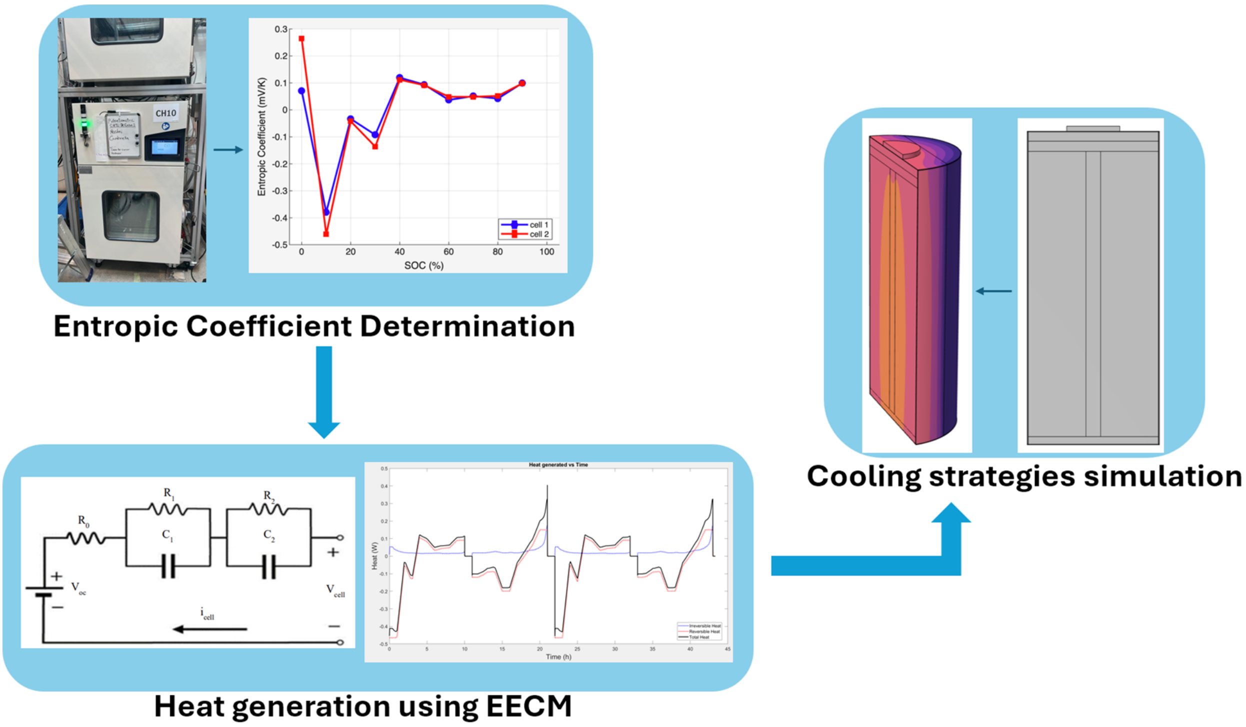

Entropic Coefficient Determination

Heat generation using EECM

Cooling strategies simulation

Thermal Characterization of Large Lithium-ion cells

MMSX30 - Master of Science Thesis

Rajesh Vishwakarma
Amithesh Selvkumar Rajeswari

DEPARTMENT OF ELECTRICAL ENGINEERING
Division Of Electric Power Engineering
CHALMERS UNIVERSITY OF TECHNOLOGY
Gothenburg, Sweden 2025
www.chalmers.se

MASTER'S THESIS 2025

Thermal Characterization of Large Lithium-ion cells

Rajesh Vishwakarma
Amithesh Selvakumar Rajeswari

Department of Electrical Engineering
Division of Electric Power Engineering
CHALMERS UNIVERSITY OF TECHNOLOGY
Gothenburg, Sweden 2025

Thermal Characterization of Large Lithium-ion cells
Rajesh Vishwakarma,
Amithesh Selvakumar Rajeswari.

Supervisor:
Daniel Poposki,
Department of Electrical Engineering, Chalmers University of Technology.

Supervisor:
Uppili Murali,
Department of Energy Storage Engineering, VOLVO Groups.

Examiner:
Dr.Torbjörn Thiringer
Department of Electrical Engineering, Chalmers University of Technology

Master's Thesis 2025
Department of Electrical Engineering
Division of Electric Power Engineering
Chalmers University of Technology
SE-412 96 Gothenburg
Telephone +46 31 772 1000

Typeset in $\LaTeX$
Printed by Chalmers Reproservice
Gothenburg, Sweden 2025

Thermal Characterization of Large Lithium-ion cells
Rajesh Vishwakarma, Amithesh Selvakumar Rajeswari
Department of Electric Power Engineering
Chalmers University of Technology

Abstract

Accurate thermal management is critical for battery management systems (BMS) to prevent thermal runaway and optimize performance. The reliability of thermal models depends on precise characterization of material properties and heat generation, yet many existing models rely on assumed or incomplete parameters, limiting accuracy. This study investigates the thermal properties and behavior of 4695 cylindrical lithium-ion cells using a combined experimental and simulation-based approach.

A custom-built isothermal calorimeter measured reversible and irreversible heat generation across various C-rates and temperatures, while entropic coefficients were determined using calorimetric and potentiometric methods to ensure consistency and validate the experimental setup. An Electrical Equivalent Circuit Model (EECM), developed with experimental and manufacturer-provided data, was integrated into a 3D electrothermal COMSOL model to analyze internal temperature distributions and heat propagation.

Results show that heat generation rises significantly with increasing C-rate, with discharging producing up to 36% higher peak heat than charging, highlighting nonlinear scaling and the importance of tailored cooling strategies. Calorimeter calibration revealed systematic errors at low power, which were effectively mitigated by offset correction and noise filtering, reducing errors to below 4% at moderate to high power levels. Cooling simulations demonstrated that double-sided liquid cooling at a 60° configuration offers the best balance between thermal performance, uniformity, and practical design, outperforming single-sided and high-angle alternatives. Overall, the integrated experimental and modeling framework provides critical insights for the design of safer, more efficient thermal management systems in large-format lithium-ion batteries for electric vehicles.

Keywords: 3-D, Li-ion, Calorimeter, Potentiometer, Thermal model, Heat transfer, EECM,

Acknowledgements

This thesis was carried out in collaboration between Volvo Groups and the Department of Electrical Engineering at Chalmers University of Technology.

We would like to thank our Chalmers examiner, Prof.Torbjörn Thiringer, for providing us with the opportunity to work with this project and taking time out of his schedule to help us in providing his expertise and guiding us in the right direction.

We want to express our sincere gratitude to Daniel Poposki, Uppili Murali and Niladri Roy Chowdhury for the invaluable guidance that they have given us throughout this thesis work. We are grateful for the time that they have spent with us to make this work easy for us.

We would like to thank our managers at VOLVO Group, Mrs.Stina Karlsson and Mrs.Ullrika Heden for their support along the course of the thesis. I would also like to thank the Cell simulation team for providing 3D thermal models based on which the models for this thesis were developed.

Special thanks to Niladri Roy Chowdhury for helping us resolve the issues faced in the built models. Finally, huge thanks to Mr.Andrew Mandeya for assisting us with the calorimeter and potentiometer tests performed at VOLVO Groups.

Finally, we are indebted to our family and friends for motivating us throughout the master's degree. Their support and encouragement have been a constant source of strength during this journey.

Rajesh Vishwakarma, Göteborg, 2025
Amithesh Selvakumar Rajeswari, Göteborg, 2025

List of Acronyms

Below is the list of acronyms that have been used throughout this thesis listed in alphabetical order:

1D	One dimensional
3D	Three dimensional
BES	Battery Energy Storage
BTMS	Battery thermal management system
CAD	Computer Aided Drawing
DER	Distributed Energy Resource
EV	Electric Vehicle
EECM	Electrical Equivalent Circuit Model
FEA	Finite Element Analysis
LIB	Lithium ion Battery
MILP	Mixed-Integer Linear Programming
MG	Microgrid
PV	Photovoltaic
RES	Renewable-based Energy Sources

Nomenclature

Below is the nomenclature of indices, sets, parameters, and variables that have been used throughout this thesis.

Indices

i,j	Indices for distribution network buses
t	Index for time step

Sets

$\mathcal{D}$	Set of distribution network buses
$\mathcal{D}_s$	Set of substation buses
$\mathcal{H}$	Set of time steps (simulation/scheduling horizon)
$\mathcal{N}$	Set of buses

Parameters

γ	Penalty coefficient
Δt	Time discretization step (time interval)
η_j^{ch}	Charging efficiency of BES
η_j^{dis}	Discharging efficiency of BES
$\boldsymbol{H}$	Adjacency matrix
N	Number of iterations
$P_{j,t}^{L}$	Active power of load demand
$P_{j,t}^{PV}$	Active power from solar generation

Variables

p_j	Active power injection at bus j
p_{ji}	Active power flow from bus j to bus i
v_i	Square of voltage magnitude at bus i
$\eta_{\text{ch}}, \eta_{\text{dis}}$	Charging and discharging efficiencies
Q_{ir}	Irreversible heat generation
Q_{rev}	Reversible heat generation
$\frac{dE_{\text{OCV}}}{dT}$	Entropic coefficient (temperature derivative of OCV)
k_{eq}	Equivalent (effective) thermal conductivity
C-rate	Charge/discharge rate relative to rated capacity
Q_{total}	Total heat generated (reversible + irreversible)
h	Convective heat transfer coefficient
P_{loss}	Power loss due to internal resistance
T_{sens}	Temperature from PT100 sensors
V_{sens}	Voltage output from heat flow sensor
SOC	State of Charge
SOH	State of Health
OCV	Open Circuit Voltage
L	Arc length of the cell
G_{th}	Thermal conductance

Contents

1

Introduction

1.1 Background

The global transition to electric vehicles (EVs) is significantly reliant on developments in lithium-ion battery technology, notably in terms of safety, longevity, and performance. Effective thermal management is crucial for this, as temperature severely limits the working region of lithium-ion cells. Inadequate thermal management can cause rapid degradation at best and catastrophic thermal runaway at worst.

While Battery Management Systems (BMS) rely on precise thermal models to regulate temperature, the quality of these models is frequently restricted by insufficient characterization of key thermal characteristics. Many existing models rely on assumed or generalized values for heat generation (which includes both irreversible (Joule heating) and reversible (entropic) heat) and material characteristics. This simplicity fails to convey the complex, non-linear thermal behavior of cells under dynamic loads, particularly in large-format cylindrical cells such as the 4695, which have significant interior temperature differences. As a result, there is a need for a completely verified, multidimensional approach that precisely characterizes heat generation and incorporates these factors into high-fidelity models, allowing for the design of optimized thermal management systems.

1.2 Purpose

The purpose of this work is to develop thermal models to study the thermal behavior of a cylindrical cell. In addition to this, a thermal model for a battery cell with active cooling strategy was developed and an experiment was performed to validate the thermal behaviour of the cell.

The principle aim of this study is:
- To determine the entropic coefficient of large-format cylindrical lithium cell experimentally on calorimeter.
- To quantify the contribution from reversible and irreversible heat over different C-rates and temperature conditions.
- To compare entropic coefficients calculated indirectly from heat measurement on a calorimeter to the direct measurement of entropic coefficient on a potentiometer at different temperatures and C-rates.

- To quantify the heat generated at different C-Rates through usage of an Equivalent circuit model (1-D) under the existing parameters and experimental part of this work.
- To develop a 3D electrothermal model for analyzing the thermal performance of the battery cell across varying C-rates.
- To make a quantitative comparison of different cooling strategies and proposing a suitable one for this cell using the 3D electrothermal model.

1.2.1 Environmental and ethical consideration

As highlighted briefly in Section 1.1, the heat generation in lithium-ion batteries is a critical factor in advancing electric-vehicles (EVs) and ultimately reducing societies dependency on fossil fuels. As our dependence on electric-powered technologies, such as EVs and renewable energy storage systems, continues to increase, lithium-ion batteries and perhaps other energy storage technologies will become a crucial element in our technological infrastructure. However, the performance of energy storage technologies is directly influenced by factors such as the rate of heat generation, which typically arises from losses and inefficiencies within the system. A deeper understanding of these thermal processes enables researchers and engineers to optimize battery design for improved heat management and overall performance. Enhanced thermal control not only increases the safety and reliability of electric vehicles and energy storage systems but also promotes the broader adoption of sustainable technologies. Consequently, this advancement supports the reduction of carbon emissions and dependence on fossil fuels, contributing to global efforts to mitigate climate change. Therefore, investigating and controlling heat generation in lithium-ion energy storage systems is essential for facilitating society's transition toward a low-carbon future.

When conducting experimental work of this nature, it is essential to consider the ethical dimensions that underpin such studies. The Institute of Electrical and Electronics Engineers (IEEE) Code of Ethics provides a valuable framework upon which this research is based. A key ethical consideration involves safeguarding the health, safety, and welfare of the public throughout the course of the study[4]. For instance, should the findings of this thesis be applied in real-world contexts, they must not pose any risk to users or the wider community. Therefore, it is imperative that all reported results are accurate, transparent, and presented with due diligence.

Given the inherent possibility of experimental error, ensuring repeatability and reproducibility is critical to validate the reliability of the findings. Moreover, any unexpected or anomalous results must be reported objectively, rather than omitted to align with a preferred conclusion or hypothesis. Finally, in an increasingly globalized and interdisciplinary research environment, collaboration across diverse cultures and perspectives remains vital. This has been embraced in the present work through engagement with individuals from different disciplines and worldviews to enhance the ethical and scientific robustness of the study.

2

Theory

The following chapter aims to provide theoretical background on the core aspects of the experimental work. At the heart of the thesis work is the lithium-ion battery cell - which is the primary test object during the experimental work. In addition, it is equally important to highlight the fundamental theory behind the experimental techniques used. Therefore, the following section will cover the working principle of LIB cells, calorimetry and the thermodynamics of heat generation.

2.1 Lithium-ion Battery

A battery is defined as a chemical storage device and in the context of electric vehicles, a battery pack consists of a set of interconnected battery cells that power the electric motor and other electronic devices in the vehicle. The scope of the thesis is primarily on the individual battery cell level. Lithium-ion batteries (LIBs) have grown in popularity due to their high power density (W/kg) and energy density (Wh / kg) compared to other battery technologies such as Lead Acid batteries. A battery with high power and energy density is an important requirement for electric vehicles as it allows for more energy to be stored while reducing the size and weight of a battery pack - and ultimately, minimizing costs.

2.1.1 Working principle of a lithium-ion cell

The fundamental unit of a battery system is the battery cell also referred to as an electrochemical cell. A battery cell converts chemical energy to electric energy and vice-versa; where the process of converting chemical energy into electric energy is referred to as discharging, while the reverse process is referred to as charging [1, 2]. Battery cells that strictly undergo the discharging process are referred to as galvanic cells, while those that only undergo charging are referred to as electrolytic cells.

The fundamental design of an electrochemical cell consists of several key components namely: electrodes, separator, electrolyte and current collectors[3]. The basic design is that lithium-ions move between positive (cathode) and negative (anode) electrodes through the electrolyte medium as illustrated in Figure2.1. The positive and negative electrodes serve as the sites for which electrochemical reactions take place. These chemical reactions that occur during charge and discharge are based on electrochemical oxidation and reduction reaction processes, or simply redox reactions. During the redox reactions, electrons travel via an external circuit from one electrode to another while aiming to maintain a balanced charge. The oxidation reaction process takes place at the negative electrode (anode), where the electrons then travel via an external circuit (through the current collector) to the positive electrode (cathode), where now the electrons are accepted and the reduction processes occurs. Simultaneously, lithium-ions flow through the electrolyte and separator towards the cathode. This process is referred to as discharging, and vice-versa would be charging. Therefore, during discharging the anode is an electron donor, while the cathode is a electron acceptor.

During the operation of a LIB cell, the State of Charge (SOC) is an important measure of the battery cell's available energy. Essentially, the SOC refers to the amount of current energy capacity (in unit of Amp hours, Ah, or milli-Amp hours, mAh) of the battery as a percentage of its maximum energy capacity (Ah). For example, if a LIB cell has a maximum capacity of 100 mAh, and it's currently at 50 mAh remaining charge, then the SOC level would be 50%. Typically, a LIB cell's upper and lower SOC limits are recommended by the manufacturer based on the tolerable voltage: 0% SOC represents the lower voltage allowed (cut-off voltage), and 100% representing the maximum voltage tolerable (voltage limit). These voltage limits are in place as to prevent under or over voltage scenarios that may lead to damages and worse-case, thermal runaway.

Accurately determining the SOC of a LIB cell is a challenging task as a LIB cell is dynamic in nature - often resulting in the true SOC level changing based on temperature, and more importantly, battery cell ageing - which is due to degradation overtime. The two main methods of estimating a LIB cell's SOC level is by coloumb counting, which is the integration of the amount of current (ampere) with time (hours). The other method is by open circuit voltage (OCV) relaxation, where the battery cell's SOC level is estimated by the open circuit voltage obtained after allowing a long relaxation period.

2.1.2 Cell Form Factor

LIB cells used in electric vehicles typically come in three designs: cylindrical, prismatic and pouch cells. Each of which have their own advantages and disadvantages.

Cylindrical

Cylindrical cells are the most recognizable shape of battery cells, and they are made from electrodes materials that are wound together in a "jelly-roll" shape as seen in Figure 2.2(a). These cells are often encapsulated in a hard casing as to provide mechanical strength. Their main advantage is they are typically faster and cheaper to manufacture compared to the other designs. However, a major challenge is they do not occupy space efficiently compared to a prismatic or pouch cell due to the nature of cylindrical geometry – hence they are not ideal when it comes to packaging.

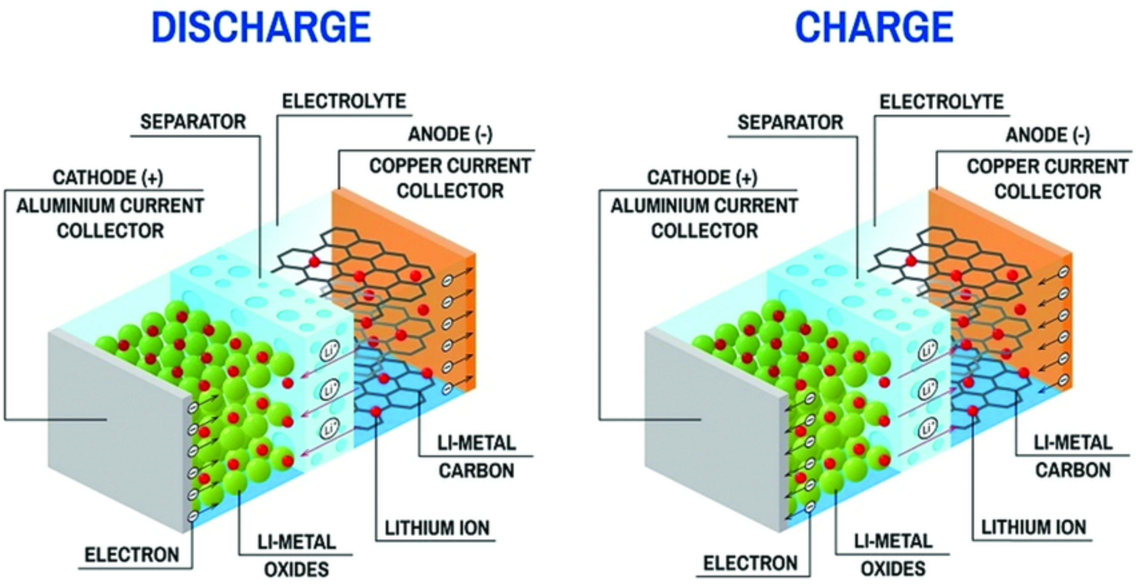

Figure 2.1: Charge–discharge process in Li-ion battery (Image Credit: https://sivVector/Shutterstock.com)

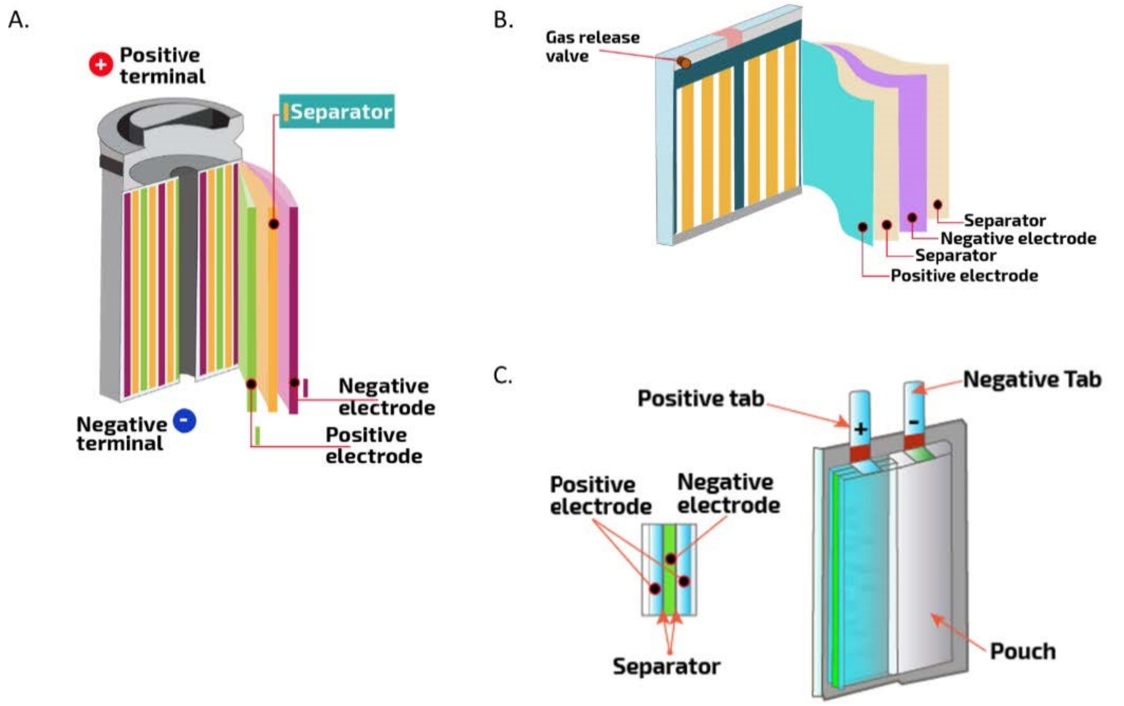

Figure 2.2: Type of packing for Lithium ion battery a) Cylindrical cell, b) Prismatic cell and c) Pouch cell (img credit:Barnett Technical Services. (n.d.). Hot Disk – Battery Anisotropy. Steve's Solutions.)

Prismatic

Prismatic cells are rectangular shaped LIB cells that are typically enclosed in a metal casing as seen in Figure 2.2(b). The electrodes can either be wounded or stacked on top of each other. Like the cylindrical cell, the prismatic is encased with metal (typically aluminum metal casing) to improve the mechanical strength. The size of these cells tend to be larger than cylindrical and hence the overall capacity is usually higher. However, if packaging is not done carefully in a battery pack, then thermal management can be a challenge – where thermal propagation (spread of heat from cell to cell) becomes more likely.

Pouch

Finally, the pouch cell shares resemblance to the prismatic with the rectangular shape, however they are not enclosed in a metal casing, but instead in a pouch as seen in Figure 2.2(c). These pouches are normally made of a layer of aluminum-coated plastic film and thus allowing them to be light. Hence, pouch cells tend to be thinner allowing them to be packaged in a more efficient manner compared to prismatic and cylindrical. However, this comes at the cost of poor mechanical strength as there is no metal casing to protect the LIB cell. The electrodes are typically stacked or rolled in a Z-fold.

2.2 Thermodynamics and Heat Generation in LIB Cells

In understanding the heat generation and transfer processes that occur within lithium-ion (LIB) cells, it is important to explore the underlying thermodynamic principles. Thermodynamics describes the relationships between heat, energy, and work. In LIB cells, these relationships are key to understanding the mechanisms of heat generation and energy losses.

2.2.1 Heat Generation Components

Heat generation (Q_{bat}) in a LIB cell comprises both irreversible heat (Q_{irr}) and reversible heat (Q_{rev}) components

$$Q_{\text{bat}} = Q_{\text{irr}} + Q_{\text{rev}} \tag{2.1}$$

Irreversible heat: Associated with ohmic losses, calculated by product of current (I) and difference between the battery's actual measured voltage during operation (E) and it's open-circuit voltage (E_{OCV})

$$Q_{\text{irr}} = I(E - E_{\text{OCV}}) \tag{2.2}$$

Reversible heat: Due to entropic changes during charge/discharge given by the the product of current, temperature of the cell (T_{cell}) and entropic coefficient of the the cell ($\frac{E_{\text{OCV}}}{\partial T_{\text{cell}}}$)

$$Q_{\text{rev}} = IT_{\text{cell}} \left(\frac{\partial E_{\text{OCV}}}{\partial T_{\text{cell}}} \right) \tag{2.3}$$

Combined equation: The total heat generation becomes

$$Q_{\text{bat}} = I(E - E_{\text{OCV}}) + IT_{\text{cell}} \left(\frac{\partial E_{\text{OCV}}}{\partial T_{\text{cell}}} \right) \tag{2.4}$$

This equation shows that heat is generated due to internal resistance (ohmic heating) and entropy changes. The sign of $\frac{\partial E_{\text{ocv}}}{\partial T}$ determines whether the entropy change is endothermic (cooling during discharge) or exothermic (heating during charge).

2.3 Heat generation thermal parameter

2.3.1 Open Circuit Voltage (E_{OCV})

Common approaches to measuring the E_{OCV} of lithium-ion cells include linear interpolation during low-rate cycling, Galvanostatic Intermittent Titration Technique (GITT), and voltage relaxation methods. The linear interpolation method involves cycling the cell at very low current rates (typically $I < C/10$) such that overpotentials are minimized, allowing the instantaneous voltage to approximate the true equilibrium voltage. Voltage relaxation methods commonly apply partial discharge steps (e.g., every 5% SOC), followed by extended rest periods (often multiple hours), assuming the cell voltage stabilizes toward the E_{OCV} once chemical and electrical equilibrium is reached (typically when voltage variation is less than 0.1 mV/min).

In the present study, however, the E_{OCV} was determined using a calorimetric method at a low C-rate of C/20 and a controlled temperature of 25°C, where the cell was cycled through the full depth of discharge (0–100% SOC) during both charge and discharge. This approach eliminates the need for prolonged rest periods at each SOC step, which are typical in potentiometric or GITT methods, allowing for a continuous evaluation of the cell's thermal and electrochemical response.

2.3.2 Entropic Factor Determination

The entropic factor, often referred to as the entropic coefficient ($\partial E_{\text{OCV}}/\partial T_{\text{cell}}$), can be obtained either by direct voltage measurements across temperatures or indirectly by thermal loss analysis. The two main direct measurement methods include the potentiometric technique and the less commonly used calorimetric approach [4, 5].

The potentiometric method measures the cell's E_{OCV} at discrete temperatures, assuming a linear relationship between voltage and temperature at a certain SOC, whereby the slope of this linear fit yields the entropic coefficient. While accurate, this technique requires prolonged equilibration times, especially for larger cells, due to the slow approach to true equilibrium [6].

The calorimetric method employed in this work, carried out at a low current rate ($I \leq C/10$), leverages the measurement of the total heat generated by the cell inside a calorimeter at constant, controlled temperature. Since the calorimeter captures both reversible and irreversible heat, the irreversible heat contributions arising from overpotentials and joule heating can be effectively subtracted by averaging the heat generated during charge and discharge cycles at the same C-rate [7].

The advantage of this calorimetric approach is the ability to cycle the cell continuously over the entire 0–100% SOC range without requiring lengthy rest periods at each SOC interval, while still obtaining a continuous and smooth profile of the entropic coefficient.

A key assumption underlying this method is that the irreversible heat—primarily due to ohmic resistance—is approximately equal during charge and discharge at a fixed C-rate. Therefore, the entropic factor can be estimated using a simplified relation derived from the Newman equation

$$\left(\frac{\partial E_{\mathrm{OCV}}}{\partial T_{\mathrm{cell}}}\right) = \frac{Q_{\mathrm{discharge}} + Q_{\mathrm{charge}}}{2IT_{\mathrm{cell}}}, \tag{2.5}$$

where I is the applied current, T_{cell} is the cell temperature (in Kelvin), and Q_{charge} and $Q_{\mathrm{discharge}}$ represent the measured heat losses during charge and discharge cycles, respectively [7].

This methodology, as applied in the current study, reliably produces entropic coefficient data that are consistent with previous findings, while offering a practical balance between measurement accuracy and experimental duration [4].

2.4 Calorimetry

A calorimeter is an instrument used to measure the heat of chemical reaction or physical changes. The basic principle is that a calorimeter contains a vessel (or container) in which the sample being studied is placed. The surrounding area of the calorimeter is known as a shield, and there can be several shield layers to provide improved isolation of the sample.

Calorimeter instruments can be divided into the following main categories:

1. Adiabatic calorimetry in which there is no heat exchanged with the outside environment. In order to achieve this it is a prerequisite to have near perfect insulation so as to ensure that there no heat being added or removed from the system.

2. Non-adiabatic calorimetry are those that have exchange of between the vessel and the outside environment.

3. Isothermal calorimetry in which there is a constant shield temperature.

4. Non-isothermal calorimetry in which the shield temperature is not constant.

The calorimeter experimental setup used in the following thesis work is a isothermal conductive calorimetry.

2.4.1 Heat flow sensors

The heat flow sensors that are integrated inside of the calorimeter are thermo-electric devices that are based on the Seebeck effect (the reverse being the Peltier effect) which is a phenomenon where a temperature difference will produce a voltage signal. The heat flow sensors consist of a large number of thermocouples connected in series electrically to produce a large voltage output, while also being connected in parallel thermally to produce a high voltage to temperature difference ratio. Typically, the thermocouples are made of p- and n-doped bismuth telluride. The voltage difference ΔU is generated across the semiconductor material inside the heat flow sensors when a temperature difference ΔT is applied across the junctions of the material. The amount of voltage produced per temperature difference is referred to as the Seebeck coefficient - thus it defines the strength of the thermoelectric effect of the heat flow sensors. The Seebeck coefficient a (V/K) for a single thermocouple is defined by

$$\Delta U = a\Delta T \tag{2.6}$$

Within a heat flow sensor the Seebeck coefficient can be defined as $E = Na$, where N is the number of thermocouples in the thermoelectric device. According to author Wadsö the sensitivity of a thermoelectric heat flow sensor is governed by the following properties [8]:

- The devices thermal conductance, $K(W/K)$
- The Seebeck coefficient, $E(V/K)$

These two coefficients relate both the heat flow rate through the heat flow sensors, as well as the voltage output for K and E respectively, to the difference between the sample and the heat sink in the calorimeter. Ultimately, the ratio between these two properties will provide the ratio between heat flow rate per voltage output—which represents the calibration coefficient

$$\epsilon = K/E \tag{2.7}$$

2.4.2 Calorimeter calibration

The heat flow sensors record the heat dissipated from the Li-Ion in terms of the voltage response. However, to measure the heat dissipated in units of watts, a calibration coefficient is required. The calibration coefficient ϵ is a constant that indicates the proportion between the calorimeter output (in voltage) and the thermal power input. A common method of determining the calibration heat conduction calorimeters is by electrical calibration [8]. This involves using a calibration heater (resistor) which is heated by passing a current $I(A)$, and the corresponding voltage response is measured. The thermal power $P(W)$ that is produced in the calibration heater with resistance $R(\Omega)$ can be obtained from

$$P = I^2 R \tag{2.8}$$

An important aspect of conducting calorimetry experiments is in using a reference sample. The central idea being the reference (or second 'sample') should not produce any heat, but should have similar thermal properties as the sample. By using the reference, one can record the heat flow measurements of both the sample and the reference, where the difference between the two can be measured. If the calorimeter setup up reaches thermal equilibrium, then low noise and low drift will be measured. Author Wadsö [8] notes that the important property of the reference is that the thermal properties (e.g. heat capacity) should be similar, and that not the reference should not produce any heat. Considering calibration at different thermal powers, the general principle is that one should expect the voltage output from the heat flow sensors to follow a proportional relationship to the thermal power at steady state. Therefore, the calibration coefficient should be independent to the thermal power level.

2.4.3 State-of-Charge (SOC) Determination

Lithium-ion (Li-ion) batteries are widely used in electric vehicles, renewable energy systems, and grid storage. Accurate estimation of the state of charge (SOC)—defined as the available capacity (in Ah) expressed as a percentage of the rated capacity—is essential for ensuring performance, safety, and battery longevity [9, 10].

SOC estimation is challenging due to the complex electrochemical processes involved, as well as varying operating conditions such as temperature, ageing, and current flow. Overcharging or deep discharging can cause irreversible battery damage, making reliable SOC monitoring a key function of any battery management system (BMS) [11, 12].

A common method for estimating SOC is coulomb counting, which integrates the current over time. This is often supported by voltage measurements and cell-specific data, including temperature and aging characteristics. Manufacturer-provided characterization data can further improve estimation of the accuracy [9].

Despite its usefulness, Coulomb counting is sensitive to initial SOC errors, self-discharge, and leakage currents. Therefore, modern systems often combine it with model-based or data-driven approaches to ensure robust SOC tracking throughout the battery life cycle [10].

2.4.4 Coulomb Counting Method

The coulomb counting method, also known as ampere hour counting and current integration, is the most common technique for calculating the SOC. This method employs mathematically integrated battery current readings over the usage period to calculate SOC values given by

$$SOC = SOC(t_0) + \frac{1}{C_{\text{rated}}} \int_{t_0}^{t_0+\tau} (I_b - I_{\text{loss}})dt \tag{2.9}$$

where SOC(t_0) is the initial SOC, Crated is the rated capacity,I_{b} is the battery current, and I_{loss} is the current consumed by the loss reactions [10, 12].

The Coulomb counting method then calculates the remaining capacity simply by accumulating the charge transferred in or out of the battery. The accuracy of this method relies primarily on a precise measurement of the battery current and an accurate estimation of the initial SOC. With a pre-known capacity, which might be memorized or initially estimated by the operating conditions, the SOC of a battery can be calculated by integrating the charging and discharging currents over the operating periods. However, the releasable charge is always less than the stored charge in the charging and discharging cycle. In other words, there are losses during charging and discharging. These losses, in addition with the self discharging, cause accumulating errors. For a more precise SOC estimate, these factors should be taken into account. In addition, the SOC should be recalibrated on a regular basis and the declination of the releasable capacity should be considered for more precise estimation [11].

2.5 Battery Models

The main objective of the battery model is to estimate heat generation while also predicting cell performance. There are various battery models, each with its own set of objectives and complexity. Furthermore, when selecting a battery model, certain variables must be considered. Complexity, computation time, accuracy, and number of parameters are just a few examples.

2.5.1 Overview of Battery Models

A comprehensive study was conducted on different battery models to evaluate their goals, application, and complexity. Each model is designed to capture different aspects of battery behavior. In this section, we will explore more about various battery models and choose the best model for our work.

2.5.1.1 Electrical Equivalent Circuit Model (EECM)

It is the most common approach for battery numerical analysis. Electrical equivalent circuit modeling is a useful description of battery dynamics that can capture the battery cell's non-linear attributes. In addition, the model is capable of precisely describing the I-V properties of the battery and presenting its electrical behavior. EECM can be used to optimize battery designs, enhance performance, and prolong battery life by simulating the battery's behavior under diverse operating conditions. Finally, it is easy to combine with other methods (e.g. Coupled with Thermal Model to form an Electro-Thermal Model) and is computationally essential.

2.5.1.2 Electrochemical Model

Beginning with the battery's internal operation, the electrochemical model provides a plausible explanation of how lithium ions behave in the battery during charging and discharging. Every model parameter has a distinct physical meaning. The electrochemical mechanism model is appropriate for use in the aging and degradation analysis of battery performance since it can simulate the significant microscopic physical quantities inside the battery in addition to describing the macroscopic physical quantities like voltage and current [13]. But the model often set up partial differential equations with many unknown parameters[14].

2.5.1.3 Peukert's Law Model

The Peukert's law is used to predict the runtime of fully charged rechargeable lead-acid batteries and assess their nonlinear capacity under different constant discharge currents. It is used to represent the rate dependence of the lead Acid Battery capacity, because of its accuracy, ease of use, and robustness over a wide temperature range. It also applies to a wide range of lead acid battery technologies with varying voltages and capacities. But it has it's own limitations. For example, it doesn't consider the effects of temperature on batteries, age of the battery and self discharge rate of the battery during low discharge rate [15].

2.5.1.4 Neural network model

An efficient method for estimating SOH is the neural network model. The input layer, the hidden layer, and the output layer make up its three layers. SOC is one of the model inputs, along with the ECM parameters ohmic resistance (R0), polarization resistance (Rp), and polarization capacity (Cp). A neural network is a type of statistical model that requires a lot of experimental data to train in order to produce optimal results. It is taught repeatedly by a learning algorithm until the estimation error is smaller than the predetermined threshold and does not require knowledge of the precise electrochemical reaction [16].

2.5.1.5 Selection of Battery Model

The integration of models with the BTMS is a crucial element in choosing the appropriate model, alongside factors such as accuracy, the number of parameters needed for the model, computation time, and complexity.

- Neural network models are efficient; however, they necessitate a substantial amount of experimental data, which can be challenging to obtain.

- The Peukert's law model is primarily utilized for lead-acid batteries, and the Peukert's law equation fails to account for the effects of temperature and cycle life on battery capacity.

- Both the electrochemical model and the equivalent circuit model offer viable alternatives and can be integrated with the BTMS.

- The electrochemical model is the most precise for estimating the state of charge (SOC); however, it is quite complex and involves partial differential equations, making real-time solutions challenging.

- Conversely, the electrical equivalent circuit model requires fewer parameters, provides accurate results, is applicable to all battery chemistries, performs well under nonlinear conditions, and has low complexity.

Thus, the electrical equivalent circuit model is selected for the battery model in this study.

2.6 Electrical Equivalent Circuit Model

Equivalent circuit model offers a practical solution by representing the battery as an electrical network with passive components. These components includes resistors, capacitors, and ideal voltage sources are used to capture the key features of the battery's behavior. Equivalent circuit modeling is used to optimize battery designs, increase performance, and extend battery life by precisely imitating the battery's behavior under various kinds of operating conditions. Thevenin model of the ECM as depicted in figure 2.3, is used in this study due to its balance between accuracy and simplicity. The components of the EECM are described in Table 2.1.

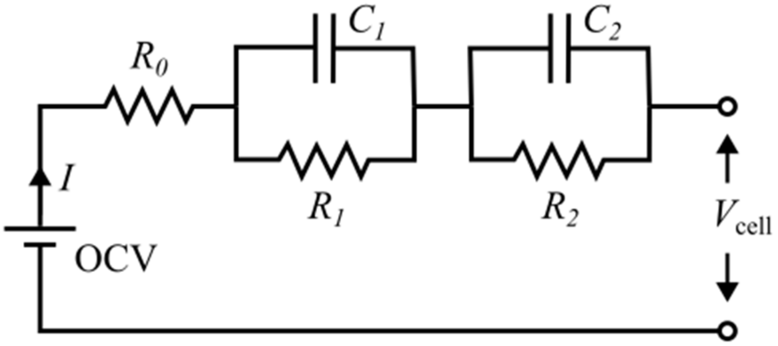

Figure 2.3: ECM thevenin model with 2 RC pairs.[17]

$$V_t = V_{OC} - IR_0 - V_{RC1} - V_{RC2} \tag{2.10}$$

where:

- V_t is the terminal voltage of the battery (V),
- V_{OC} is the open-circuit voltage, which depends on the state of charge (SOC) (V),
- I is the battery current, positive during discharge (A),
- R_0 is the ohmic resistance representing internal and contact losses (Ω),
- V_{RC1} and V_{RC2} are the voltage drops across the first and second RC networks (V).

Table 2.1: Battery Equivalent Circuit Component Descriptions

Parameter	**Component Type**	**Description**
R0	Resistor	Ohmic resistance
R1	Resistor	Charge transfer resistance
R2	Resistor	Diffusion or polarization resistance
C1	Capacitor	Double-layer capacitance
C2	Capacitor	Diffusion capacitance (Warburg equivalent)
I	Current	Current flow through the components
OCV	Voltage Source	Open Circuit Voltage
Vcell	Terminal Voltage	Voltage of the cell

Using (2.10), the instantaneous terminal voltage of the battery under load is calculated. It accounts for the open-circuit voltage, the instantaneous drop due to internal resistance, and the transient voltage drops across the two RC networks, capturing both fast and slow polarization effects.

According to [18], the double RC network is the most popular ECM design, and provides a good trade-off between error and complexity when compared to single and triple RC network designs. Although the accuracy of three pairs of RC networks is higher, they are more complicated and require a significant amount of computing time. On the other hand, accuracy and computation are low in a single pair RC network. The solid/electrolyte interface (SEI) dynamics, lithium ion diffusion, and charge transfer kinetics are examples of transient battery dynamics that are captured by the double pair RC network.

When modeling a battery's dynamic behavior, accuracy and complexity are both essential considerations. The ECM has the ability to meet both criteria well. The model is made up of three major components: one representing the thermodynamic properties of the battery chemistry, such as the open-circuit voltage (OCV) as a function of SOC, another representing the kinetic aspects of the cell's internal impedance behavior and a source or load to complete the circuit for charge or discharge procedures [19].

2.7 Battery Thermal Models

There are multiple thermal models for battery cells that have been identified in the literature. Different models have varying effects on how well heat is transferred within the cell. Choosing the appropriate thermal model based on the data available is required to analyze the temperature profile of the battery cell during operation.

2.7.1 Partial Differential Equation Models

At first, physics-based battery models that describe electrochemical, thermal, and ageing behaviors are developed. The combination of all of these models results in an extremely complicated structure that is formally represented by a sequence of coupled nonlinear partial differential equations (PDE). The modeling of such a system is severely limited due to its excessive demand for computing power and complexity.

2.7.2 Lumped RC Thermal Model

The battery is separated into a limited number of distinct nodes, each of which is regarded as a separate part in the design of this model. Additionally, it is assumed that the system's temperature gradient is minimal, which suggests that conduction-induced internal thermal resistance is minimal. Finally, it is also assumed that the battery's properties are uniform. The battery casing and core, for instance, are regarded as two distinct isothermal nodes. On the other hand, the anode, cathode, separator, and other components inside the core are seen as a single, homogeneous entity with averaged properties [20].

2.7.3 FEA of Battery Thermal Model

The finite element method is a method that involves discretizing the object to be examined or dividing it into multiple components. A node connects each element to its neighbors. Then, a mathematical equation is created to represent the object being viewed. According to [14], this model is accurate and useful for investigating the behavior of heat in the cell and surroundings. However, it requires a large amount of data, which can lengthen the duration of the simulation.

2.7.4 Selection of Thermal Model

The choice of the battery thermal model is influenced by several factors, including accuracy, the simulation tools at hand, the data available, and how well it integrates with the Battery Thermal Management System (BTMS). The Partial Differential Equation (PDE) model is overly complex and requires intricate mathematical equations. In this study, we have opted for the lumped capacitance thermal model. The lumped capacitance thermal model is straightforward, providing satisfactory accuracy along with quick computation times.

2.8 Temperature effects on Cell

Lithium-ion batteries for electric vehicles must be able to operate at a variety of temperatures, typically between 20 and 40°C. Temperature has a significant impact on both cycle life and energy capacity. High temperatures limit battery life, while low temperatures affect the cell's energy, power, and charge capacity. The thermal problems and effects of commercial Lithium-ion batteries are covered in detail in this section.

2.8.1 Effects at high temperatures

When the battery is subjected to high temperatures, there is a loss in power and also a fade in capacity that causes performance degradation of the Lithium-ion cell.

According to [21] when the ambient temperature exceeds 25°C and lower than 55°C, the discharge capacity of the battery increases as the temperature rises. This is due to increased activity of the battery's internal materials, faster deintercalation of lithium ions, and a decrease in internal resistance. When the ambient temperature rises to 60°C, the discharge capacity of the lithium ion battery of the three materials falls slightly below that of 55°C. The fundamental cause is that high temperatures reduce the activity of the active battery's internal electrolyte and the reaction strength of the electrode material.

Apart from performance degradation, when LIBs are subjected to high temperatures, aging occurs. Aging shortens LIBs' lifespan in addition to affecting their performance. Cycle aging and calendar aging are generally included in the aging of LIBs. However, because of the complex composition and mechanism of LIBs, these two forms of aging always coexist. The aging process will be accelerated and LIB degradation will result if the operation temperature is raised above the ideal range [22].

2.8.2 Effects at low temperatures

First, the low temperature will change the electrolyte's properties. As the temperature decreases, the viscosity of the electrolyte increases, reducing ionic conductivity. As the impedance of the directional migration of chemical ions increases, so does the internal resistance.

In addition to that, the rise in charge-transfer resistance in LIBs is also a significant factor in performance degradation at low temperatures. LiFePO4-based cathodes exhibit three times higher charge-transfer resistance at -20°C compared to room temperature [23]. According to [24], the charge-transfer resistance grew drastically as the temperature dropped. A depleted battery has much higher charge-transfer resistance than a charged battery. Charging a battery at low temperatures is consequently more challenging than discharging it. Additionally, performance decrease at low temperatures is linked to the slow pace diffusion of lithium ions within electrodes.

2.8.3 Thermal Runaway

The vast majority of LIB fires can be traced back to LIB thermal runaway (TR), which is caused by mechanical, electrical, and/or thermal abuse and involves complex chemical and physical processes. Thermal runaway is more likely to occur when the battery temperature exceeds 80°C. Between 80 and 100°C, the anode begins to degrade, and an exothermic reaction within the cell produces a variety of gasses. As the temperature rises, the separator and electrodes melt, resulting in contact between the anode and cathode. A positive cathode begins to degrade and release oxygen about 130°-150°C. The cell may ignite and catch fire as a result of oxygen evolution and other chemical reactions. At temperatures between 150°C and 180°C, the cell becomes thermally unstable and may experience thermal runaway if heat dissipation is inadequate [25].

Individual lithium-ion cells may fail thermally for a variety of causes, the most common of which being internal short-circuits, overheating, and overcharging or discharge. These factors also produce an initial increase in cell temperature, which triggers this chemical processes.

- **Internal Short Circuits**: These are a typical cause of thermal runaway, often due to physical damage, defects in manufacturing, or the failure of internal separators, resulting in direct contact between the anode and cathode.

- **Overcharging and Discharging**: Excessive charging or discharging rates might stress the battery, increasing the risk of overheating and thermal runaway.

- **External Heat Sources**: Thermal runaway can occur when batteries are exposed to high ambient temperatures or are close to heat-generating equipment because they can more rapidly reach critical temperatures.

2.9 Thermal Management System

The Battery Thermal Management System (BTMS) is a vital component of electric vehicles (EVs) and other energy storage systems that use rechargeable batteries. The primary purpose of this device is to keep batteries within an appropriate temperature range, ensuring their safety, efficiency, and lifespan. Temperature changes have a considerable impact on battery performance, so it is critical to keep them within a particular range. The primary function of a BTMS is to control the temperature of the battery pack using cooling and heating technologies, which may involve the use of cooling systems, fans, or other devices to manage heat generated while charging or discharging and give warmth under particular situations.

BTMS can be applied with a variety of methods, including air cooling, liquid cooling, phase change materials (PCMs), and thermoelectric coolers as depicted in figure 2.4. The two primary types of BTMS are active BTMS, which uses fluids in motion, and passive BTMS, which does not. Electric vehicles typically use active systems, such as pushed air or coolant. Liquid cooling systems can be direct or indirect, with direct systems providing better heat transfer but necessitating additional study into dielectric fluids.

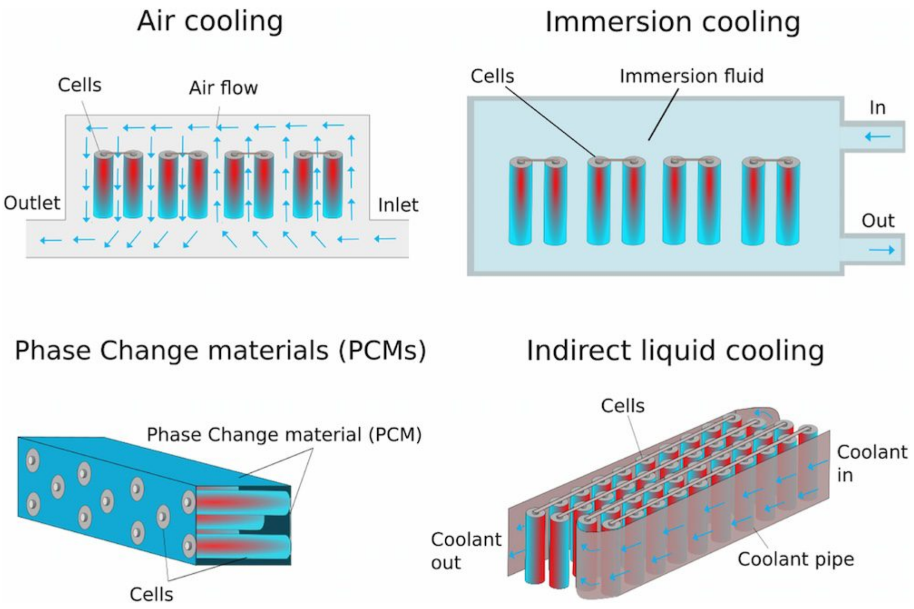

Figure 2.4: Different types of thermal management systems for EV batteries [26].

2.9.1 Air Cooling

The use of air to cool LIBs has becoming more common in commercial vehicles because of its intrinsic benefits, which include less complex design, economic feasibility, and smaller packing. In electric vehicle powertrains, air cooling of the battery is lightweight, low maintenance, and has a straightforward design. In this kind of management system, the air is used for ventilation, heating, and cooling. The heating or ventilation effects can be achieved by either forced or natural convection.

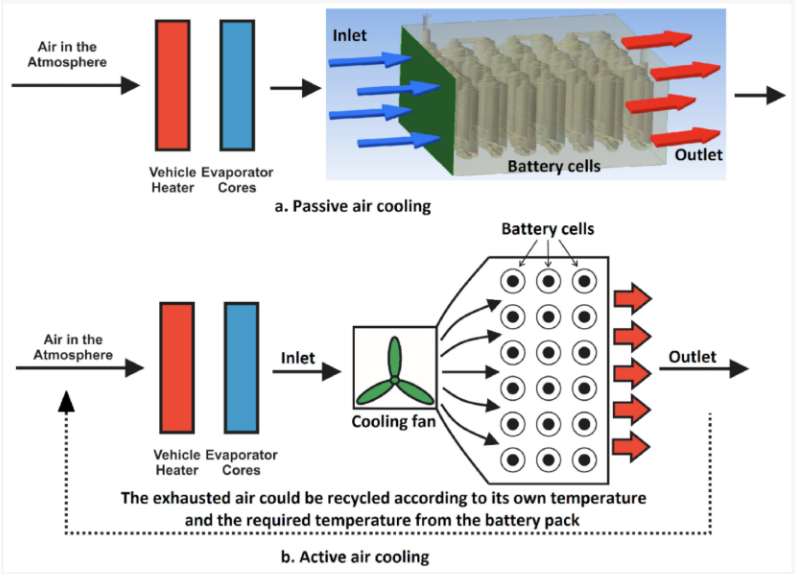

Figure 2.5: Schematic diagram of air cooling, (a) passive air cooling, and (b) active air cooling [27]

When active cooling is used, an electric fan blows air over the battery pack at higher speeds as shown in figure 2.5. The accelerated air thus reduces the maximum temperature and temperature fluctuations. When using natural air cooling, air convection flows into the battery pack without spending any energy, making it only ideal for low-density batteries. The advantage of passive air cooling is that it costs less than active air cooling and is run silently due to the absence of fans.

According to [28], there are three significant variables in the air-cooling system. These variables, which can improve or decrease the system's efficiency, are airflow velocities, flow rate, and the geometrical arrangement of the battery packs.

As reported by [14], the air-cooling system has been frequently employed in BESS. Air cooling may not be the optimal cooling technique due to its poor heat capacity and thermal conductivity. However, it remains an appealing solution for BTMS because there are no leaks and no heat exchangers. It is also easier and more comfortable to maintain than liquid cooling. The only cooling system in Table that uses passive air convection is the Nissan Leaf EV. The movement of the car while driving improves airflow through the battery pack, making the passive cooling system more efficient.

2.9.2 Liquid Cooling

Liquid cooled BTMS are used in EVs to have enhanced heat dissipation characteristics when compared to Air cooled BTMS. These BTMS use liquid coolants such as water, ethylene glycol or nanofluids to remove heat efficiently from the battery cells and also maintaining an optimal operating temperature which helps in improving battery pack longevity and safety. Liquid cooling can be categorized into two methods: one in which the coolant comes into direct contact with the battery cells, and another in which the coolant runs through channels or plates that contact the battery module. Indirect cooling technique moves the heat produced by the battery to the outside with the flowing coolant, avoiding direct contact between the coolant and the battery whereas Direct cooling greatly improves the contact area between the battery and the coolant, thereby obtaining an extremely high heat transfer rate. Direct liquid cooling can be classified as single or two phase depending on whether the coolant has a phase change. Direct liquid cooling outperforms indirect liquid cooling in terms of cooling effect and temperature distribution uniformity. Because the battery and coolant are in direct touch, elaborate flow channel designs are unnecessary, and the potential of unintentional coolant leakage, which could create short circuits in the battery, is minimized [29].

Jiahao Liu et al.[29] have also discussed that different battery shapes are appropriate for different cooling devices when using indirect liquid cooling. Cylindrical batteries typically use isolated tubes or jackets to increase the surface-coolant contact area. Flat cold plates are usually the best option for prismatic and pouch batteries as shown in figure 2.6. Because the coolant and battery do not come into direct contact, the air gap between the cooling plate or tube and the battery contributes to heat insulation and lower heat transfer efficiency. To remove air gaps and thus reduce thermal contact resistance, a high-precision cold metal plate and a high-thermal conductivity grease or epoxy bonding agent are required.

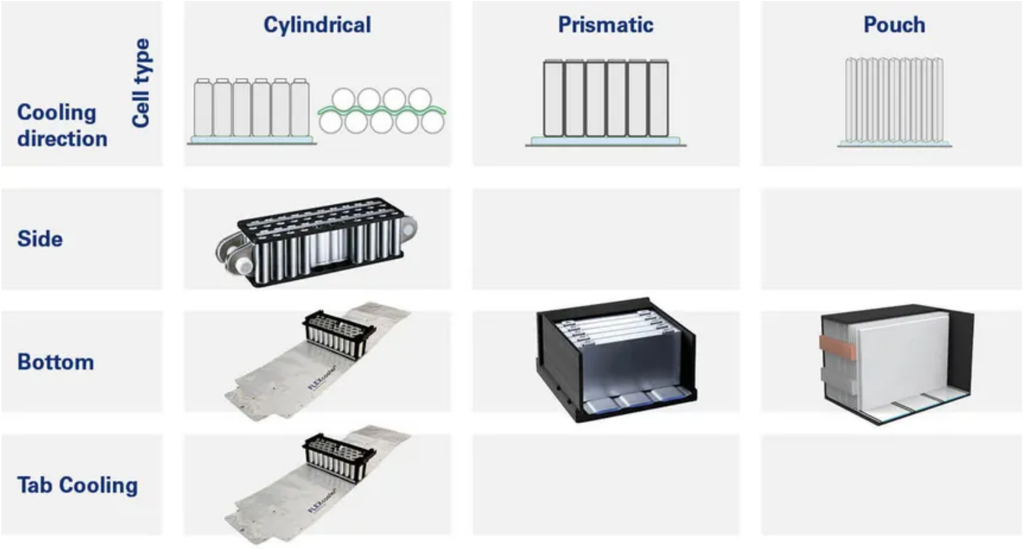

Figure 2.6: Cooling direction for different cell types [30].

The liquid cooling system has four primary factors. Similar to air cooling, these factors—the number of channels, the inflow mass flow rate, the flow direction, and the channel width—can increase or reduce the system's efficiency. These factors were studied and the results were provided by [31].

- The cooling efficiency improves as the number of channels increases. However, cold-plates with more than five channels do not appear to have any significant advantages.

- To minimize the maximum temperature and temperature differential, increase the inflow mass flow rate, which is more efficient than other approaches. However, it comes at the expense of energy usage.

- Increasing the channel width can reduce the energy consumption. When it was doubled in size, there was a significant drop in pressure. Lowering the temperature difference between batteries is challenging due to higher heat generation in the near-electrode area and varying cooling effects.

Because of the cost and safety considerations, such as the possibility of short-circuiting and leaking, the direct liquid cooling system for BTMS may not be the preferred choice for most present applications. Direct liquid cooling requires a dielectric material with low viscosity, high thermal conductivity, and thermal capacity, unlike indirect cooling systems.

3

Case Setup

The following section aims to describe the methodologies followed during the calorimeter, cell assembly, cell characterisation and heat generation experiments. The main requirement of the experimental methodology is to address the objectives outlined in Section 1.2.1.

3.1 Overall setup for calorimeter

The overall experimental setup is shown in figure 3.1. The setup consists of a custom-build calorimeter that is housed in a styrofoam box. The working principle of the calorimeter was described in Section 2.4. The calorimeter consists of two sides labeled side A and side B, where in between the sample and reference cells are placed. Between the sample and reference, the styrofoam material is placed to insulate the sample and reference from potential heat transfer.

The two sides of the calorimeter aluminum plates are integrated with thermal heat sensors. On each side, there are two pairs of thermal sensors connected in series, giving a total of 8 - four on each side. The heat sinks on both side A and B have the water circulation flowing through and is controlled by the Julabo temperature regulator. To provide good contact, both plates are tightened using spring holders. The voltage output from the heat flow sensors on sides A and B for both sample and reference are added together - thus giving the total heat output from the sample. The voltage output in the thermal sensors are recorded using the PICO logger. PT100 temperature sensors are used to measure the temperature on each side A and B of the calorimeter, the calorimeter indoor box temperature and the outside temperature. In total, 8 channels connected to PICO logger were used for recording the PT100 temperature. The calorimeter was placed inside a large styrofoam box as to replicate a adiabatic environment where minimal heat is to escape to the outside environment. Finally, the isothermal bath system used was a Julabo F25MA which provided a constant supply of water at constant temperature.

3.2 Measuring instrument

The various measurement instruments used throughout the experimental work include the following:

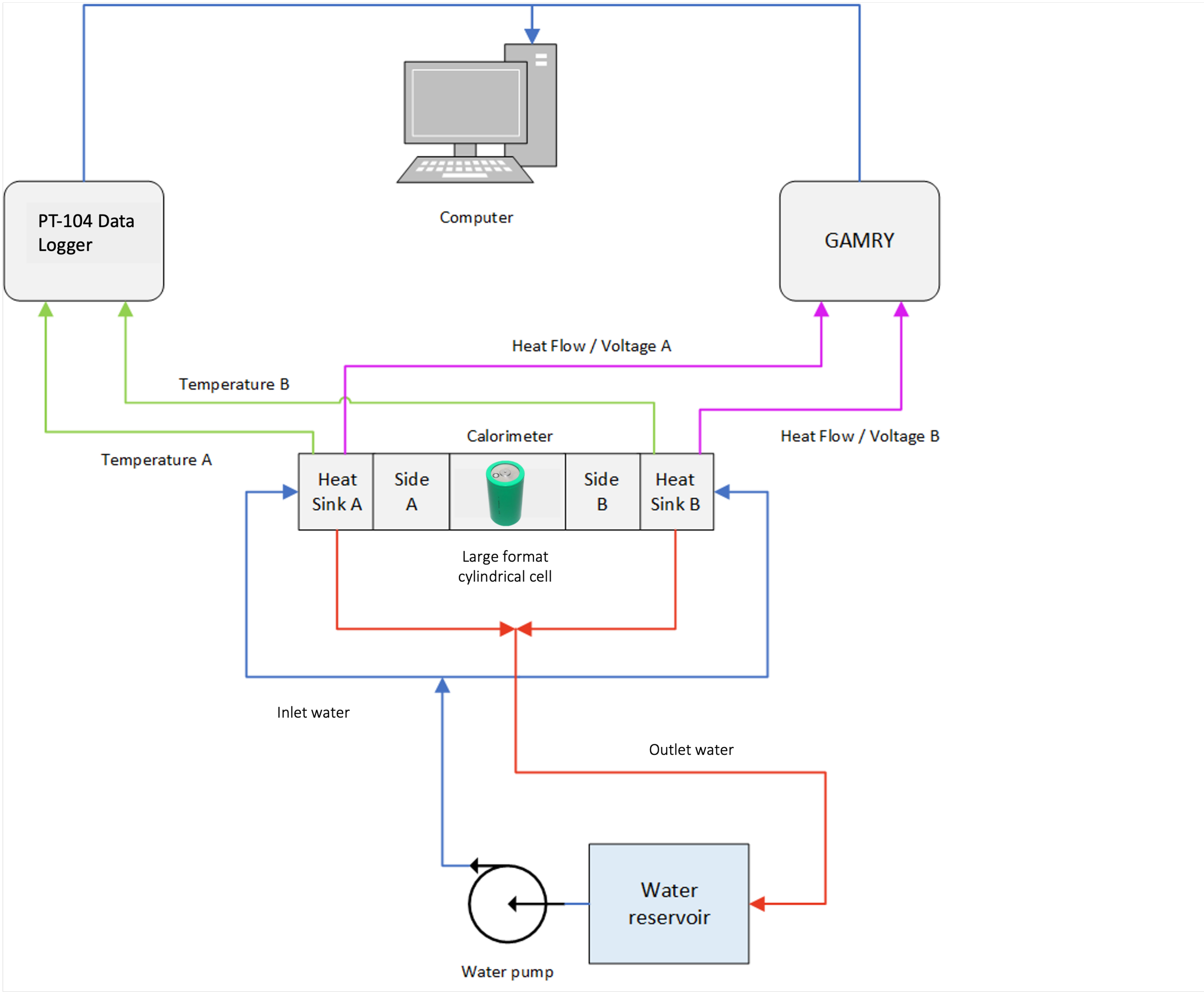

Figure 3.1: Overview of experimental setup on calorimeter.(Adapted from authors Lidbeck & Syed [13])

- **GAMRY Reference 3000 potential**: The battery tester is used to perform electrochemical tests on LIB cells such as charging and discharging cycles. The heat flow measurements (in mV), cell voltage output (V), and current (A) are measured using the GAMRY.

- **PT-104 Data Logger**: Temperature and heat flow measurement recorder in degrees Celsius and milliVolt respectively.

- **FLUKE 787**: Multimeter used to measure voltage and resistance of sample in Volts and ohms respectively.

- **MACCOR 4000**: Potentiometric measurements were performed using the MACCOR 4000 cell tester system, which offers high-precision control over voltage, current, and temperature parameters. The MACCOR 4000 enables reliable cycling protocols and open-circuit voltage measurements necessary for the accurate determination of entropic coefficients in lithium-ion cells. The system integrates advanced electronics with thermal management to maintain consistent environmental conditions throughout the experiments.

Table 3.1: Specifications for GAMRY 3000 Reference and PT-104 Data Logger

GAMRY 3000 Reference	
Operation limits	±15 V; 3.0 A or ±30 V; 1.5A
Potential applied accuracy	±1 mV ±0.2% of setting
Potential measured accuracy	±1 mV ±0.2% of reading
Current applied / measured accuracy	±5 pA ±0.05% of range
PT-104 Data Logger	
Compatibility	Works with PT100 and PT1000 sensors
Accuracy (unit of 23 ± 2 °C)	0.015 °C + 0.01% of reading
Resolution	0.001 °C

3.2.1 Components of Calorimeter setup

- **Heat flow sensor**: The battery tester is used to perform electrochemical tests on LIB cells such as charging and discharging cycles. The heat flow measurements (in mV), cell voltage output (V), and current (A) are measured using the GAMRY.

- **Twin calorimeter configuration:**: Temperature and heat flow measurement recorder in degrees Celsius and millivolt respectively.

- **Heat sinks**: Multimeter used to measure voltage and resistance of sample in Volts and ohms respectively.

- **Temperature regulator**: Jalabo temperature regulator is used to achieve a temperature controlled environment where water circulates into the calorimeter at a desired temperature.

- **Copper sheets**: Copper sheets with high thermal conductivity is attached to the heat flow sensors as to increase heat transfer

- **Thermal pads**: Similar to the copper sheets, the thermal pads with high thermal conductivity is attached to both the heat flow sensors and copper sheets to increase heat transfer

- **Testing jig**: A customized cell holder was designed and partially fabricated using 3D printing technology to securely mount the dummy cell for calorimetric experiments. This holder ensures mechanical stability and optimal thermal contact between the cell and the calorimeter, thereby enhancing the accuracy and reproducibility of heat measurements.

- **Dummy cell**: Dummy cell was employed to replicate the thermal and electrical behavior of a real 4695 format lithium-ion battery cell without the risks associated with active battery chemistry. This dummy cell is designed to exhibit a similar heat dissipation profile and internal resistance as an operational battery but contains no electrochemical materials.

  The use of such a chemically inert dummy cell is a good safety measure. It eliminates hazards such as thermal runaway, leakage, or explosion that could arise during prolonged testing or calibration procedures. Moreover, it provides a stable and reproducible platform for calibrating the calorimeter apparatus and validating measurement methods. The dummy cell employed in this study was designed to replicate the thermal and electrical response of the commercial lithium-ion cell, enabling safe experimental calibration under controlled laboratory conditions. Its similarity in heat dissipation behavior ensures that the calorimetric setup could be effectively validated before measurements on real cells.

  By utilizing the dummy cell, the experimental setup can be thoroughly characterized under controlled conditions, ensuring the accuracy and reliability of subsequent thermal measurements performed on real battery cells. This approach enables the detection of systematic errors and noise sources in the measurement system while maintaining a safe laboratory environment.

3.3 Method to evaluate discrepancy between both techniques

The methodology for measuring difference in results and acceptance threshold definition consists of four main steps, as described below.

Step 1: Reference Mean Calculation

The reference mean entropic coefficient from cell 1 and cell 2, $\overline{EC}(x)$, at each state of charge (x) is calculated as:

$$\overline{EC}(x) = \frac{EC_1(x) + EC_2(x)}{2} \tag{3.1}$$

Step 2: Reference RMSE Calculation

The reference root mean square error (RMSE) at each x is then computed as:

$$RMSE_{\text{ref}}(x) = \sqrt{\frac{(EC_1(x) - \overline{EC}(x))^2 + (EC_2(x) - \overline{EC}(x))^2}{2}} \tag{3.2}$$

Step 3: Global Threshold Establishment

The maximum standard deviation threshold, $\sigma_{\max}$, is defined as the maximum RMSE value across all states of charge:

$$\sigma_{\max} = \max\{RMSE_{\text{ref}}(x)\}, \quad \forall x \in [0, 100]\%\ SOC \tag{3.3}$$

Step 4: Acceptance Criteria Definition

The calculated RMSE for each dataset, $RMSE_{\text{ref}}(x)$, is evaluated against the defined thresholds according to the following criteria:

$$RMSE_{\text{ref}}(x) = \begin{cases} \text{Acceptable,} & RMSE_{\text{ref}}(x) \leq \sigma_{\max} \quad (\pm 1\sigma \text{ threshold}) \\ \text{Marginally Acceptable,} & \sigma_{\max} < RMSE_{\text{ref}}(x) \leq 2\sigma_{\max} \quad (\pm 2\sigma \text{ threshold}) \\ \text{Unacceptable,} & RMSE_{\text{ref}}(x) > 2\sigma_{\max} \end{cases} \tag{3.4}$$

3.4 Simulation Setup

The case studies for the modeling and simulation part of this work consists of:

- Battery Model (EECM)
- Battery Thermal Model
- BTMS

The first step in the work was creating a model that combined several models to predict the temperature in the LIBs. Each of these models requires a different set of steps, which are eventually combined in order to achieve the desired result. The electrical equivalent circuit model (EECM) was initially chosen. According to the EECM model, it is necessary to first determine the initial model parameters, which include the resistances, capacitances, and OCV with the function of the SOC. The electrical equivalent circuit model was used to determine the heat generation of the cell for various c-rates, after the initial model parameters were estimated. To make sure the EECM model was accurate, it was verified with the help of experimental data. BTMS was then modeled at the cell level within the battery thermal model. It was used to control the cell's thermal characteristics. In simulations, the BTMS system was utilized to examine various cell operation conditions and identify limitations of air or liquid cooling. The result can be found in the results section.

3.5 Electrical Equivalent Circuit Modeling

In this section, we will look into how the parameters for the ECM is determined and how it is implemented in COMSOL to obtain the heat generation of the cell at various C-rates.

3.5.1 Parameter Estimation

The accuracy of the ECM is dependent on the parameters in the model. The parameters are identified using measurement data obtained from the GITT test that was performed by VOLVO. These tests were conducted under various conditions, such as varying temperatures and C-rates. The parameters identified in this tests were R0, R1, R2, C1, C2 and OCV. When an arbitrary magnitude pulse current is applied to the cell, the corresponding voltage response is as illustrated in figure 3.2. The data correlation shown in figure 3.2 represents the relationship between the state of charge (SOC) and the open circuit voltage (OCV). The OCV and SOC values are determined during the rest periods, when no current is applied and the terminal voltage has reached a steady state, ensuring that the measurements reflect the equilibrium behavior of the cell. The R0 impacts the instantaneous response, while the RC parallel networks impact the delayed response.

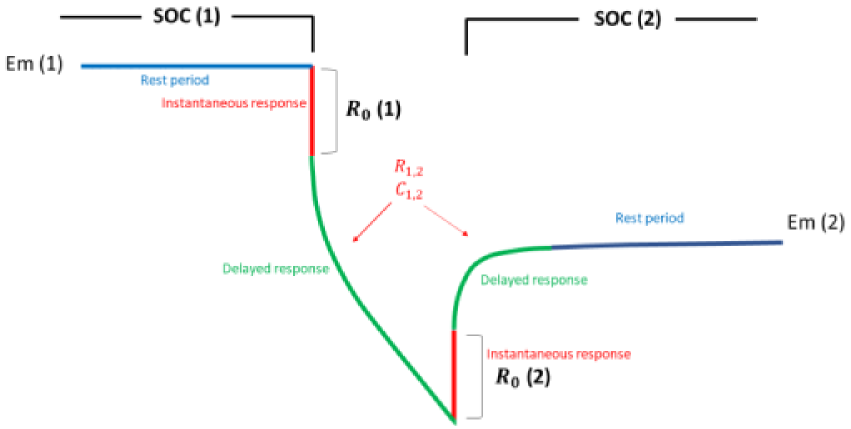

Figure 3.2: ECM data correlation [14].

The values were then transformed into readable information (look up tables) using MATLAB and then exported as a text file for modeling the ECM in COMSOL.

- **R0**: It stands for the battery's ohmic resistance. In addition to producing a voltage drop proportional to the current, it also creates a leap in voltage at the start of the current step.

- **R1 & R2**: It represents charge transfer and diffusion resistance of the cell. These resistances contribute to transient voltage behavior (voltage relaxation after current changes).

- **C1 & C2**: It denotes the capacitive behavior at the electrode/electrolyte interface in the RC networks. It dictates the time constants of the battery's dynamic response.

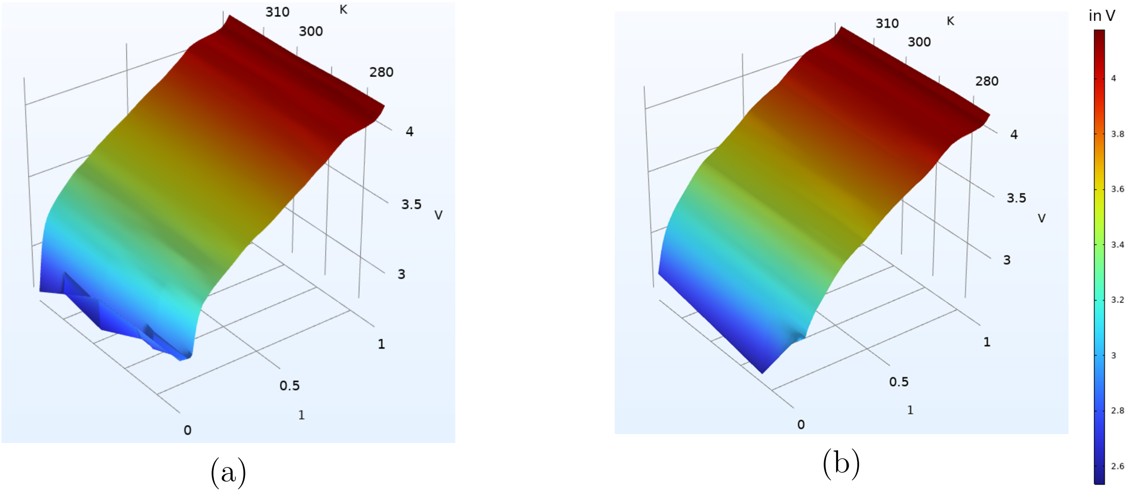

(a) (b)

Figure 3.3: OCV obtained at different conditions as function of temperature and SOC during a) charging and b) discharging.

OCV (depicted in figure 3.6) and R0 are temperature and SOC-dependent factors, whereas R1,R2,C1, and C2 are temperature, SOC, and current-dependent variables. All of the parameters for the four distinct temperatures for charge and discharge were estimated for the cell at various SOCs.

3.5.2 EECM Modeling

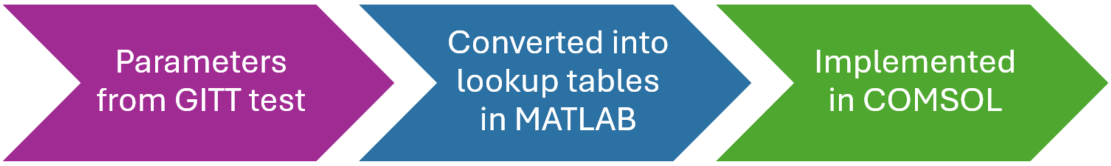

Figure 3.4: ECM modeling Workflow

Figure 3.4 represents the flow of work done for constructing the EECM model. The data from the GITT test was transformed into readable data using a MATLAB script. The data was saved as a text file and subsequently imported into COMSOL to define the ECM, where the irreversible heat was estimated using the parameters extracted from the GITT test. In COMSOL, under the "Electrochemistry → Batteries" branch of the Physics interface, the "Electrical Circuit" block is used to represent the Equivalent Electrical Circuit Model (EECM) in our study. The model parameters are then imported into COMSOL as an interpolation function. The parameters R1, R2, C1, and C2 are defined as functions of SOC, OCV, Temperature, and Current, while OCV and R0 are defined as functions of SOC and temperature.

Finally, these parameters are assigned to each component that collectively make up the electrical circuit component in COMSOL Multiphysics shown in figure 3.5.

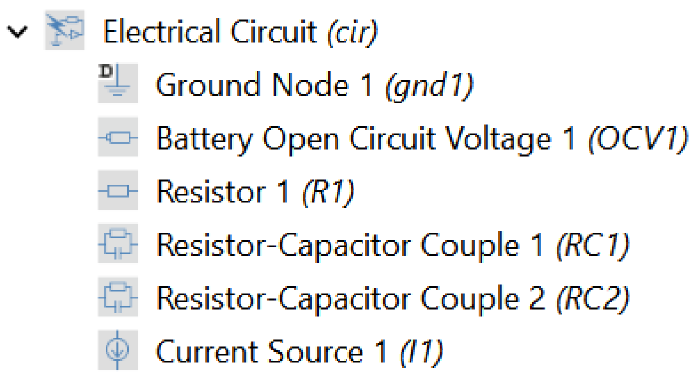

Electrical Circuit *(cir)*
- Ground Node 1 *(gnd1)*
- Battery Open Circuit Voltage 1 *(OCV1)*
- Resistor 1 *(R1)*
- Resistor-Capacitor Couple 1 *(RC1)*
- Resistor-Capacitor Couple 2 *(RC2)*
- Current Source 1 *(I1)*

Figure 3.5: ECM modelled in COMSOL Multiphysics.

The components shown in figure 3.5 are connected in series to represent the ECM depicted in figure 2.3. The components are defined using look-up tables which are imported in to COMSOL from MATLAB. For example, R0 gets allocated to a resistor block R1, while R1 and C1 are allocated to the Resistor-Capacitor couple RC1 and R2 and C2 are assigned to the the Resistor-Capacitor couple RC2. Finally, a current is provided in the current source block I1 in the EECM to determine voltage response and irreversible heat generation from the battery cell. There are localized heat generated at each component of the ECM. The total irreversible heat generated obtained is the sum of heat obtained from different components as shown in (3.5).

$$Q_{\mathrm{ir}} = cir.R_1.q + cir.R_{C1}.q + cir.R_{C2}.q \tag{3.5}$$

where Q_{irr} denotes the irreversible heat generated by the cell for different C-rates, cir represents the name of the electrical circuit as shown in figure 3.5, R_1 represents the component name and q represents the heat obtained from the component.

For the reversible heat, the entropic coefficients obtained from the calorimetric and potentiometric experiments were defined into the OCV1 block as shown in figure 3.6. The term $dEOCV$ denotes the entropic coefficients and OCV_LUT denotes the open-circuit voltage obtained from the GITT test. The reversible heat is calculated by taking the localized heat generated in the OCV block as $cir.OCV\_1.q$.

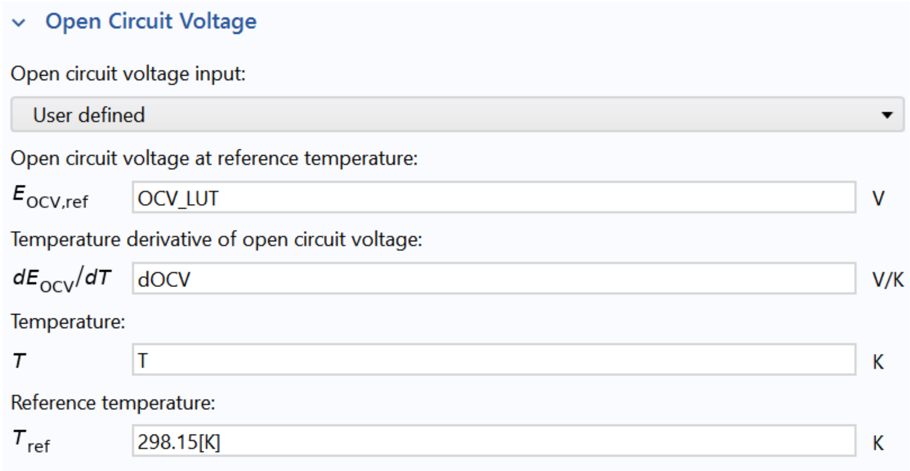
Open Circuit Voltage

Open circuit voltage input:
User defined

Open circuit voltage at reference temperature:
$E_{OCV,ref}$ OCV_LUT V

Temperature derivative of open circuit voltage:
dE_{OCV}/dT dOCV V/K

Temperature:
T T K

Reference temperature:
T_{ref} 298.15[K] K

Figure 3.6: Defining the Battery Open Circuit Voltage 1 block.

3.6 3D Thermal Model

The thermal model has been developed based on the electrical properties of the EECM. This model aims to simulate the heat transfer processes occurring within and out of the cell. During battery operation, heat generation arises from various energy conversion mechanisms, including chemical reactions, electrical processes, and mass transport phenomena. Accurate prediction of both cell temperature and heat generation rate is essential for constructing a reliable thermal model.

The VOLVO cell simulation team has previously developed comprehensive 3D thermal models for both prismatic and 21700 lithium-ion cells using COMSOL Multiphysics. The present work builds upon these existing simulations. This section provides an overview of the methodology employed to derive the thermal model from the previously established COMSOL-based cell simulations.

3.6.1 Modeling Thermal Model

With the heat generated by the ECM, the primary goal of our model was to illustrate the temperature distribution within the battery cell using the minimal amount of thermal properties that were accessible to us.

3.6.1.1 Geometry

A lumped 3D CAD model of the battery cell was developed to represent its geometry as described in figure 3.7, incorporating key structural components such as the jelly roll, mandrel, current collectors, outer casing, and terminals. The model geometry was defined based on dimensional measurements obtained from CT-scan imaging. Each component was assigned a corresponding material, determined through CT-scan analysis of the cell. The jelly roll was represented using lumped material properties to capture the overall thermal behavior of the electrochemical layers without explicitly modeling individually. The thermal properties of components such as the current collectors and cell assembly parts were estimated using reasonable engineering assumptions (described in Section 3.6.1.2) and assigned accordingly. Distinct material properties were also defined for the outer casing, terminal, and mandrel. The complete list of materials and their associated thermal properties is summarized in Table 3.2.

Table 3.2: List of Components with Corresponding Materials

Component	**Material Assigned**
Terminal	Aluminum
Cell assembly components and air	Combined properties of air, rubber, and metals
Positive current collector and air	Combined properties of air and copper (70-30 ratio)
CAN	Stainless steel
Jelly Roll	Material with properties of the cell
Mandrel	Air
Negative current collector and air	Combined properties of air and aluminum (70-30 ratio)

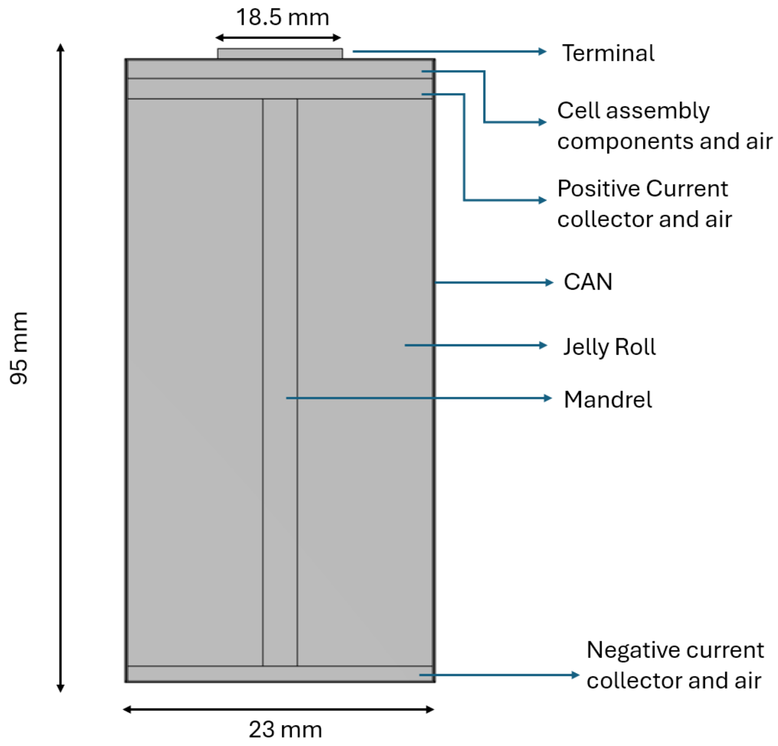

Figure 3.7: 3D Geometry of the 4695 cell

3.6.1.2 Heat Transfer

The heat transfer in this study can be differentiated into two:

- Heat transfer within the battery cell.
- Heat transfer from the battery cell to the surroundings.

To accurately capture heat propagation within the battery cell, the heat generated by the ECM was uniformly distributed across the entire jelly roll, as illustrated in figure 3.8. thermal properties, such as thermal conductivity for components, including the can, mandrel, and terminal were defined using COMSOL's internal material library. For the remaining components, the effective thermal conductivity was determined through analytical estimation, calculated using (3.6).

$$k_{eq} = \frac{k_1 A_1 + k_2 A_2}{A_1 + A_2} \tag{3.6}$$

where k_1 represents the equivalent (effective) thermal conductivity, k_1,k_2 denotes the thermal conductivities of material 1 and material 2 and A_1,A_2 represents the cross-sectional areas of the materials perpendicular to heat flow.

To monitor the temporal variation of the cell's internal temperature, a temperature probe was placed at the geometric center of the jelly roll, recording data at one-second intervals. The temperature measured by this probe was used as input to the EECM, as the model parameters vary dynamically with changes in cell temperature. This setup establishes a feedback loop in which the EECM continuously updates its parameters based on the real-time temperature within the battery cell, as illustrated in figure 3.9.

To enable this coupling, the EECM parameters were defined as functions of the probe temperature, ensuring that the model accurately represents the temperature-dependent behavior of the cell and that parameter variations correspond to the thermal state of the system.

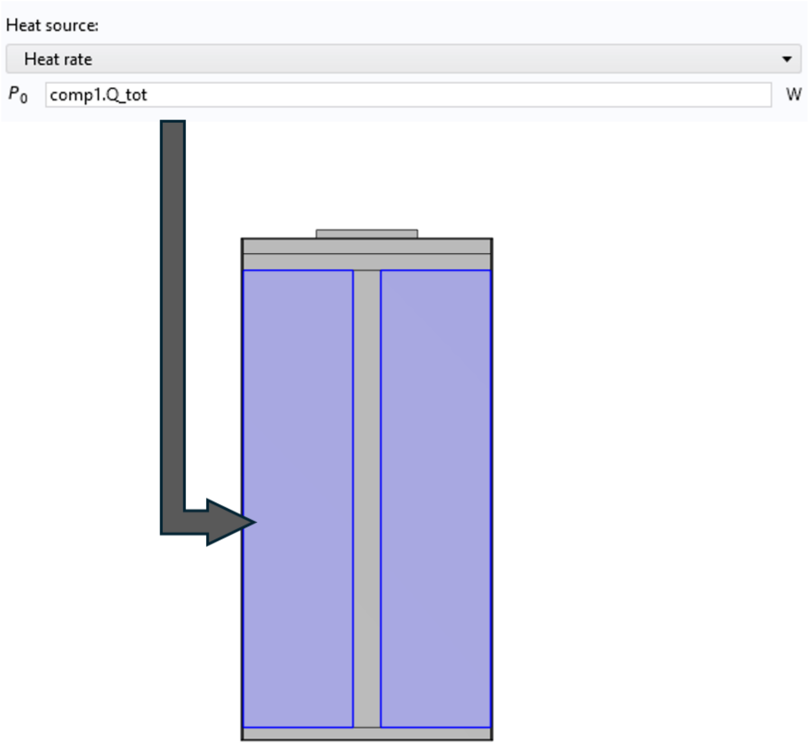

Heat source:

Heat rate

P_0 comp1.Q_tot W

Figure 3.8: EECM Heat Input to Jelly Roll in 3D Thermal Model

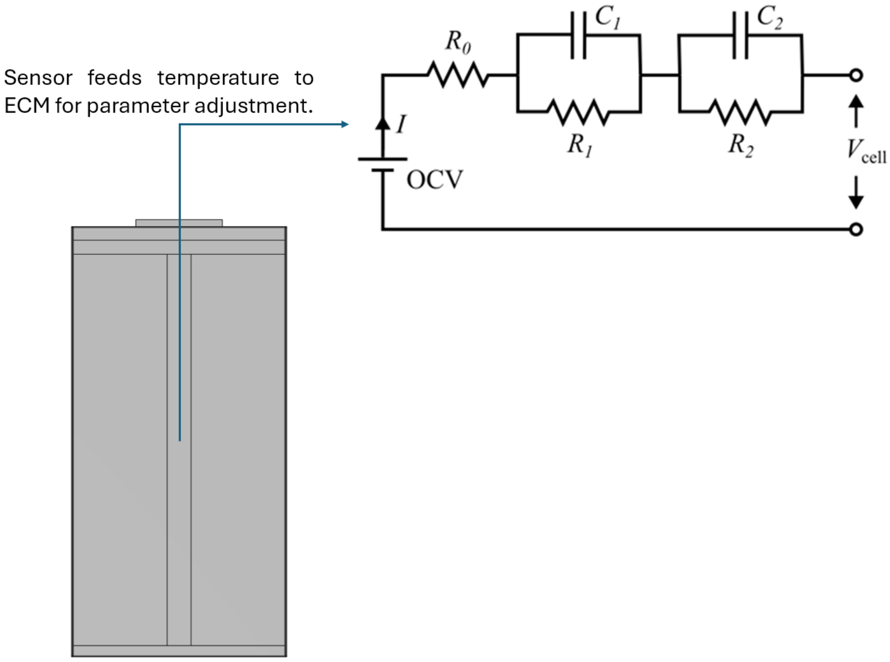

Sensor feeds temperature to ECM for parameter adjustment.

Figure 3.9: Temperature sensor feedback to update ECM parameters.

In COMSOL Multiphysics, within the "Heat Transfer" physics module, the "Heat Transfer in Solids" interface is employed to model thermal interactions. In this interface, the heat transfer coefficient (HTC) is applied to the outer surfaces of the cell to represent convective heat exchange with the surrounding environment. The procedure for defining the heat transfer coefficient as a boundary condition is illustrated in Figure 3.10. The heat transfer coefficient is a critical parameter that governs the rate at which heat is exchanged between the battery cell and its surrounding environment. Conceptually, it serves as a thermal bridge between the cell and its surroundings, controlling how efficiently the cell dissipates the heat generated during operation.


Heat Flux

Flux type:

Convective heat flux

Heat transfer coefficient:

User defined

Heat transfer coefficient:

h 10 W/(m²·K)

External temperature:

T_{ext} User defined

298.15[K] K

Figure 3.10: Assignment of Heat Transfer Coefficient in COMSOL Model

In this study, the heat transfer coefficient was determined and subsequently adjusted as a function of the C-rate, since the rate of heat generation is highly dependent on the charging and discharging intensity of the cell. By adapting the coefficient to reflect varying operating conditions, the thermal model can more accurately reproduce the cell's real-world thermal behavior. The primary objective of tuning this parameter is to maintain the cell within its safe operating temperature range, thereby preventing overheating and ensuring consistent and reliable performance during operation.

3.6.1.3 Simulation Configuration

- The external surfaces of the cell are subjected to natural convection with a heat transfer coefficient of 10 $\mathrm{W/(m^2 \cdot K)}$.
- Ambient temperature is set to 298.15 K.
- The initial voltage of the cell was set to 2.8 V, and a negative current (varying according to the C-rate) was applied to the model to simulate the charging process. (In COMSOL Multiphysics, a positive current conventionally represents current flowing out of the model. Therefore, during battery charging—where current flows into the cell—the applied current is defined as negative within the simulation framework.)

- A time-dependent solver was employed to solve the model, with the total simulation time determined by the C-rate, since the charge duration varies inversely with the applied current rate.

3.7 Battery Cooling Strategy

When different cooling strategies are applied in the model, the heat transfer coefficient varies across the outer surfaces of the battery cell. For example, in a single-sided cooling configuration, the surface of the cell is in direct contact with the cooling tube exhibits a significantly higher heat transfer coefficient than the remaining sides, which are exposed only to ambient air. Due to the presence of a vent at the bottom of the cell, bottom cooling is not feasible.

To investigate the influence of these variations on the cell's thermal behavior and internal temperature distribution, three distinct cooling strategies were simulated for the 4695 battery cell: top cooling, single-sided cooling, and double-sided cooling. These simulations were conducted to analyze the resulting temperature gradients within the cell and to assess the relative effectiveness of each strategy in managing heat dissipation and maintaining thermal uniformity.

The primary difference between the simulation setups for each cooling strategy lies in the location of heat removal from the cell surfaces. Depending on the selected cooling configuration, a higher heat transfer coefficient is assigned to the surfaces in contact with the cooling tube depicted in figure 3.11, representing enhanced convective cooling. In contrast, the remaining surfaces are assigned lower coefficients corresponding to natural convection with the surrounding air.

- Single-sided cooling : Since only one side of the cell is in contact with the cooling tube, that portion of the surface is assigned a higher heat transfer coefficient, while the remaining surfaces maintain lower values corresponding to natural convection.

- Double-sided cooling : When both sides of the cell are exposed to cooling, these surfaces are assigned higher heat transfer coefficients, while the remaining surfaces retain lower values representative of natural convection.

- Top cooling : In the case of top cooling, the terminal of the cell is the primary surface exposed to the cooling system. Consequently, the terminal surface is assigned a higher heat transfer coefficient, while the remaining surfaces are exposed to natural convection and retain lower values.

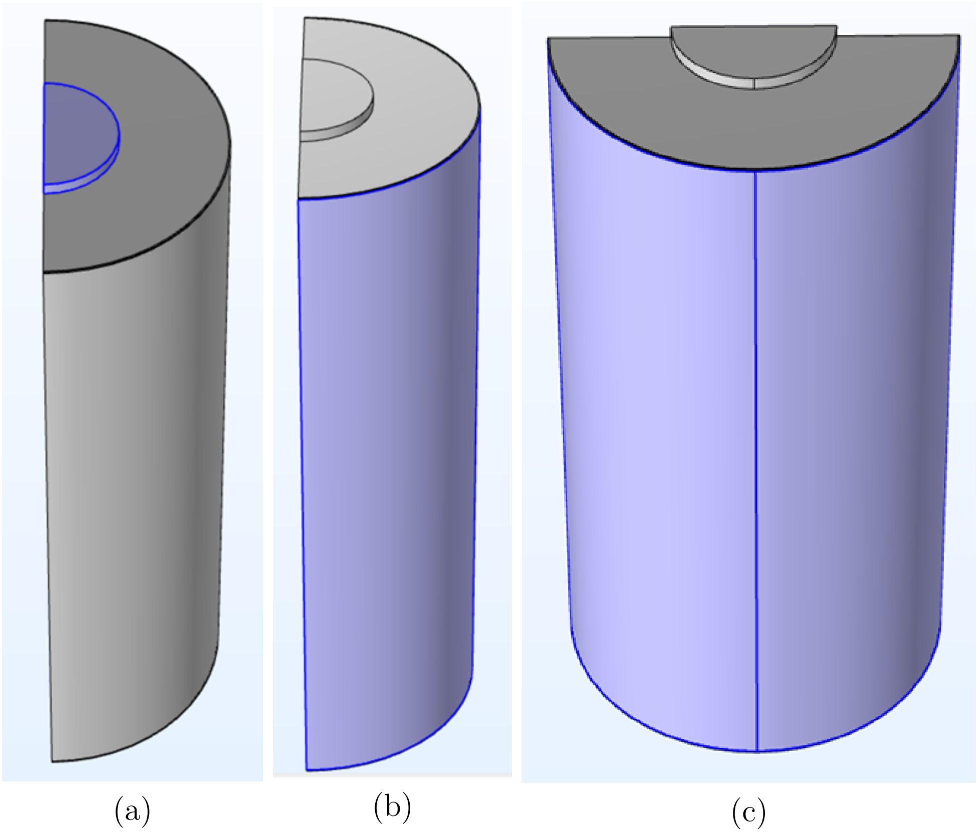
(a) (b) (c)

Figure 3.11: Heat flux removal representation of a) Top, b) Single-sided and c) Double-sided cooling.

The heat transfer coefficient (HTC) can be calculated using the formula:

$$h = \frac{Q}{A\,\Delta T} \tag{3.7}$$

where:

- h — **Convective heat transfer coefficient** ($\mathrm{W/m^2 \cdot K}$)
- Q — **Heat transfer rate** (W)
- A — **Surface area** ($\mathrm{m^2}$)
- ΔT — **Temperature difference** (K or °C)

For a cylinder, the curved surface area is (double-sided cooling):

$$A = 2\pi r h = 2\pi \times 23 \times 93.5\,\mathrm{mm}^2 \approx 13,521.6\,\mathrm{mm}^2 = 0.0135216\,\mathrm{m}^2$$

Given (for 1.5C-rate):

$$Q = 10.5\,\mathrm{W}(\text{from figure 4.27(b)}), \quad \Delta T = 10\,^\circ\mathrm{C}\ (\text{desired temperature} = 40^\circ\mathrm{C})$$

Substitute the values:

$$h = \frac{10.5}{0.0135216 \times 10} = \frac{10.5}{0.135216}$$

$$h \approx 78\,\mathrm{W/m^2 \cdot K}$$

3.7.1 Simulation Configuration

- All external surfaces of the cell except the surface that is in contact with the cooling tube, were subjected to natural convection with a heat transfer coefficient of 10 $\mathrm{W/(m^2 \cdot K)}$.

- The heat transfer coefficient for the cooling tube is determined using (3.7).
- Ambient temperature is set to 298.15 K.

- Initial voltage of the cell is set to 2.8 V and negative current (varies with respect to C-rate) is fed into model in order to charge the cell.

- A time-dependent solver was employed to solve the model, with the total simulation time determined by the C-rate, since the charge duration varies inversely with the applied current rate.

3.7.2 Cell-Level Simulation for Module Analysis

In real-world conditions, where battery cells are closely packed, heat dissipation to the ambient is minimal. The surrounding cells act as thermal barriers, limiting heat transfer from individual cells to the environment. As a result, the module tends to exhibit a more uniform temperature distribution, as heat is shared among the cells. To capture this behavior, an additional simulation was conducted with an optimized contact area between the cooling tube and the cells, allowing for more realistic representation of heat transfer within the module.

The two main factors considered to simulate the module-level cooling strategy are:

- Bending radius of the cooling tubes
- Temperature gradient of the cell.

3.7.2.1 Modeling

The cooling side of the cell is partitioned to replicate the cooling area of the cell in real world as shown in figure 3.13. The contact area between the cell and cooling tube was defined using an inscribed angle as shown in figure 3.12.

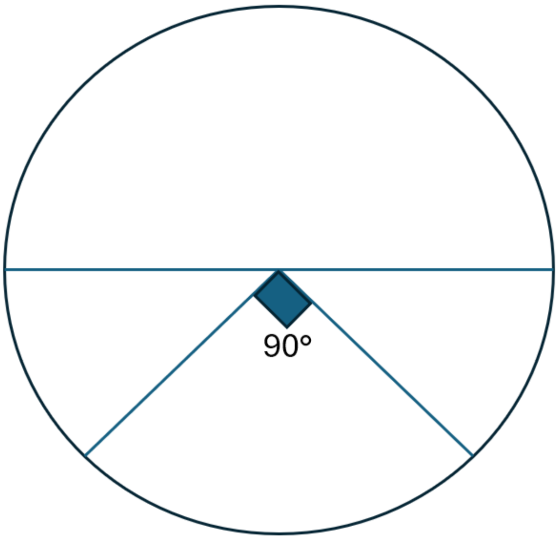

Figure 3.12: Inscribed angle depicting the cooling area

Using this angle, the arc length of the cooling tube is determined as shown in (3.8). As a result, an independent heat flux removal value is provided for this arc length in order to recreate the cooling tube contact. The cooling area is then calculated using the arc length and height of the cylinder to determine the amount of heat flux required to be removed.

$$L = \frac{\theta}{360^\circ} \times 2\pi r \tag{3.8}$$

In this case the angle is 90° and the radius is 23 mm. So the arc length or the contact length of the cooling tube and the cell is

$$L = \frac{90^\circ}{360^\circ} \times 2\pi \times 23mm \tag{3.9}$$

$$L = 36.11mm. \tag{3.10}$$

Similarly, for 60° the contact length is 24.07 mm.

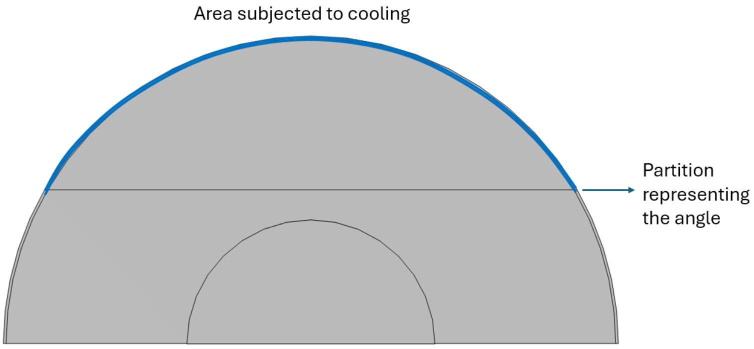

Figure 3.13: Thermal Model representing the cooling contact area for 90°.

Initially, the temperature of the cooling surfaces was fixed at 25°C, corresponding to the cooling tube temperature used at a 1C-rate. A surface integration of the battery cell cooling surface at a fixed temperature of 25°C was performed to evaluate the thermal conductance of the cell surface. The result, expressed in W/K, represents the effective heat transfer rate per unit temperature difference across the surface. The resulting thermal conductance, expressed as a function of time, was subsequently divided by the cooling surface area to calculate the time-varying heat flux necessary to effectively remove heat from the cell.

Since we use double-sided cooling, the cooling area for 90° is

The curved surface area (CSA) of a cylinder is given by,

$$\text{CSA} = \pi r h$$

Substituting the given values, $\pi r = 36.11\,\text{mm}$ (from (3.10)) and $h = 93.5\,\text{mm}$:

$$\text{CSA} = 36.11 \times 93.5$$

$$\text{CSA} \approx 3373.3\,\text{mm}^2$$

Similarly, for 60° the cooling surface area is $2250.55\,\text{mm}^2$.

$$h = \frac{G_{\text{th}}}{A} \tag{3.11}$$

where

$$\begin{aligned} h &= \text{heat transfer coefficient (W/m}^2\text{K)}, \\ G_{\text{th}} &= \text{thermal conductance (W/K)}, \\ A &= \text{curved surface area (m}^2\text{)}. \end{aligned}$$

Using (3.11), the varying heat flux needed to maintain the surface at 25°C is calculated.

3.7.2.2 Simulation Configuration

- All external surfaces of the cell except the surface that is in contact with the cooling tube, are thermally insulated with a heat transfer coefficient of 0 $\text{W}/(\text{m}^2 \cdot \text{K})$.

- The heat transfer coefficient for the cooling tube is determined as shown in (3.11).

- Ambient temperature is set to 298.15 K.

- Initial voltage of the cell is set to 2.8 V and negative current (varies with respect to C-rate) is fed into model in order to charge the cell.
- A time-dependent solver was employed to solve the model, with the total simulation time determined by the C-rate, since the charge duration varies inversely with the applied current rate.

The cooling strategy was simulated for contact angles of 90° and 60°. As the contact length of the cooling tube decreases, the heat flux required to be removed from the cell increases. In these simulations, heat transfer to the ambient was assumed to be zero to replicate a worst-case scenario. Initially, the fixed heat flux was determined based on the maximum heat generation of the cell. However, applying this same flux during periods of lower heat generation could cause the cell temperature to drop below 25°C. To prevent this, a time-varying heat flux removal strategy was implemented, enabling the cooling system to adjust according to the instantaneous heat generation and maintain the cell temperature within the safe operating range.

4

Results

4.1 Open circuit voltage

The OCV-SOC relationship was established through low-rate charging and discharging cycles at 0.05C, with voltage values averaged to minimize hysteresis effects and measurement uncertainties. Figure 4.1 presents the experimental results showing charge voltage, discharge voltage, and the estimated OCV curve across the full SOC range.

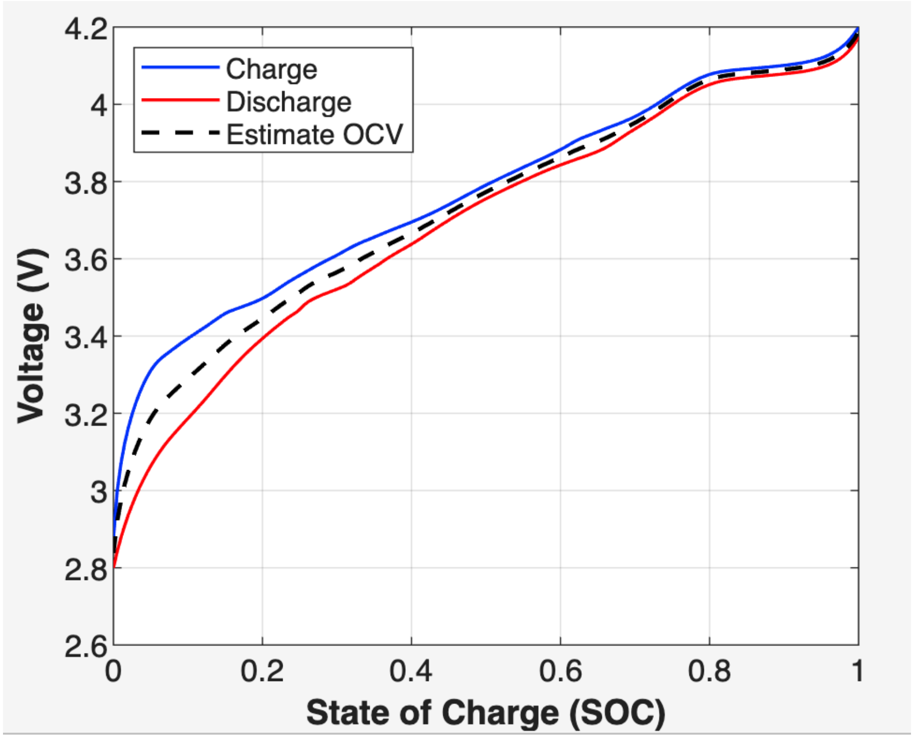

Figure 4.1: OCV-SOC relationship derived from 0.05C charge and discharge cycles

The obtained OCV curve exhibits the characteristic non-linear voltage-SOC relationship typical of lithium-ion batteries, with a voltage range spanning from 2.8V to 4.18V across 0-100% SOC. The curve demonstrates three distinct regions: steep voltage gradients at low SOC (0-0.1) and high SOC (0.95-1.0), and a more linear relationship in the intermediate range. This behavior aligns with findings reported in literature [32] [33], who observed similar voltage characteristics in lithium-ion cells under quasi-equilibrium conditions.

The hysteresis effect, evident as the voltage difference between charge and discharge curves, is most pronounced in the 0-0.4 SOC range with a maximum deviation of approximately 50mV. The estimated OCV curve serves as the fundamental reference for subsequent SOC estimation accuracy evaluation and battery management system

4.2 Calibration Coefficient

The calorimeter calibration was conducted to establish a reliable conversion between the sensor electrical output (millivolts) and the corresponding thermal power dissipated by the cell (watts). A dummy cell was used inside a temperature-controlled incubator at 25°C to minimize thermal fluctuations.

The calibration protocol involved initially discharging the dummy cell at 0.05 C to 2.8 V, followed by a 60-hour rest period to reach thermal and electrochemical equilibrium. Subsequently, the sensor voltage was recorded for a series of known power inputs applied by a DC power supply: 0.1, 0.4, 0.8, 2.1, 7.5, and 10 W (figure 4.2). For each power level, the average millivolt output and the calibration coefficient (W/mV) were computed (table 4.1). After calibration, the dummy cell was recharged at 0.5 C for 30 minutes to restore baseline conditions.

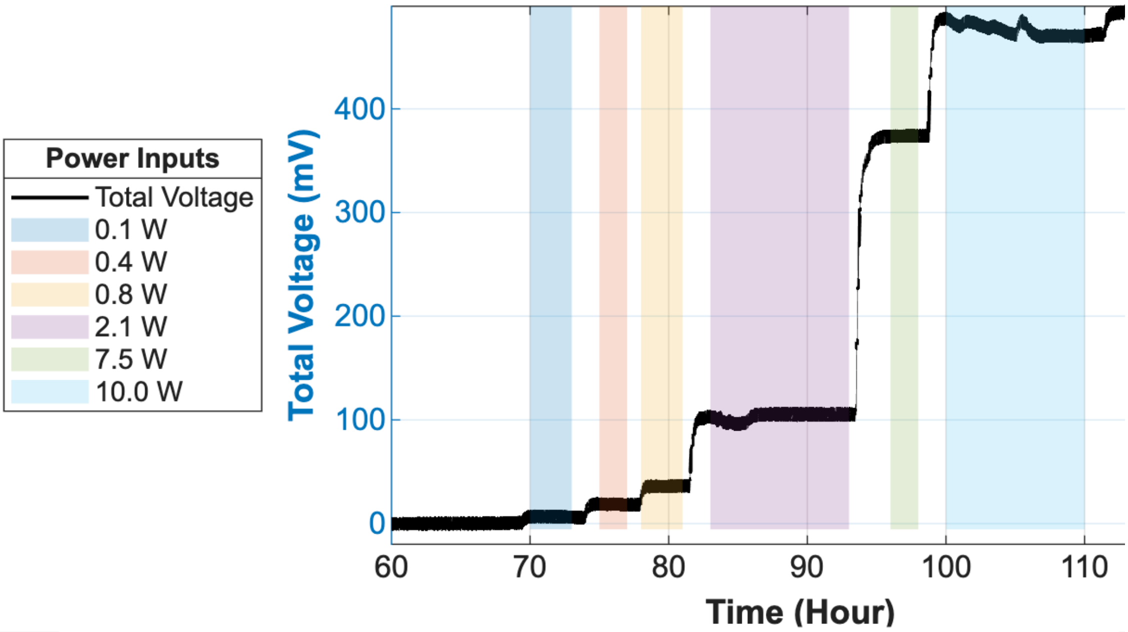

Figure 4.2: Measured voltage with variation in power input for calibration

Initial calibration results revealed notable variability and instability, especially at low power inputs. At 0.1 W, the calibration coefficient peaked around 28.6 W/V with a coefficient of variation (CV) exceeding 84%, indicating dominant measurement noise and offset effects. For higher power levels (0.4 W and above), the coefficient stabilized between approximately 20 and 23 W/V, with CVs dropping below 20%, achieving excellent precision and reduced measurement variance (table 4.1). This trend highlights that noise and background offsets significantly impact low signal levels but become negligible as power—and thus signal amplitude—increases.

Table 4.1: Calibration coefficients and variability at different power inputs.

Power (W)	Avg Voltage (mV)	Calibration Coef. (W/V)	Std. Dev. (W/V)	CV (%)
0.1	5.84	28.59	24.15	84.48
0.4	17.71	23.40	4.44	18.99
0.8	34.73	23.29	2.56	10.97
2.1	102.55	20.52	0.97	4.70
7.5	373.05	20.11	0.18	0.89
10.0	475.37	21.04	0.28	1.34

To mitigate measurement noise and baseline offsets, a correction procedure was applied. This included offset subtraction and signal filtering, significantly reducing variance and improving calibration coefficient stability across all power levels, particularly at the challenging low-power end. Post-correction results (table 4.2) show more consistent calibration coefficients clustered around 20–22 W/V with notably decreased standard deviations (figure 4.3 and figure 4.4) and CVs.

Table 4.2: Calibration results after noise offset correction.

Power (W)	Avg Voltage (mV)	Avg Calibration Coef. (W/V)	Std. Dev. (W/V)
0.10	6.59	19.73	0.56
0.40	18.48	21.65	0.30
0.80	35.43	22.64	1.31
2.10	103.31	20.35	0.67
7.50	373.81	20.06	0.01
10.00	476.13	21.00	0.24

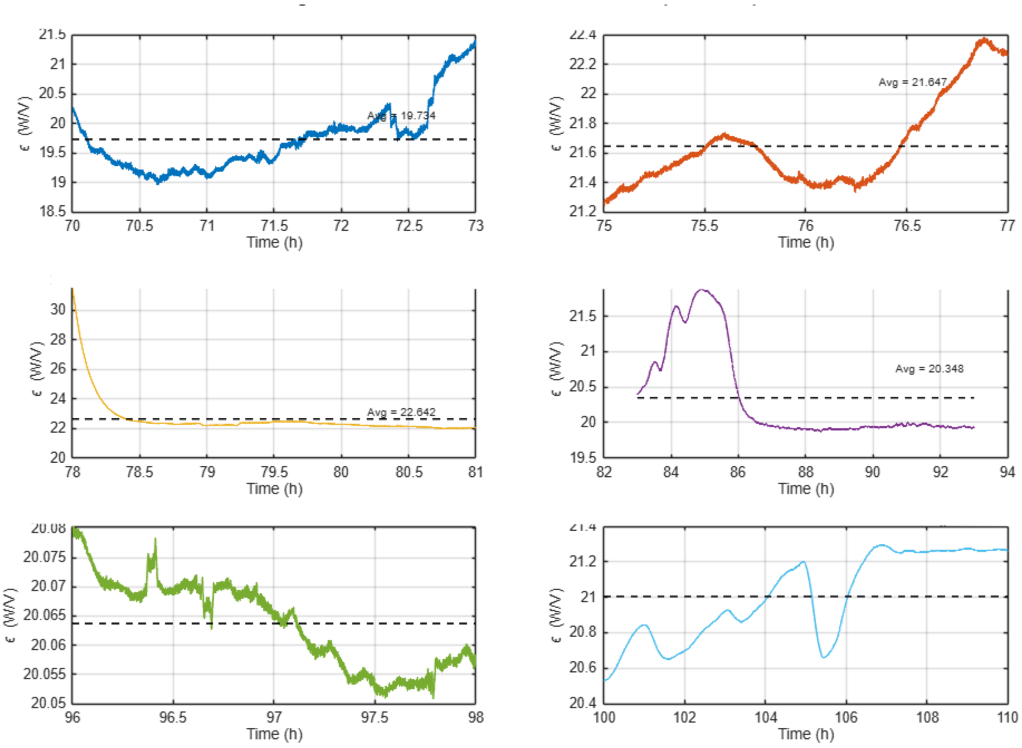

Figure 4.3: Identified calibration coefficient with variation in power input for calibration. The panels correspond to increasing power levels from left to right and top to bottom: (1) 0.10 W, (2) 0.40 W, (3) 0.80 W, (4) 2.10 W, (5) 7.50 W, (6) 10.00 W.

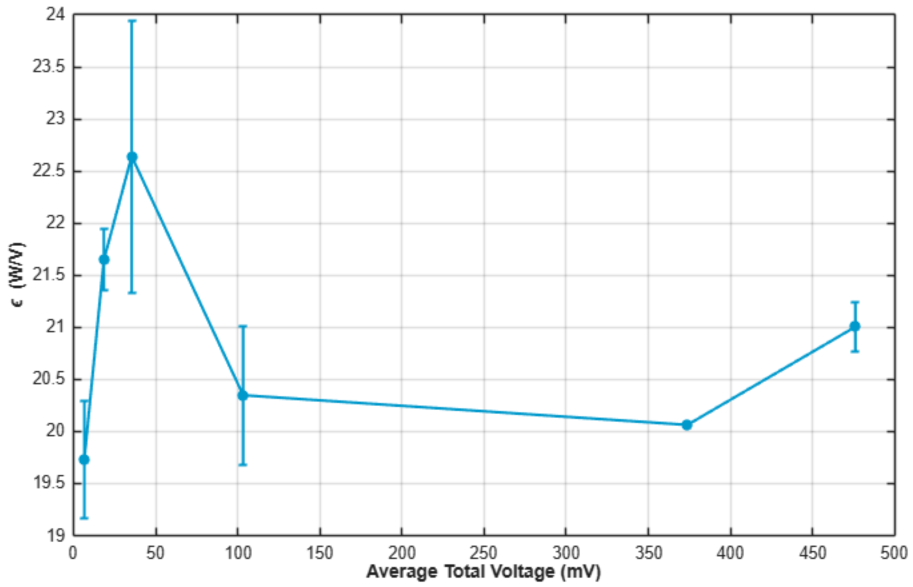

Figure 4.4: Standard deviation for calculated epsilon values

4.3 Heat generation

The large format lithium-ion battery (LIB) cell tested here, with a capacity of 33 Ah, was cycled between 2.8 V and 4.2 V. The heat flow measurements reveal clear differences in thermal behavior during charging and discharging, as shown in Figures 4.6 to 4.8. In summary, the initial calibration highlighted system limitations due to measurement noise and baseline offsets, especially at low power levels where errors reached nearly 67%. After applying offset correction and noise filtering, calibration demonstrated improved precision and stability with errors falling below 4% for moderate to high power inputs. This correction significantly enhanced the linearity and accuracy of the calorimeter, enabling reliable thermal power measurements essential for precise battery thermal characterization and modeling.

During charging, heat generation is predominantly positive, reflecting exothermic processes. Discharging, however, shows more complex thermal behavior, with both exothermic and endothermic signals appearing. Sharp peaks often coincide with changes in current or internal resistance.

A key observation is the asymmetrical thermal response between charging and discharging, especially at higher C-rates. This difference comes from the fundamental electrochemical and mass transport mechanisms active in each mode. When charging, lithium ions must overcome increasing activation barriers to intercalate into already occupied electrode sites [34, 35]. This leads to difference in heat patterns linked to concentration gradients and structural changes as state of charge (SOC) varies.In contrast, during discharge, lithium ions leave the electrode materials, initially requiring less energy but facing growing transport limitations as discharge progresses. Lithium can be easily removed from the anode at initially, but as anode sites empty out, the residual ions have much greater transport limitations due to less available sites in the cathode lattice. This leads to transportation issues, which explains why heat levels rises significantly towards the end of discharge cycle.

4.3.1 Origins of Heat Generation

At very low C-rates (e.g., 0.05C), currents are small and ohmic losses are minimal. Electrochemical reactions proceed near equilibrium, so polarization losses are low. Under these conditions, entropic heat dominates, leading to relatively low and stable heat flow across SOC (figure 4.7, 0.05C curves).

When the C-rate increases to 0.1C, ohmic heating increases significantly due to its quadratic relation with current (figure 4.7). Meanwhile, higher currents promote larger concentration gradients and mass transport limitations, causing additional polarization losses. This is reflected by the elevated baseline heat flow compared to 0.05C .

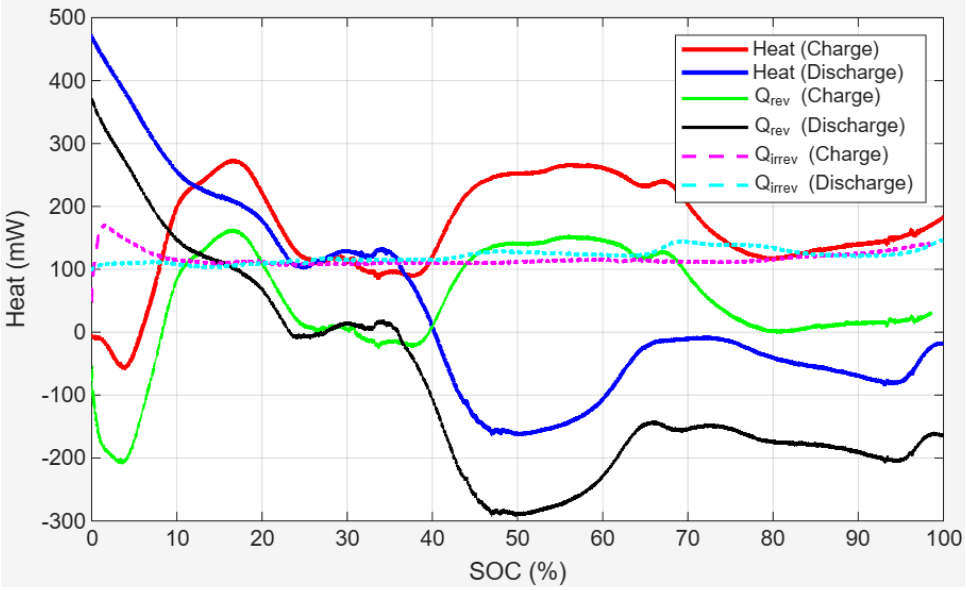

Figure 4.5: Heat flow profile during cycling at C/10.

At high C-rates like 0.3C, resistive and polarization effects dominate heat generation. The thermal output grows nonlinearly with current due to kinetic limitations in ion transport and reaction overpotentials. This results in complex, multi-peak heat signatures as the battery moves further from equilibrium.

4.3.2 Charging Heat Generation Behavior

During charging, the heat flow patterns intensify with increasing C-rate:

- At 0.05C, heat remains low and smooth for most of the cycle, with slight changes reflecting phase transitions and lithium insertion into electrode structures.
- At 0.1C, heat generation increases and shows distinctive peaks at certain SOC levels. These correspond to electrode structural changes or sharp voltage variations, indicating energy consumed by resistive losses and material reorganization.
- At 0.3C, heat generation is substantially higher, with peaks exceeding 1100 mW. The early sharp rise relates to lithium concentration gradients forming, while subsequent peaks reflect complex interactions of internal resistance and evolving mass transport effects.

4.3.3 Discharging Thermal Characteristics

Discharging presents quite different heat profiles:

- At low C-rates (0.05 C), heat flow starts moderately and declines as SOC decreases, illustrating changing thermodynamics and resistance.
- At 0.1 C, heat remains elevated and relatively constant before tapering at the end of discharge, dominated by resistive and polarization heat.
- At 0.3 C, discharge heat peaks above 1500 mW initially, then decays exponentially. This pattern reflects rapid lithium depletion at easy extraction sites

and increasing difficulty maintaining current as concentration gradients become severe. A noticeable heat increase at low SOC suggests mass transport challenges requiring extra energy.

4.3.4 Implications for Thermal Management

The clear dependence of heat generation on C-rate has important practical consequences. Heat output increases nonlinearly with current, meaning thermal management systems must be designed to handle disproportionately higher heat loads during high-power operation. For instance, peak heat at 0.3 C rises more than tenfold compared to 0.05 C, despite only a sixfold increase in current.

Moreover, the asymmetric heat patterns between charging and discharging highlight the need for adaptive cooling strategies that respond to changing SOC and cycling modes. Both peak and average heat rates need consideration: average heat is relevant for steady thermal load, while peaks dictate transient responses and risks such as thermal runaway.

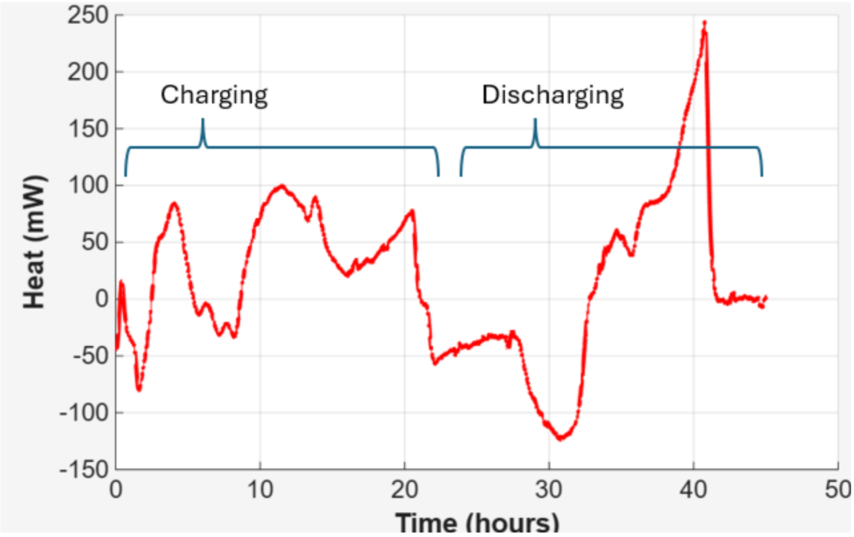

Figure 4.6: Overall heat flow profile during cycling at C/20.

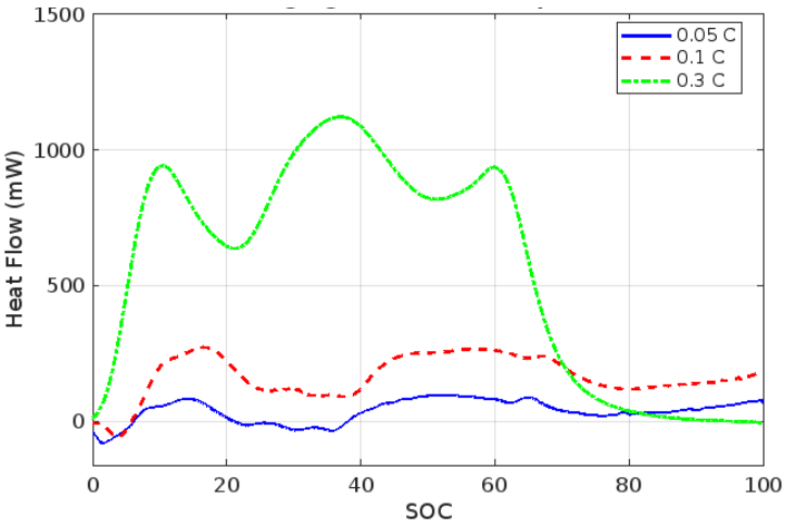

Figure 4.7: Heat flow during charging at different C-rates.

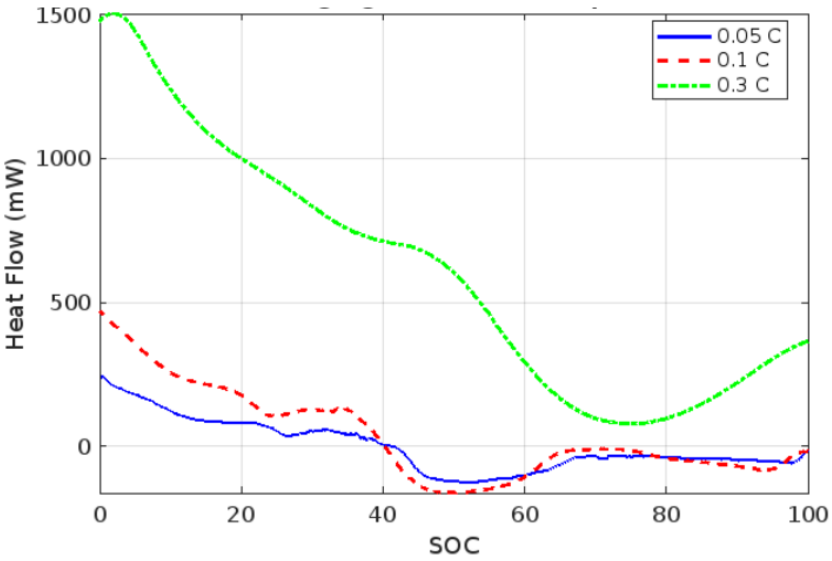

Figure 4.8: Heat flow during discharging at different C-rates.

4.4 Entropic measurement using calorimeter

The calorimetric measurements were carried out with the help of the set up as outlined in Section 3.2 at two temperatures (15°C and 25°C) and across three cycling rates (C/3, C/10, and C/20). With the reversible heat values calculated during charge and discharge cycle and average reversible heat was calculated for example as shown in figure 4.9 for 0.1 C, entropic coefficient was calculated (2.5) for that particular C-rate and temperature. The focus here is on how the entropic coefficient changes with state of charge (SOC) and how sensitive it is to temperature and cycling conditions.

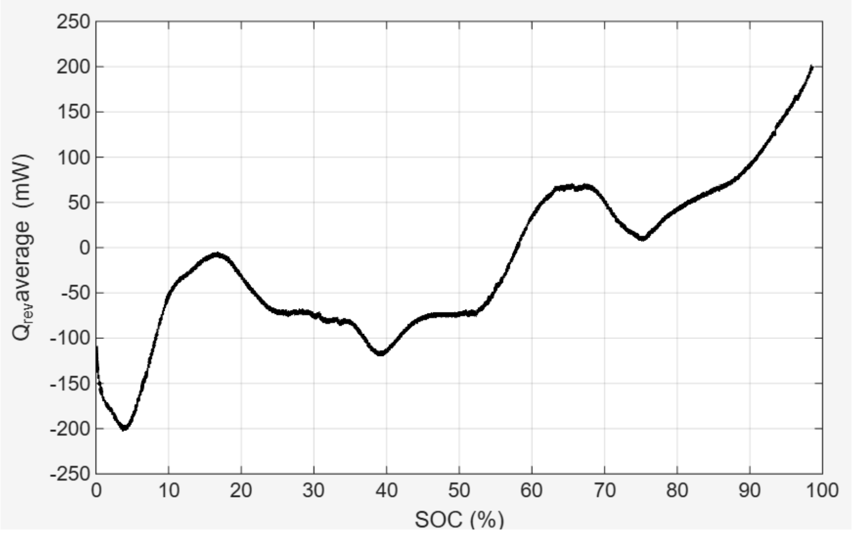

Figure 4.9: Average reversible heat flow during 0.1 C charge and discharge cycle at 25 deg C

At C/10, the entropic coefficient profiles recorded at 15°C and 25°C showed broadly similar shapes across the SOC window, but clear differences in magnitude were evident. At 25°C, the entropy change was more pronounced, while at 15°C the values were consistently lower, especially in two regions: early lithiation (10–20% SOC) and the high SOC range above 95%.

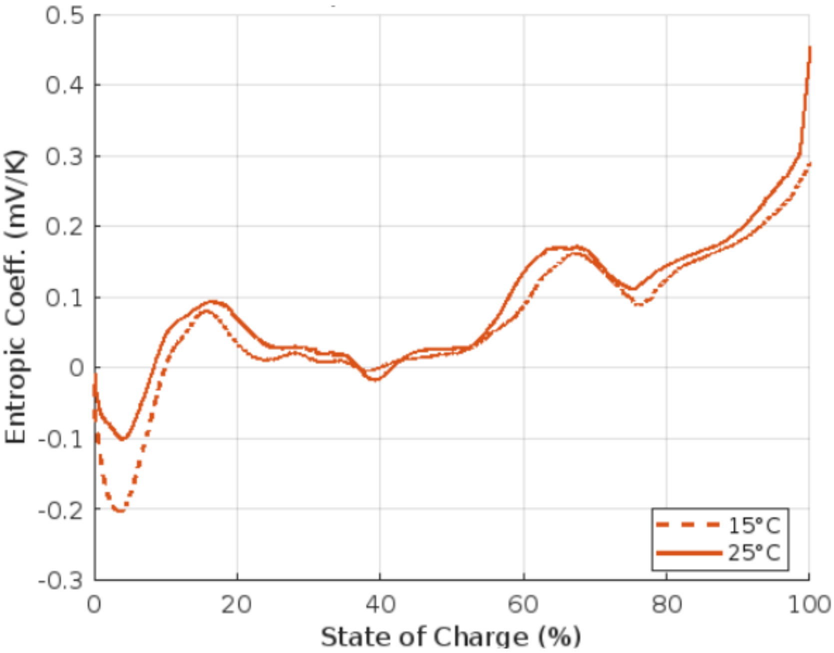

Figure 4.10: Entropic coefficient profile with C/10 cycling at 15 and 25 deg C

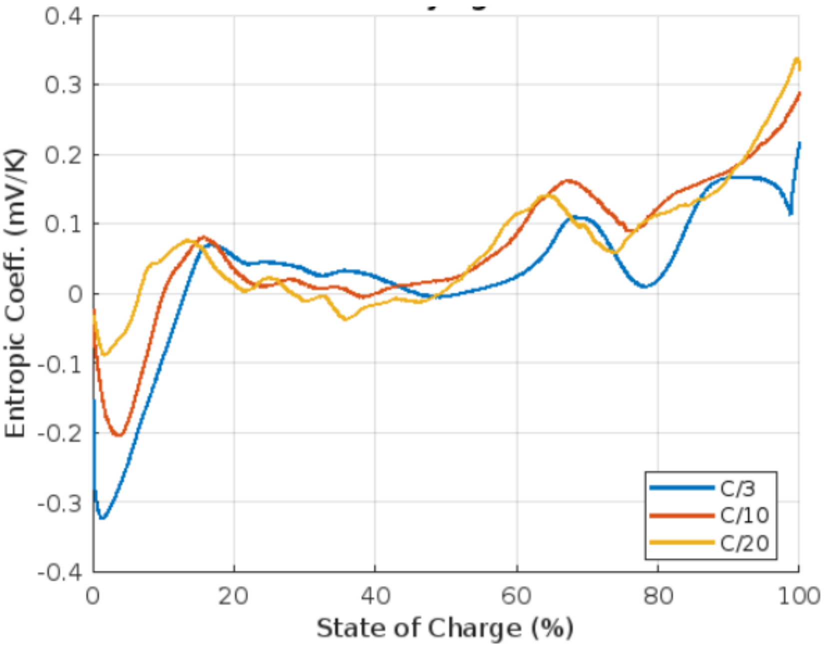

Figure 4.11: Entropic coefficient profile at 15 deg

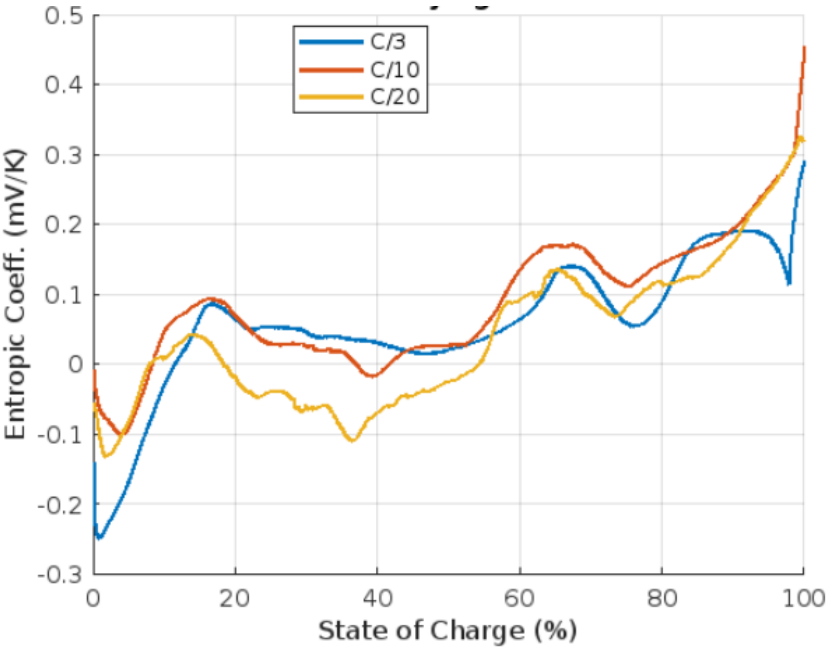

Figure 4.12: Entropic coefficient profile at 25 deg

When comparing cycling rates at constant temperature, further distinctions became clear. At 25°C, the lowest rate (C/20) captures the smallest fluctuation in peaks of entropic coefficient value throughout SOC range. This indicates that slower cycling allows the system to remain closer to equilibrium by avoiding the effect of thermal lags, giving a more well-defined entropy signal. As the rate increased to C/10 and then C/3, the overall magnitude decreased, and the profiles became much smooth, due to insufficient time to measure the heat signals. At C/3, the signal was strongly dampened, pointing to limitations in how quickly the system can equilibrate. A similar picture was observed at 15°C, having simiar suppression, highlighting that the effect of high cycling rate which severely restricts the accurate reversible heat response.

Another noteworthy observation is the reproducibility across repeated runs. For both temperatures, the profiles at C/10 were highly consistent between cycles, with only small variations in peak values. At C/3, the scatter was more evident.

Taken together, the calorimetry results highlight a robust finding: faster cycling rates diminish both the magnitude and clarity of the entropy profiles. These results confirm that the entropic response is highly sensitive to both kinetic limitations and thermal conditions, and they provide a direct experimental picture of how cycling environment influences reversible heat generation in the cell.

4.5 Entropic measurement using potentiometer

As mentioned in chapter 3, potentiometric measurements were performed using MACCOR 4000 (section 3.2), at three temperatures (10°C, 25°C, and 40°C) such as shown in figure 4.13 across the SOC 100%. The aim was to evaluate how the E_{OCV} changes with the cell temperature across entire SOC range and to derive the entropic coefficient ($\partial E_{\text{OCV}}/\partial T_{\text{cell}}$).

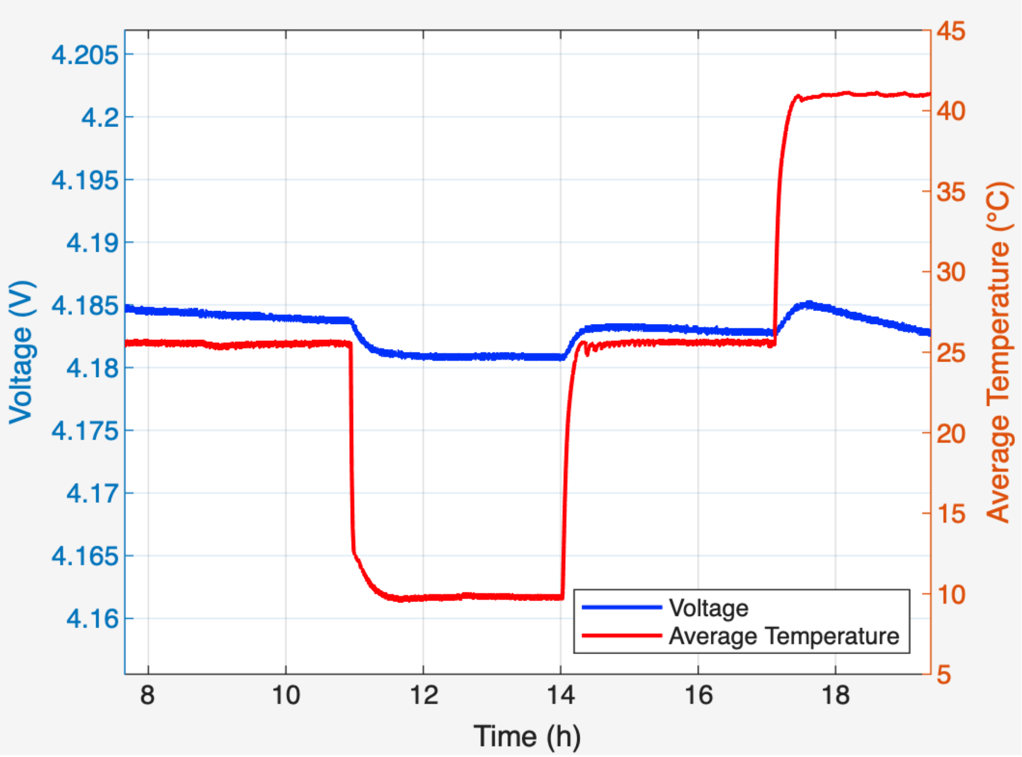

Figure 4.13: Change in volatge due to changing cell temperature.

Figures 4.15 and 4.16 show the OCV as a function of temperature for Cell 1 during charging and discharging and figure 4.14 shows one example for calculating $(\partial E_{\text{OCV}}/\partial T_{\text{cell}})$ at SOC equals to 80%.

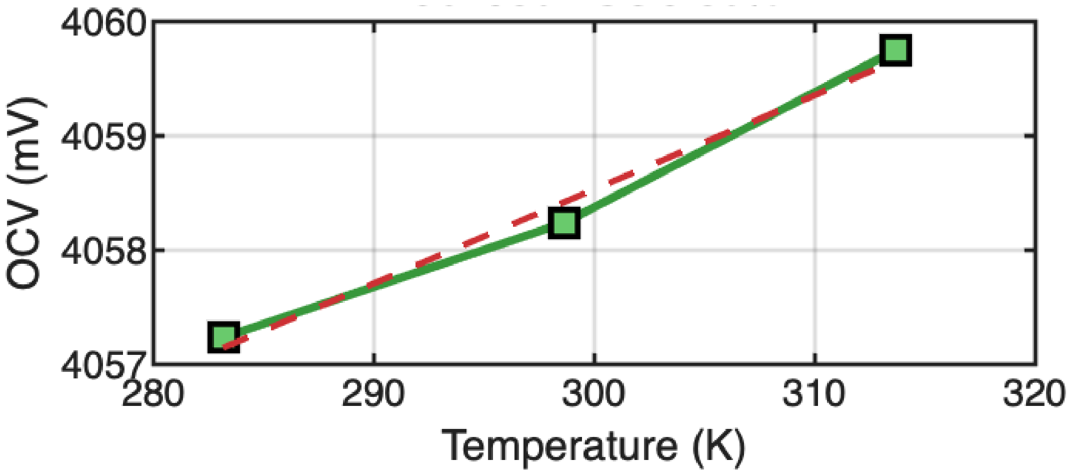

Figure 4.14: Calculating the slope at SOC 80 during charge cycle.

The linearity across the different SOC points was excellent, with most regression fits reaching R^2 values above 0.9. This demonstrates that the OCV–temperature relationship is consistent and reliable, which is essential for extracting entropic coefficient values.

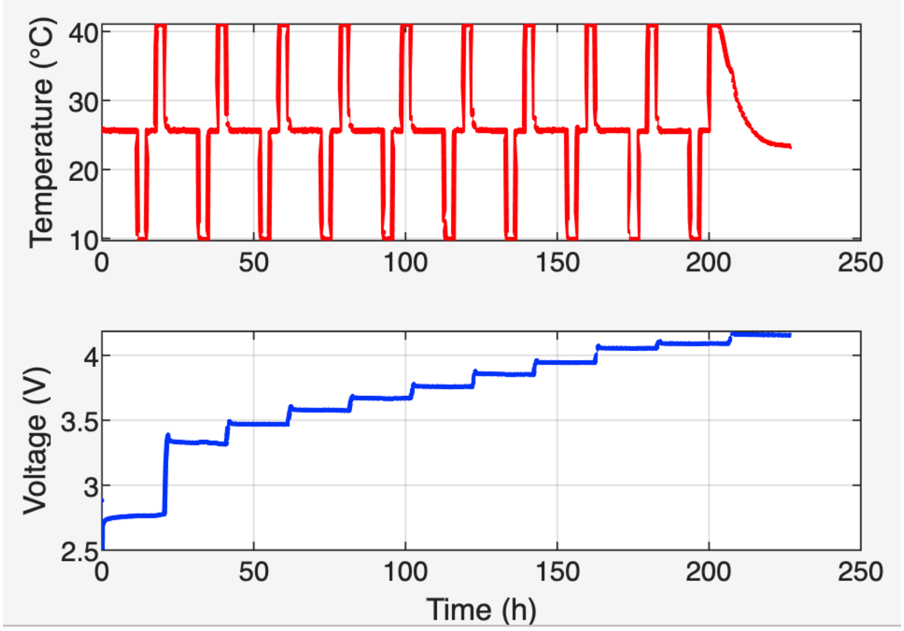

Figure 4.15: Open-circuit voltage as a function of temperature at different SOC levels for Cell 1 during charging.

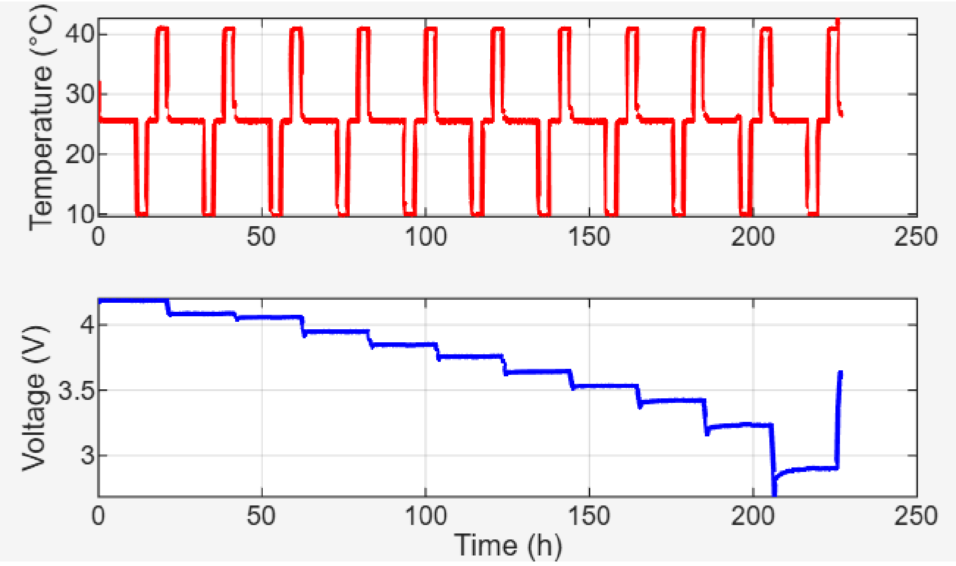

Figure 4.16: Open-circuit voltage as a function of temperature at different SOC levels for Cell 1 during discharging.

A summary of slopes and regression quality is provided in table 4.3. Most SOC points gave strong fits (e.g., $R^2 > 0.98$ at 20%, 50%, 70%, and 90%). However, the extreme points (0% and 100% SOC) showed poor linearity, with R^2 values below 0.7. This suggests incomplete equilibration or slow relaxation at those states, which likely prevented the OCV from fully stabilizing.

Table 4.3: Summary of entropic coefficients and linear fit quality (R^2) for Cells 1 and 2 during discharging.

SOC (%)	Cell 1		Cell 2		
	Slope (mV/K)	R^2	Slope (mV/K)	R^2	Fit Quality
0	0.170	0.770	-0.060	0.699	Poor
10	-0.420	0.944	-0.190	0.995	Good–Excellent
20	-0.034	0.993	-0.128	0.943	Excellent–Good
30	-0.093	0.911	-0.036	0.957	Good–Excellent
40	0.110	0.940	0.052	0.988	Good–Excellent
50	0.093	0.988	0.210	0.992	Excellent
60	0.037	0.503	0.221	0.730	Poor
70	0.051	0.991	0.084	0.978	Excellent
80	0.042	0.973	0.052	0.990	Excellent
90	0.099	0.999	0.0125	0.993	Excellent
100	-	-	0.0119	0.752	Poor

The resulting entropic coefficient profiles are shown in Figures 4.17 and 4.18 for both Cell 1 and Cell 2. The curves clearly reveal alternating positive and negative regions across SOC. At low SOC (10–30%), both cells show negative coefficients, indicating entropy decreases in this range. In the mid-SOC region (40–90%), the coefficients turn positive, with values around 0.04–0.12 mV/K. At high SOC, the coefficients remain positive, reflecting increased configurational entropy during delithiation. These trends were consistent for both cells.

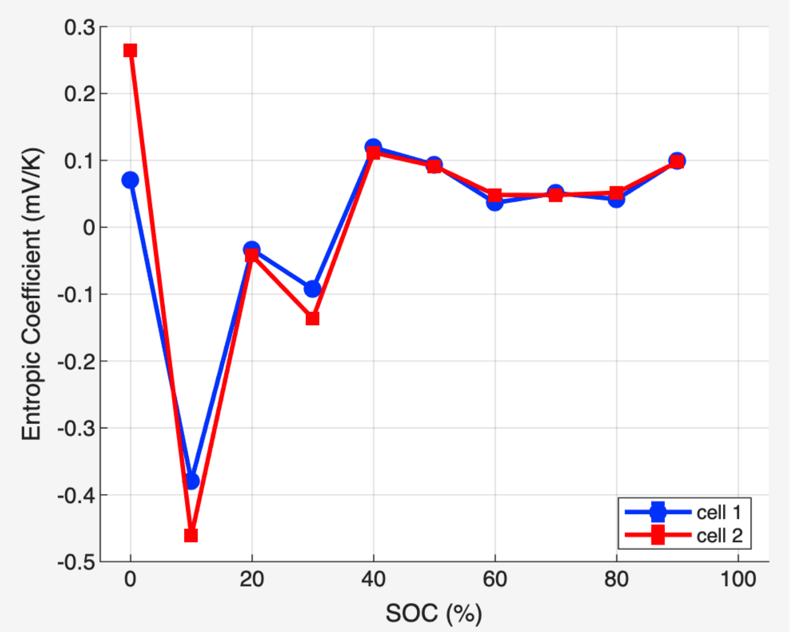

Figure 4.17: Entropic coefficient as a function of SOC for Cells 1 and 2 during charging.

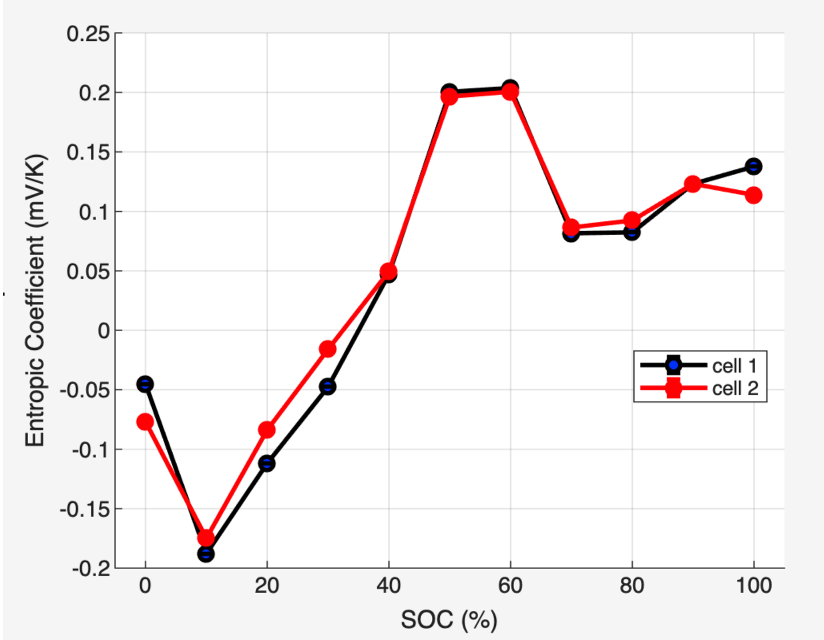

Figure 4.18: Entropic coefficient as a function of SOC for Cells 1 and 2 during discharging.

Overall, the potentiometric measurements confirm that the entropic coefficient varies strongly with SOC, with reproducible patterns of negative values at low SOC and positive values at higher SOC. The comparison of Cells 1 and 2 shows excellent agreement, strengthening confidence in the method and highlighting the robustness of the data.

4.6 Comparison of Calorimetric and Potentiometric Methods

Both calorimetric and potentiometric methods produced entropic coefficient profiles with similar overall shapes, but their reliability varied depending on experimental conditions. To quantify this, the calorimetric data were filtered using root mean square error (RMSE) analysis at two test temperatures, 15°C and 25°C as mentioned in section 3.3. These RMSE plots (figures 4.19 and 4.20) help to identify SOC regions where calorimetric measurements can be trusted, and where they are affected by experimental error. Potentiometric results are used as a baseline for comparison (3.2, 3.3 and 3.4).

4.6.1 RMSE at 25°C

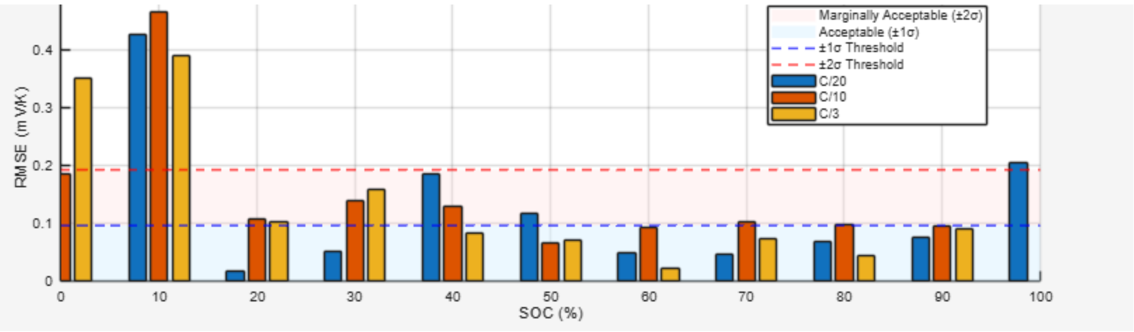

Figure 4.19: Charging

Figure 4.19 shows the RMSE of calorimetric entropy values across the SOC range at 25°C. Three trends are evident:

- **0–30% SOC:** High RMSE values indicate poor reliability. The calorimetric signal in this region was noisy and inconsistent, in contrast to the clear negative entropy captured by potentiometry.
- **30–80% SOC:** Most data points fall within the ±1σ acceptance threshold, especially at lower C-rates (C/20, C/10). This region shows the best overlap with potentiometric results, where mid-SOC entropy values are stable and reproducible.
- **90–100% SOC:** RMSE values drop sharply, and profiles from multiple cycles agree closely. Both methods consistently report strong positive entropy in this region.

4.6.2 RMSE at 15°C

At 15°C, the RMSE profile (figure 4.20) shows much larger error across most of the SOC range. The only region with consistently acceptable RMSE was at mid SOC (20–90%). Low SOC (0–2%) and high SOC (90–100%) were dominated by scatter, producing unreliable entropy values.

It is important to note that these deviations should not be interpreted as true temperature effects on entropy. Instead, they likely arise from experimental setup:

- At lower temperatures, heat leakage through imperfect insulation increases the background noise of the calorimeter, artificially inflating RMSE.
- At higher temperatures (e.g., 40°C,), the limited relaxation time after current steps may not have been sufficient for the cell voltage to reach equilibrium, leading to poor OCV fits.

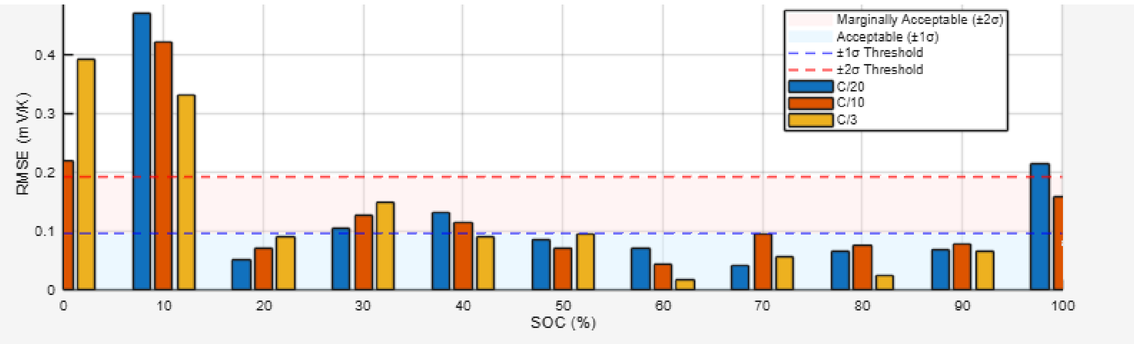

Figure 4.20: Charging

In contrast, potentiometric measurements remained stable, capturing smooth negative entropy at low SOC and positive entropy at high SOC, confirming that the underlying thermodynamic profile is unaffected by temperature within this range. The scatter in calorimetry therefore reflects measurement limitations, not a true physical dependency.

4.6.3 Overall Assessment

The RMSE analysis shows that calorimetry is sensitive to experimental conditions. Given the rapid changes in the entropic coefficient at extreme SOCs, any small inaccuracies or noise in the temperature, voltage, or current measurements can be significantly amplified when calculating the derivative $\left(\frac{\partial U}{\partial T}\right)$. This makes the determination of the entropic coefficient highly sensitive in the critical regions. At extreme SOC levels, as entropic heat is highly sensitive to small temperature changes, phase transitions in electrode materials, and lithiation / de-lithiation under high lattice influence, causing unstable or irregular entropy profiles and unreliable data [34, 35].Research indicates that heat generation profiles can vary significantly across different locations on a battery cell [36]. Rapid and complex heat generation profiles at extreme SOCs hence precise methods should be taken while measuring parameters such as heat flow.

Potentiometry, by contrast, avoids these issues: the long equilibration steps ensure accurate OCV values, producing reliable entropic coefficients across the full SOC window at all temperatures tested. This highlights potentiometry as the more robust approach, with calorimetry offering complementary insight only in carefully controlled SOC regions. Using both together strengthens confidence in the results and clarifies the boundaries of reliability for entropy measurements in lithium-ion cells.

4.7 EECM Parameter Validation

The constructed model was validated through multiple approaches to ensure its performance not only on available data but also under new operating conditions. Validation helps identify potential flaws and ensures that the predicted temperature distribution is robust, reliable, and representative of real-world behavior.

The Equivalent Electrical Circuit Model (EECM), which accounts for the irreversible heat generated by the battery cell, was validated using two distinct load cycles, shown in figures 4.21 and 4.22. These load cycles confirm that the parameters obtained from the GITT tests are correctly implemented within the model. Each load cycle represents a straightforward current–voltage profile, with the corresponding current applied to the EECM as depicted in figures 4.21(a) and 4.22(a). The goal is to reproduce a voltage response that closely matches the experimental load cycle. Any deviations in the simulated voltage are then used to fine-tune and scale the RC parameters, ensuring the EECM accurately represents the cell's electrical and thermal behavior.

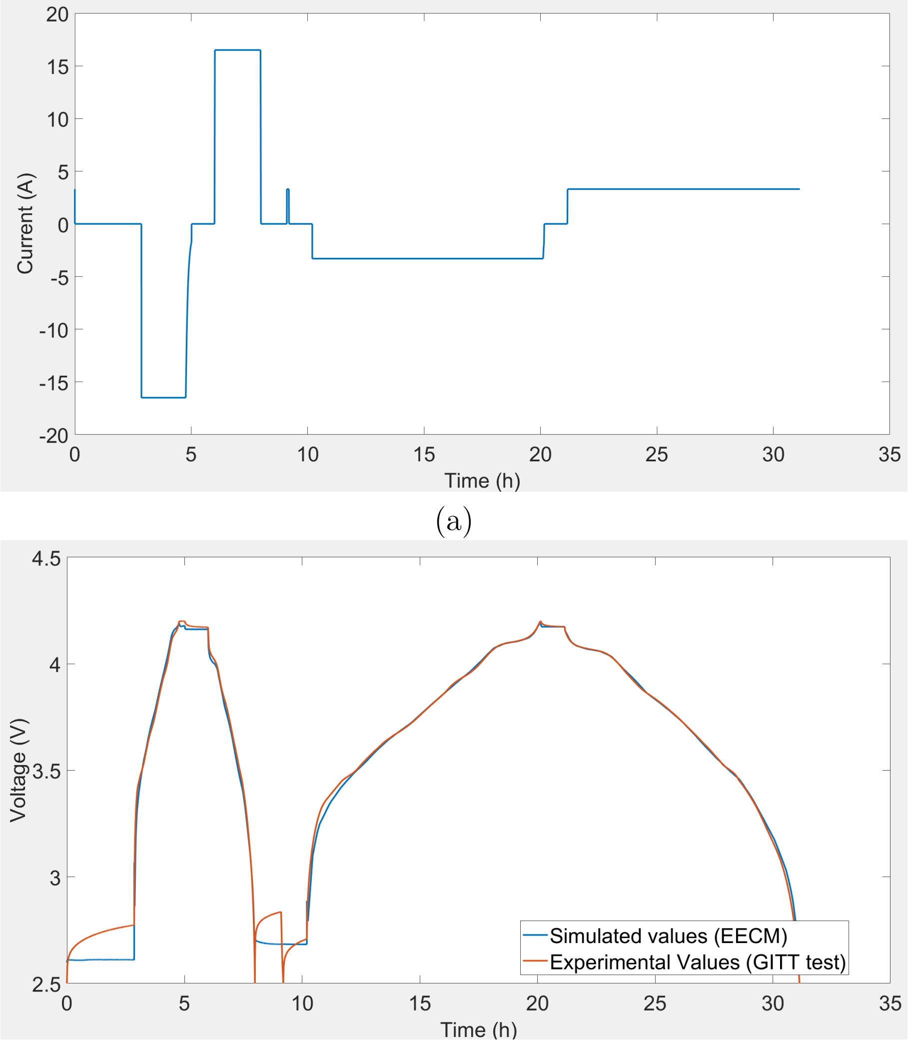

(a)

(b)

Figure 4.21: a) Current applied to the EECM and b) Voltage response from EECM and GITT test.

The discrepancy in values is observed in figure 4.21(b) when the voltage is less than 2.8V. This is because of the inability of the solver to extrapolate the OCV values under 2.8V, since the tests performed to obtain these values are in the range of 2.8 - 4.1 V. Furthermore, it also could be due to solver being unable to converge because of low SOC which results in nonlinear equations approaching singularities. The “singularities” COMSOL warns about in low-SOC regions are usually logarithmic or reciprocal concentration terms (from Nernst equations, Butler–Volmer kinetics, or transport relations) that diverge as species concentrations approach zero or maximum limits, making the Jacobian nearly singular and causing solver divergence. So, a more relaxed and inside the defined voltage range is simulated to validate the model again.

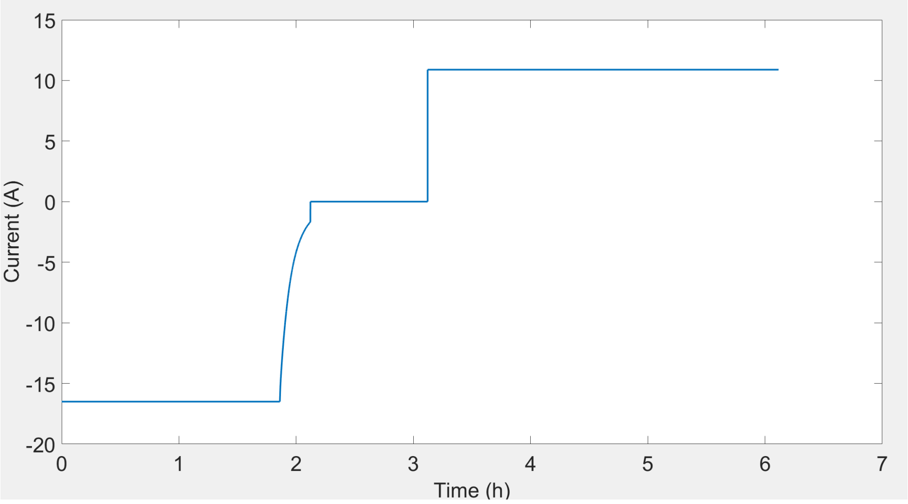

(a)

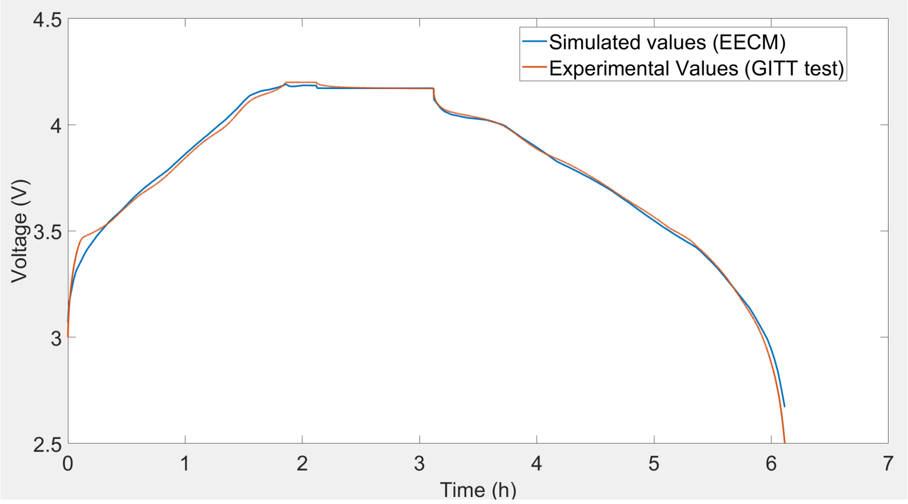

(b)

Figure 4.22: a) Current applied to ECM and experiment and b) corresponding voltage responses.

The cycle shown in figure 4.22 demonstrates that the ECM parameters obtained from the GITT testing are highly reliable (since the voltage obtained from ECM is almost superimposed on the voltage obtained experimentally). Building on this, the next step is to validate the heat generation predicted by the ECM model using (2.4). To do this, we compare the amount of heat calculated by the model with the heat actually measured in the experiments as shown in figure 4.25.

The entropic coefficient values have been identified for both the charging and discharging processes in figure 4.17 and figure 4.18 respectively. Using these values, we can estimate the total heat generated by the cell and then directly compare it with the experimental data to evaluate how well the model reflects real behavior.

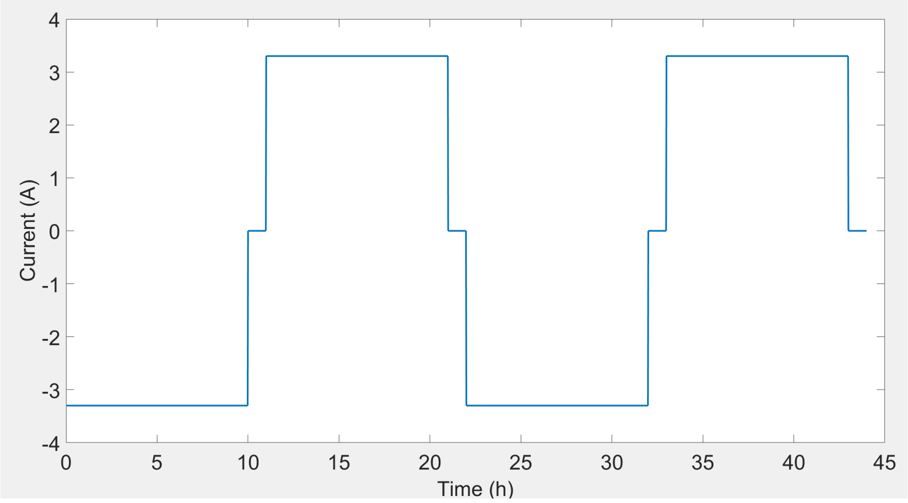

(a)

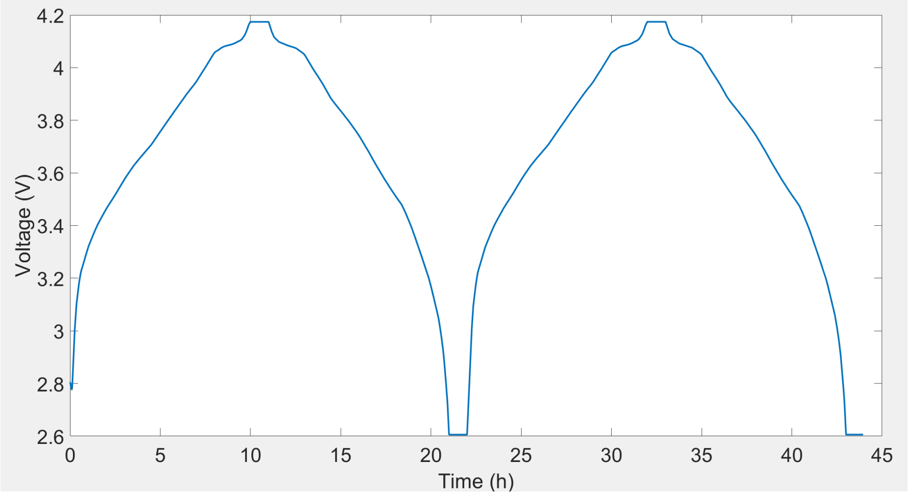

(b)

Figure 4.23: a) EECM subjected to 0.1C current and b) Corresponding EECM voltage response.

At a 0.1 C-rate, the applied current is calculated using 0.1 × capacity. The capacity denotes the nominal capactiy of the cell. Under these conditions, a full charge or discharge cycle lasts approximately 36,000 seconds (10 hours), as illustrated in figure 4.23(a). To ensure stability between charging and discharging phases, the cell is allowed a rest period of 3,600 seconds before transitioning from one phase to the other.

At lower C-rates, the total heat generated is primarily dominated by reversible heat, as observed in figure 4.24. The main contributor to this reversible heat is the entropic coefficient, which was determined experimentally. Some discrepancies are noted, as illustrated in figure 4.25, due to the model interpolating between discrete entropic coefficient values measured during charging and discharging.

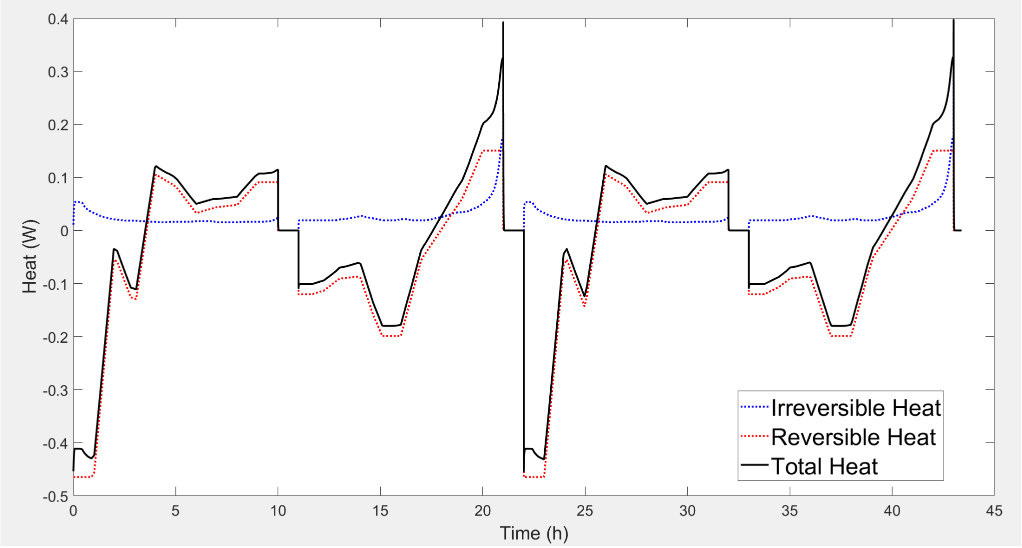

Figure 4.24: Heat generated by the cell during 0.1C Cycling

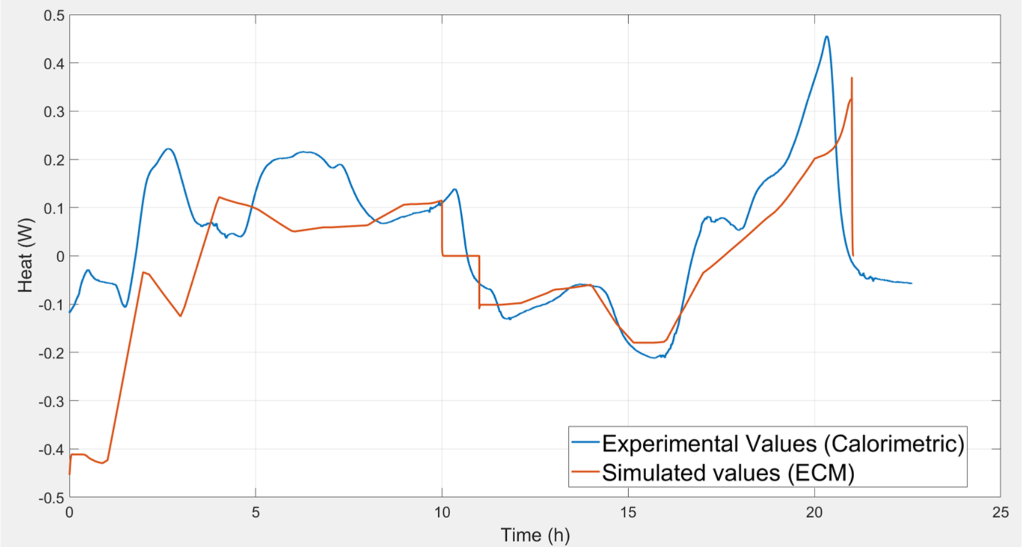

Figure 4.25: Comparison of heat generation at 0.1C Rate

In reality, the entropic response of the cell changes smoothly and continuously, rather than in discrete steps. Because reversible heat generation is highly sensitive to variations in the entropic coefficient, even small differences can result in significant fluctuations in the predicted heat.

Another factor contributing to these discrepancies is the location of heat measurement. Experimentally, heat is recorded at the surface of the cell, whereas in the simulation it is calculated at the center. This introduces a lag governed by the thermal time constant, which represents the rate at which heat generated inside the jelly roll propagates to the cell surface. Due to time constraints, the thermal time constant could not be measured experimentally, which further explains the observed deviations between the model predictions and experimental results.

4.8 Battery Electrothermal Model

First, the heat generated at each C-rate was calculated using the ECM parameters in combination with the experimentally determined entropic coefficient within the ECM model. Since the GITT experiments were performed at 0.1C, 0.5C, and 1C, the software interpolated the RC parameter values for intermediate C-rates and extrapolated them for higher C-rates. However, extrapolation beyond 2C proved unreliable. Consequently, the total heat generation was evaluated at 0.1C, 0.3C, 0.5C, 1C, 1.5C, and 2C.

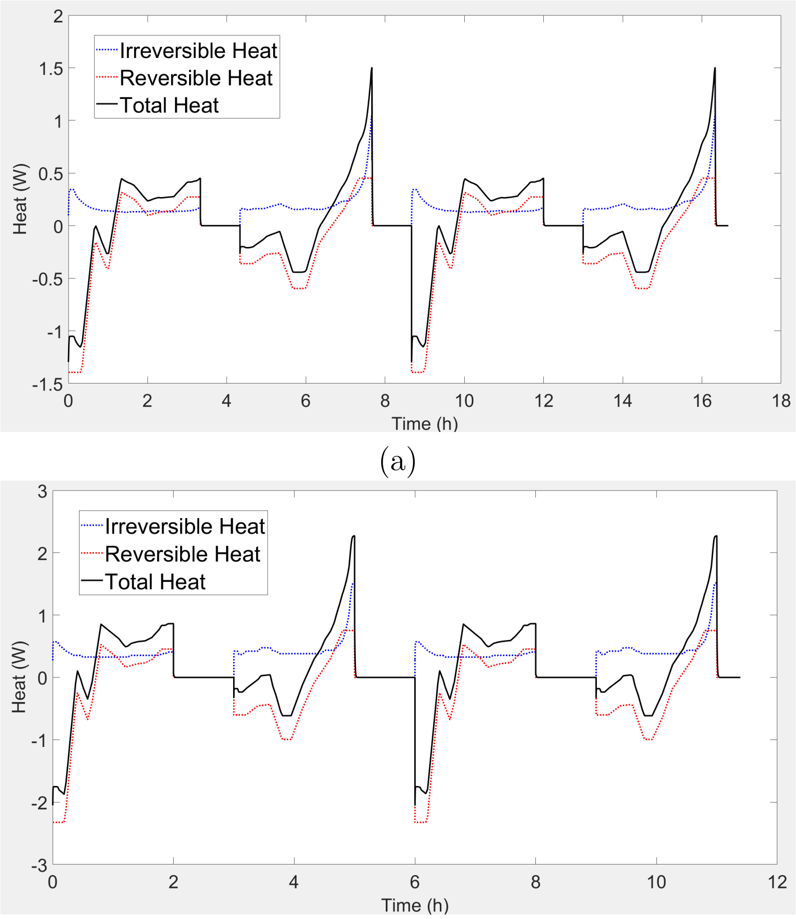

(a)

(b)

Figure 4.26: Overall heat generation at a) 0.3C and b) 0.5C rates.

Figures 4.26 and 4.27 show that the heat generated increases with rising C-rates due to the corresponding increase in current. The reversible heat is associated with entropic changes in the battery, which depend on the cell chemistry and the state of charge, as described in (2.3). At lower C-rates, the current is relatively small, resulting in minimal irreversible heat, so the reversible heat dominates the total heat generated.

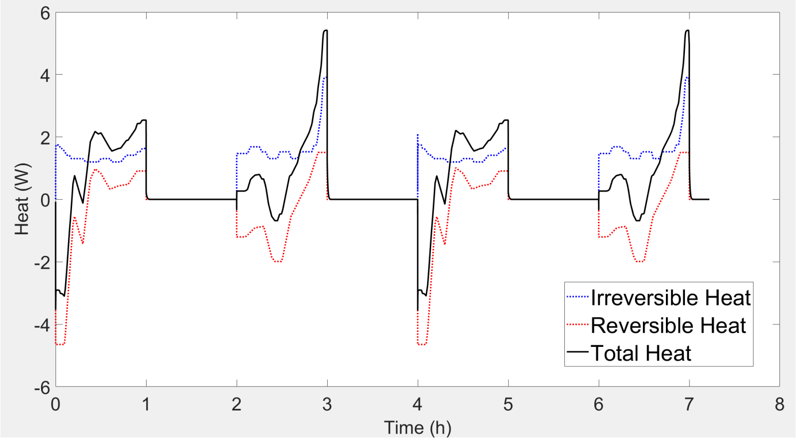

(a)

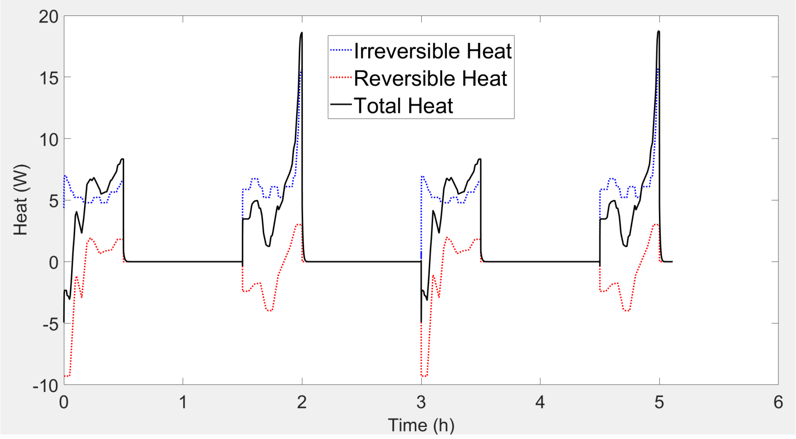

(b)

Figure 4.27: Overall heat generation at a) 1C and c) 2C-rates.

At higher C-rates, as the current increases, the irreversible heat grows rapidly due to its quadratic dependence on current, as described in (2.2). However, the reversible heat does not vanish; it continues to contribute based on the entropic coefficient and the rate of change of the cell's voltage with temperature. In certain SOC ranges where the entropic coefficient is large (either positive or negative), the reversible heat can still be comparable to the irreversible heat, even at high C-rates.

In essence, while irreversible heat dominates at high currents, the reversible component is always present because it depends on the intrinsic thermodynamic properties of the cell rather than the current magnitude. It can either add to or subtract from the total heat generation, depending on the sign of the entropic coefficient.

The total heat generated was then used to compute the temperature distribution within the cell using a 3D thermal model. Figure 4.28 illustrates the resulting temperature distributions at different C-rates, simulated under the conditions described in Section 3.6.1.3.

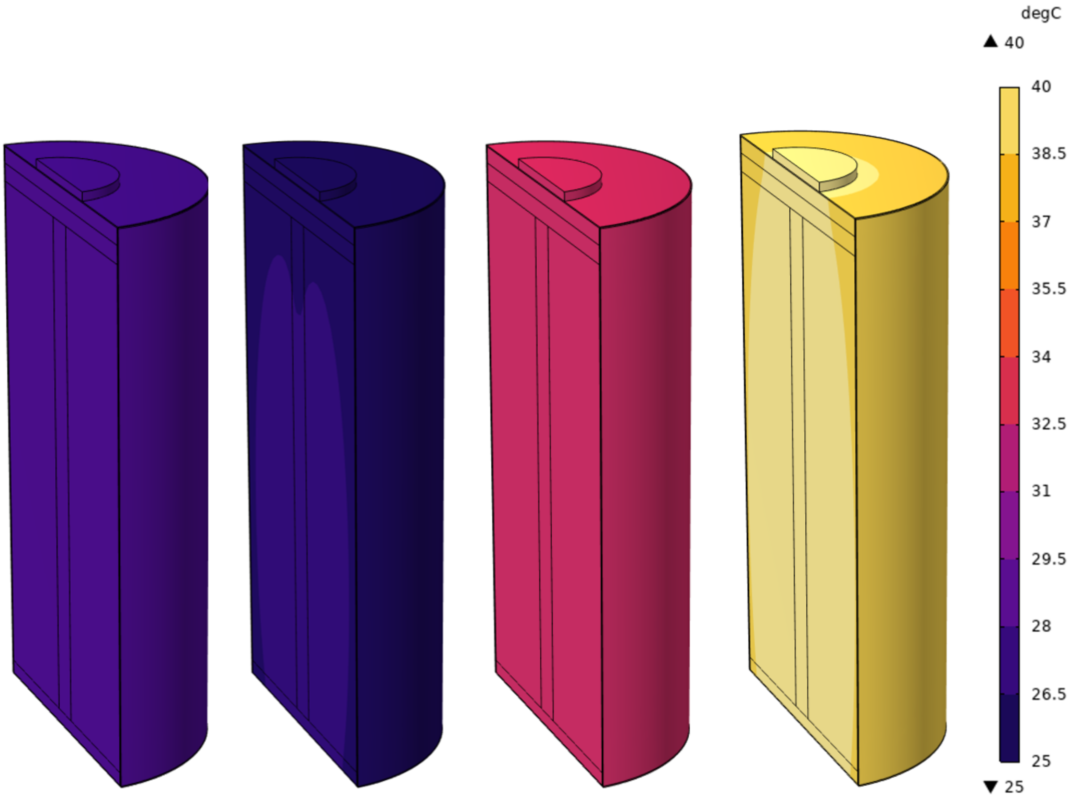

Figure 4.28: Temperature distribution for 0.1, 0.3, 0.5 and 1 C-rates.

The time at which the cell reaches its maximum temperature varies depending on the C-rate used in the simulation. These times are summarized in table 4.4. From the table, it is evident that the cell attains its highest temperature when it is nearly fully discharged. This suggests that thermal stress peaks toward the end of the discharge cycle, likely due to increased internal resistance and elevated heat generation, as observed in figure 4.27 when the cell approaches its lower state-of-charge limit.

Table 4.4: Maximum cell temperature at a given time for each applied C-rate.

C-rate	Time	Maximum Temperature	SOC
0.1	21 h	27°C	1.29%
0.3	7.66 h	29°C	1.29%
0.5	5 h	33°C	1.29%
1.0	3 h	40°C	1.29%

Figure 4.28 does not clearly illustrate the temperature gradient within the cell. Therefore, a more detailed temperature distribution at 1C-rate is presented in Figure 4.29.

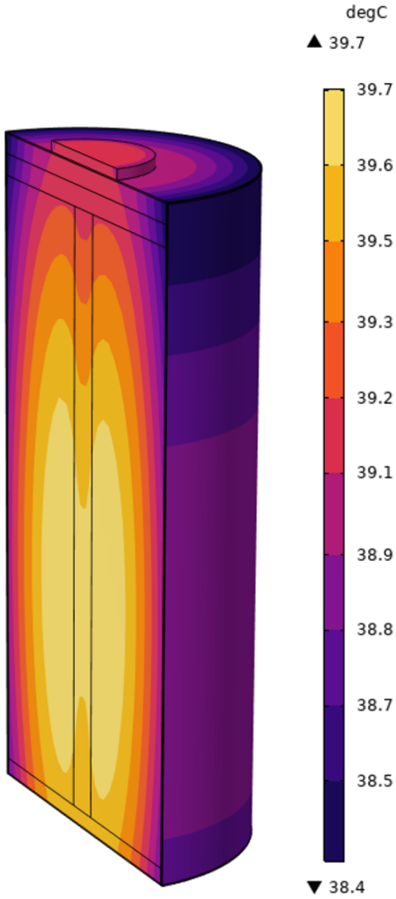

Figure 4.29: Temperature distribution for 1C-rate at 3h.

The highest temperature in the cell occurs at the center of the jelly roll, since this is where heat is defined in the EECM model as you can see in figure 3.8. As the C-rate increases, the overall heat generation rises, which leads to a higher temperature at the center. When examining temperature distribution, we see in figure 4.29 that the gradient along the axial direction (top to bottom of the cell) is much smaller than the gradient in the radial direction (from the center outwards). This happens because heat flows more easily along the axis, since the axial thermal conductivity is nearly 14 times higher than the radial conductivity. So the temperature differences are quickly evened out along the length of the cell.

Even though the axial thermal conductivity is the same, the temperatures at the top and bottom of the cell are not identical. This is due to insulating components near the top, such as gaskets and sealing rings around the cell terminals, thus lowering the effective thermal conductivity in that path which reduces heat flow in that direction as described in table 3.2. At the bottom, heat can flow more freely through the negative current collectors, which connect the case and the jelly roll, resulting in slightly lower temperatures. In short, the temperature distribution is influenced both by the geometry and thermal properties of the cell and by local variations in insulation, which create small but noticeable differences between the top, center, and bottom of the battery.

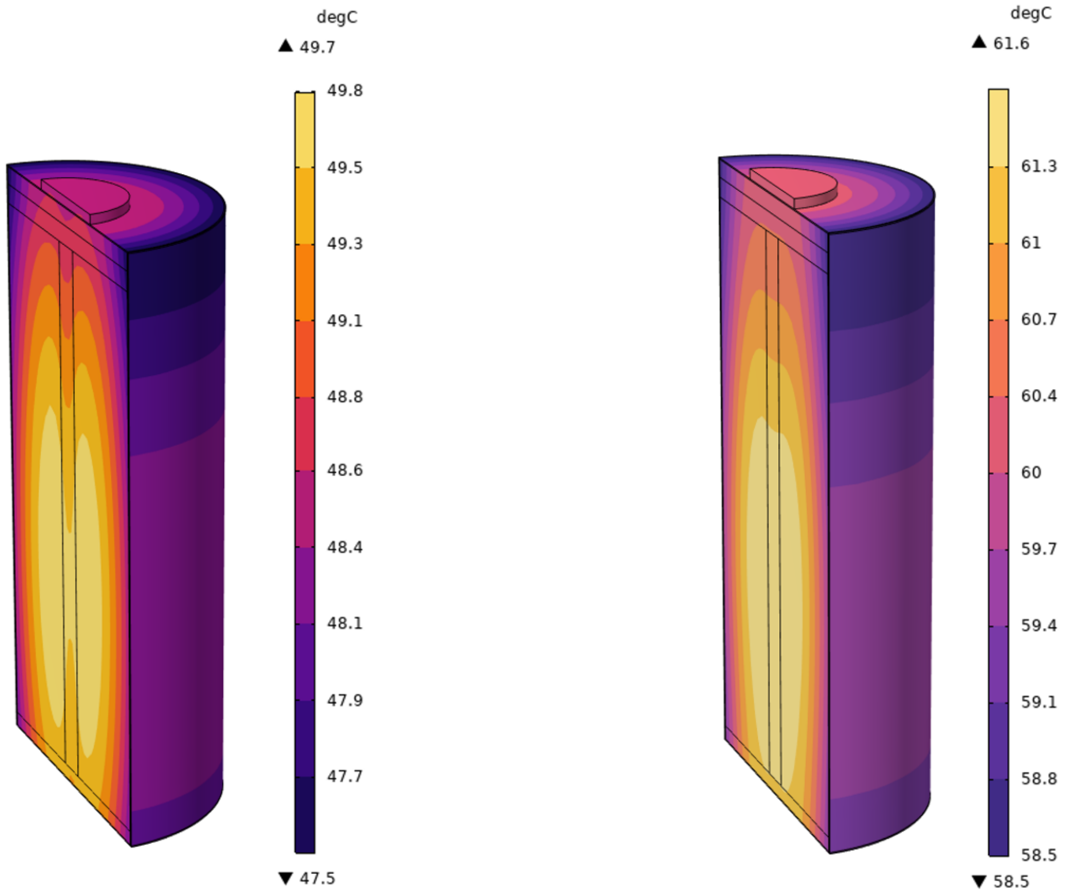

(a)

(b)

Figure 4.30: Temperature distribution for a)1.5C at 2.25h and b) 2C at 2h.

When the cell was exposed to natural convection, active cooling was not required for C-rates up to 1C. In this range, the maximum cell temperature reached only 39.8°C, as shown in figure 4.29, which is safely within the recommended operating range for the battery (25–45°C). However, at higher C-rates, specifically 1.5C and 2C, the temperature exceeded 45°C, as illustrated in figure 4.30. At these elevated rates, the heat generated exceeds what can be dissipated through natural convection alone, necessitating active cooling strategies to maintain safe and efficient operation.

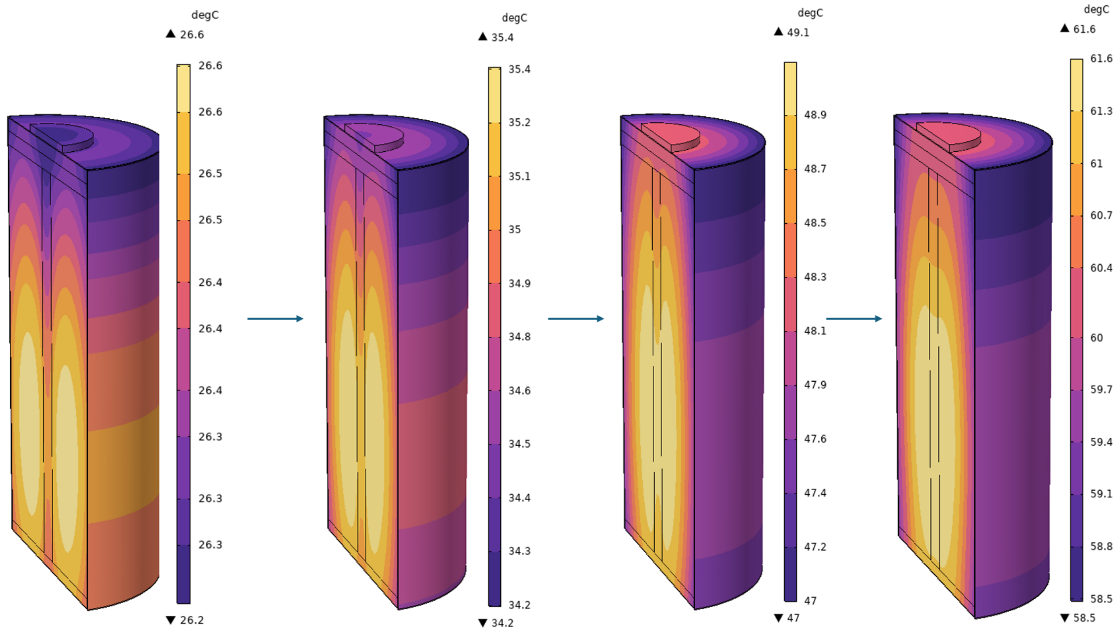

Figure 4.31: Heat flow inside the cell for a charge-discharge cycle at 2C-rate.

Table 4.5: Temperature Gradient of large cylindrical Lithium-ion cells

Cell Geometry	Temperature Gradient		Reference
	Radial	Axial	
4680	1-3°C	4°C	[37]
4680	1-4°C	3-5°C	[38]

The table 4.5 indicates that large cylindrical lithium-ion cells generally exhibit only small temperature gradients across the cell. This aligns well with the results from the model developed in this work, which also shows minimal variation in temperature (around 3°C). The relatively uniform temperature distribution can be attributed to the high axial thermal conductivity of the jelly roll structure, which allows heat to spread efficiently along the length of the cell. As a result, significant hot spots do not form within the cell and overall temperature differences remain small.

4.9 Cooling Strategy Analysis

Since the cell's temperature rises above 45°C at higher C-rates, cooling becomes necessary to keep it within the optimal operating range. Proper cooling helps prevent accelerated aging and extends the overall lifespan of the battery. As mentioned earlier, the cell has a vent located at the bottom. As a result, the cell was only simulated for single-sided, double-sided, and top cooling with the conditions specified in Section 3.7.1.

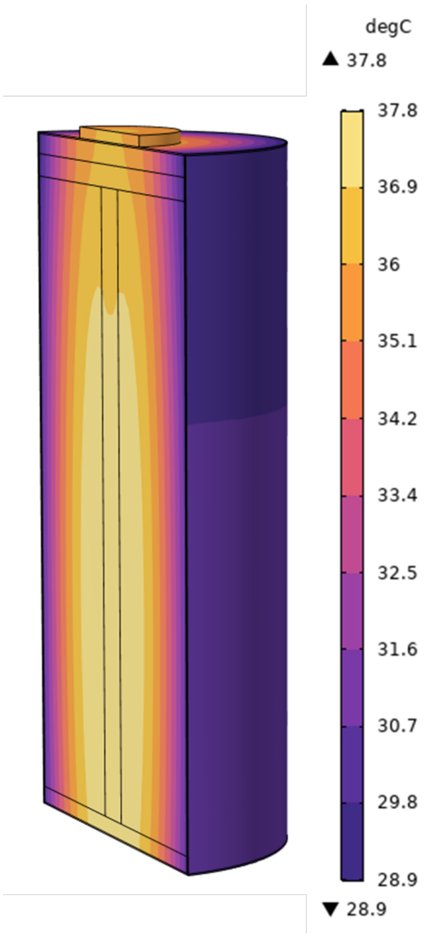

Figure 4.32: Cell temperature distribution at 1.5C at 2.33h with double-sided cooling.

Double-sided cooling was implemented for 1.5C-rate, and the results are displayed in figure 4.32. As observed, the temperature gradient across the cell is 5.4°C. The temperature distribution along the axial direction is nearly uniform, thanks to the cell's high axial thermal conductivity, which allows heat to spread efficiently from top to bottom. In this simulation, the cell is exposed to double-sided cooling, while the remaining outer surfaces interact with the environment through natural convection. Double-sided cooling is expected to minimize temperature gradients and reduce the overall heat transfer resistance, and the results confirm this behavior.

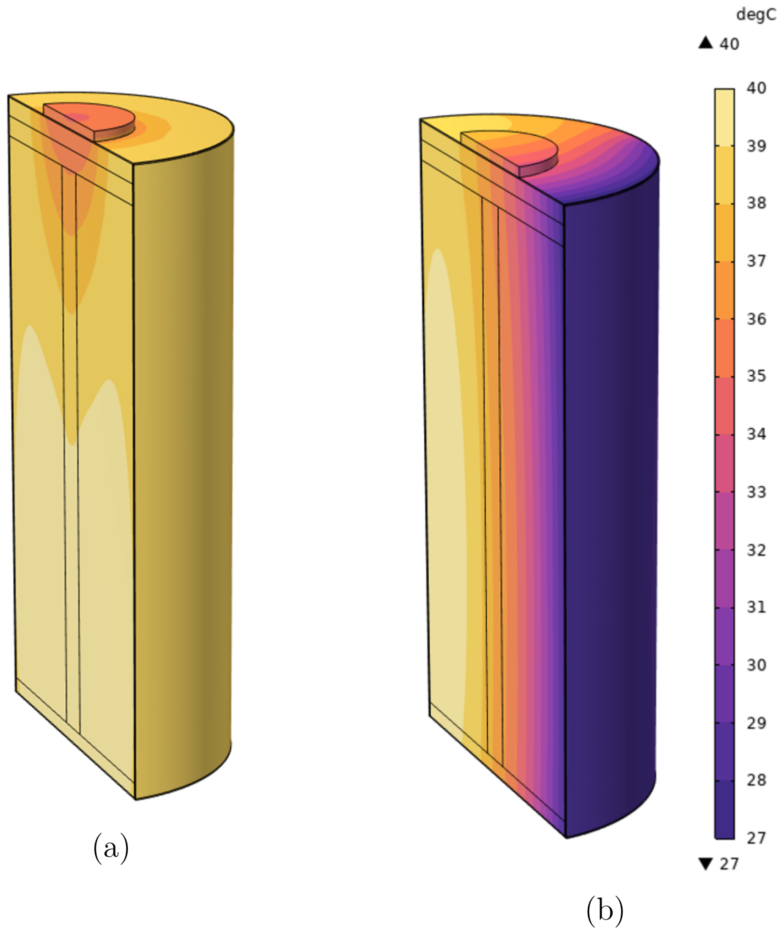

Figure 4.33: Cell temperature at 1.5C-rate when subjected to a) Top cooling and b) Single-sided cooling at 2.333h.

In addition to double-sided cooling, simulations were also performed for single-sided and top cooling at a 1.5C-rate as shown in figure 4.33. The results show that single-sided cooling leads to high temperature gradients in the radial direction. This occurs because the cell's radial thermal conductivity is low, so heat cannot efficiently spread from the center to the cooled surface. Consequently, the radial temperature difference is significant, while the axial temperature remains relatively uniform due to the high axial thermal conductivity.

Top cooling, on the other hand, produces substantially lower temperature gradients than both single-sided and double-sided cooling. However, a large amount of heat still needs to be removed because the surface area available for cooling is limited, which increases the heat flux per unit area.

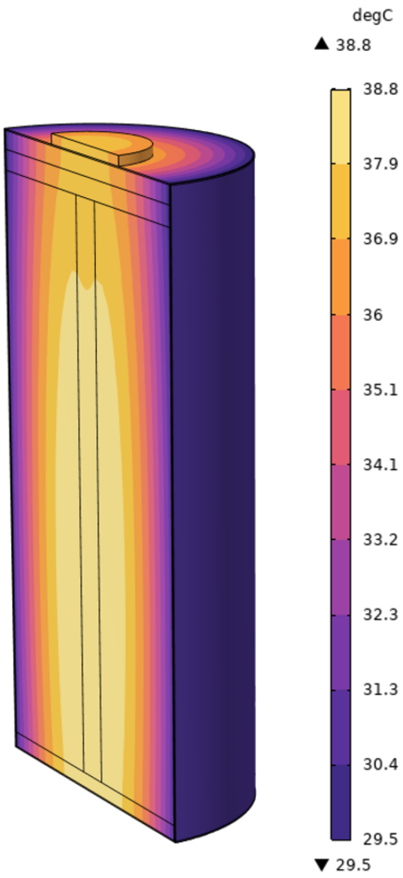

Figure 4.34: Cell temperature distribution at 2C with double-sided cooling at 2h.

Cooling strategies were also applied at a 2C-rate for comparison with the 1.5C-rate case. Double-sided cooling at 2C-rate reduced the maximum temperature by around 20°C, slightly more than at 1.5C-rate, reflecting the higher heat generation at this rate. The temperature gradient across the cell was about 9°C as it can be seen in figure 4.34, which is still relatively low, showing that heat dissipation from both sides remains effective even at higher C-rates. The highest temperatures continued to occur at the center of the jelly roll, while axial temperature differences stayed small due to the high axial thermal conductivity. However, the total amount of heat that needed to be removed was larger than at 1.5C-rate, consistent with the increased heat generation.

Double-sided cooling provides the most uniform temperature distribution, as heat is extracted simultaneously from both sides. This not only lowers the maximum temperature but also reduces the radial gradient more effectively than the other methods. In all three configurations, axial temperature differences remain minimal due to the high thermal conductivity along the length of the cell.

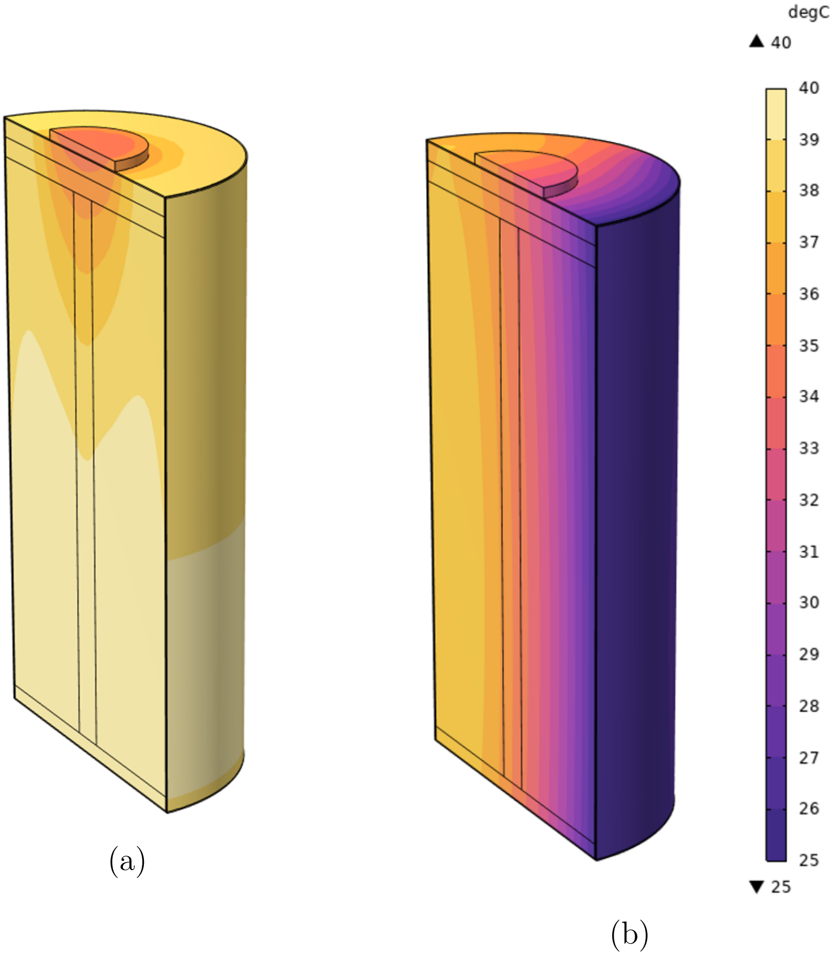

Figure 4.35: Cell temperature at 2C-rate when subjected to a) Top cooling, b) Single-sided cooling at 2h.

Finally the cell was simulated at the module level for orientations of 90° and 60° double-sided cooling using the simulation configuration described in Section 3.7.2.2.

From the simulation results displayed in figure 4.36, the temperature gradient under 90° double-sided cooling is approximately 5°C (30°C-25°C), while for 60° double-sided cooling it is around 6°C (33°C-26.5°C) at 1C-rate. The required heat flux also varies between the two configurations. Because of the cell's low radial thermal conductivity, the temperatures in the jelly roll remain relatively high, and the temperature difference between the center and the surface is noticeable.

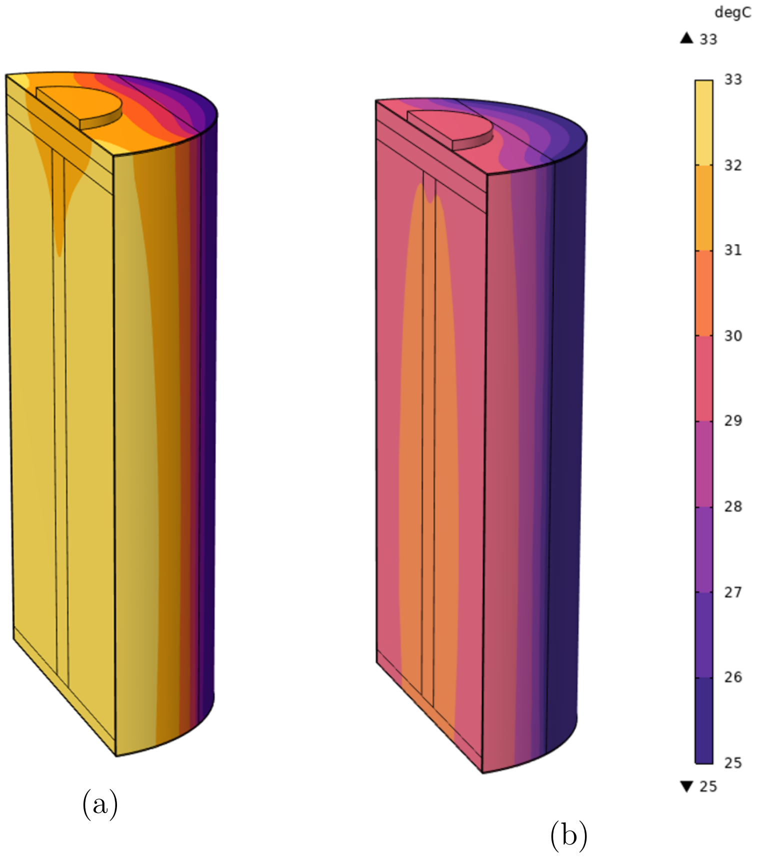

(a)

(b)

Figure 4.36: Cell temperature at 1C-rate when subjected to a) 60° and b) 90° double-sided cooling at 3h.

Although 90° double-sided cooling achieves a lower temperature gradient and requires less heat removal compared to 60° double-sided cooling, it introduces practical challenges. The tighter bends required in the cooling tubes increase flow resistance, which can lead to a pressure drop along the coolant path. As a result, the coolant velocity may decrease in certain regions, reducing the local heat transfer coefficient. In addition, sharp or frequent bends increase the likelihood of uneven flow distribution between different channels, meaning that some areas of the cell may be cooled less effectively than others.

From a mechanical perspective, excessive bending can also complicate the manufacturing and installation of the cooling system. It may increase the risk of tube deformation, kinking, or even leakage over long-term operation, especially under thermal cycling and vibration. Furthermore, the higher pumping power required to overcome the added resistance increases the system's overall energy consumption and reduces efficiency.

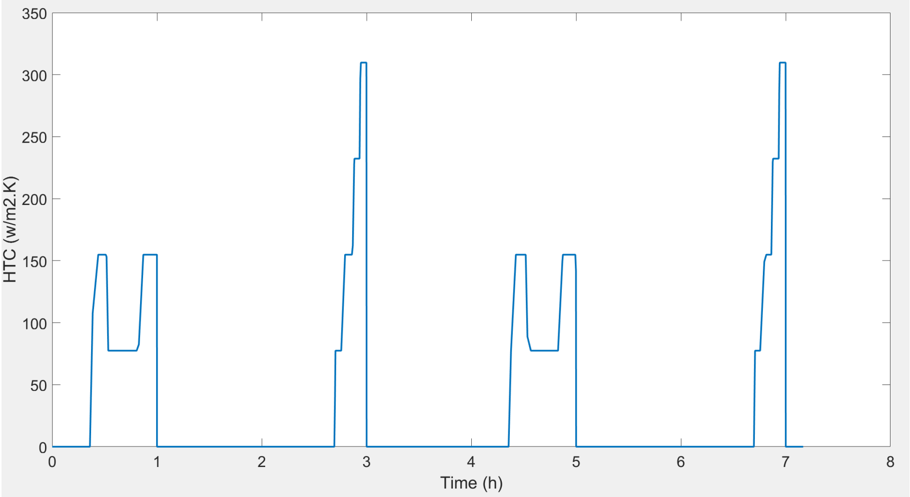

Figure 4.37: Removed heat flux at 1C under 60° double-sided cooling.

Since the heat generated is negative most of the time during charging and sometimes during discharging a varying heat flux is required to be removed so that the temperature doesn't fall below 25°C. The varying heat flux removed from 60° double-sided cooling at 1C-rate is depicted in the figure 4.37. The maximum amount of heat flux needed to be removed to keep the temperature gradient of the cell was around 307 $[\mathrm{W}/(\mathrm{m}^2 \cdot \mathrm{K})]$. Whereas it is around 207 $[\mathrm{W}/(\mathrm{m}^2 \cdot \mathrm{K})]$ for 90° double-sided cooling as shown in figure 4.38.

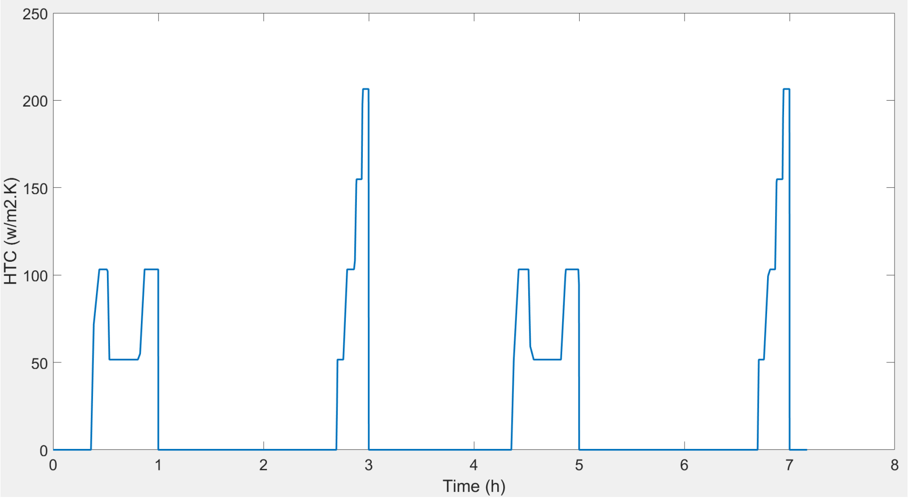

Figure 4.38: Removed heat flux at 1C under 90° double-sided cooling

The amount of heat flux needed to remove from the cell determined mathematically:

$$h_{24.073} = 307\ \mathrm{W/m^2{\cdot}K}, \quad L_1 = 24.073\ \mathrm{mm}, \quad L_2 = 36.11\ \mathrm{mm}$$

Assuming constant total heat removal ($Q = \text{const}$) and $A \propto L$:

$$h_{36.11} = h_{24.073} \cdot \frac{L_1}{L_2} = 307 \cdot \frac{24.073}{36.11} = 204.6\ \mathrm{W/m^2{\cdot}K}$$

4.10 Simulation Results Overview

Table 4.6: Temperature obtained at different areas of the cell in degC

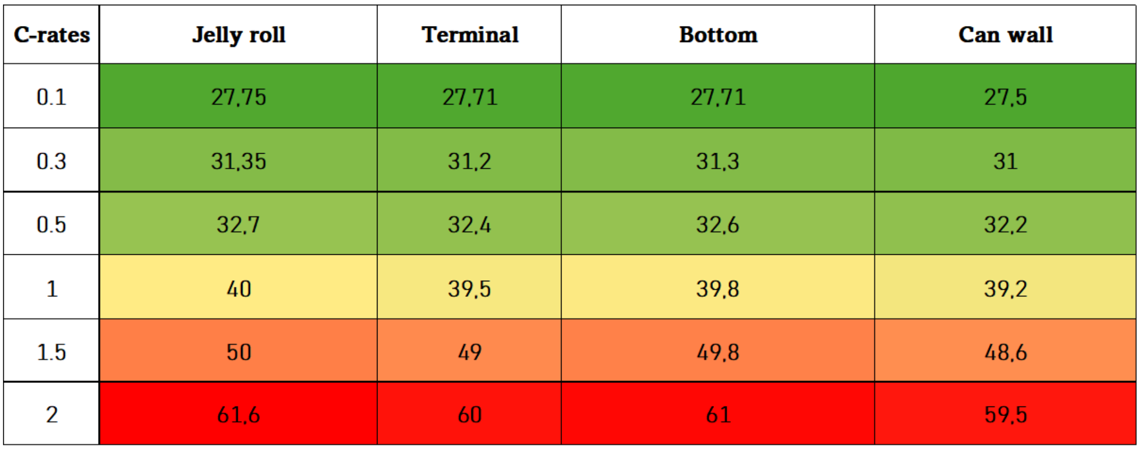

C-rates	Jelly roll	Terminal	Bottom	Can wall
0.1	27,75	27,71	27,71	27,5
0.3	31,35	31,2	31,3	31
0.5	32,7	32,4	32,6	32,2
1	40	39,5	39,8	39,2
1.5	50	49	49,8	48,6
2	61,6	60	61	59,5

Table 4.6 demonstrates that the temperature in the axial direction is about identical (the difference between bottom and terminal). The temperature values range slightly radially (between the jellyroll and the can wall). This is due to the difference in thermal conductivities between the axial and radial directions.

Table 4.7: Cooling Strategy Results

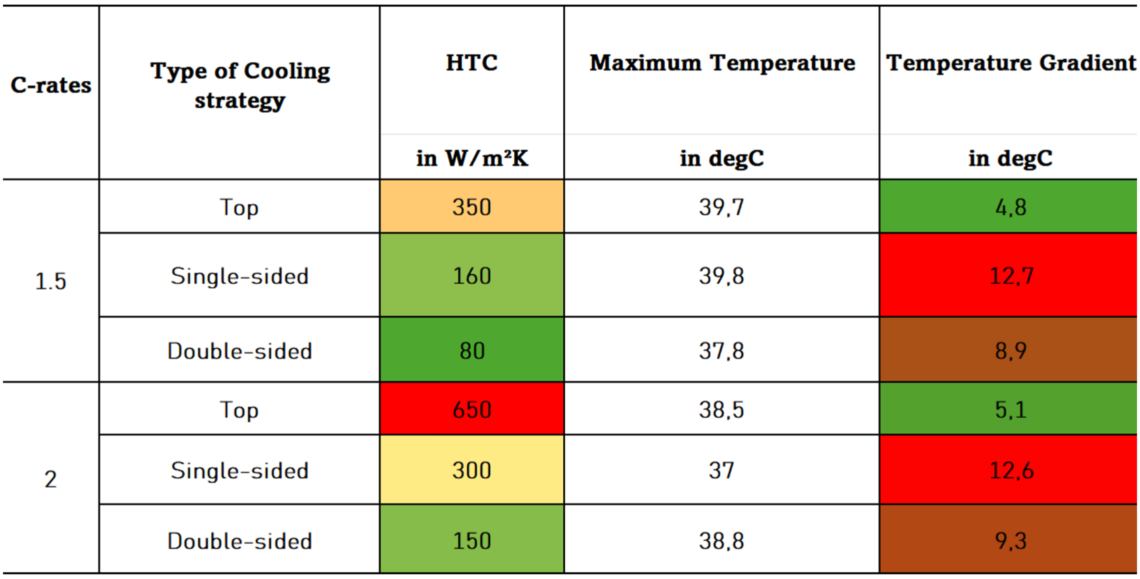

C-rates	Type of Cooling strategy	HTC	Maximum Temperature	Temperature Gradient
		in W/m²K	in degC	in degC
1.5	Top	350	39,7	4,8
	Single-sided	160	39,8	12,7
	Double-sided	80	37,8	8,9
2	Top	650	38,5	5,1
	Single-sided	300	37	12,6
	Double-sided	150	38,8	9,3

Table 4.7 shows how much heat must be removed to keep the cell's maximum temperature below 40 degrees Celsius. In addition, temperature gradients for various cooling techniques were detected. Because the cooling area is somewhat large, double-sided cooling requires less heat to be removed. However, top cooling has minimal temperature gradients due to its high axial thermal conductivity.

Table 4.8: Comparison of heat flux and temperature gradient for different contact areas

Inscribed Angle (°)	**Contact Surface Length (mm)**	**Required Heat Flux Removal ($W/(m^2 \cdot K)$)**	**Temperature Gradient (°C)**
60	24.073	307	5
90	36.11	207	6

Due to the varying surface area available for cooling the battery cell, the heat flux required to remove heat changes accordingly. As the cooling area increases, the heat flux per unit area decreases, while the total heat removal capacity of the cell improves. Therefore, both the contact area and the distribution of cooling play a critical role in determining the cell's effective thermal management. The amount of heat flux needed to remove for various contact surface area is mentioned in table 4.8.

The percentage decrease in the amount of heat flux needed to remove from cell from the simulation:

$$\begin{aligned}\text{Percentage decrease} &= \frac{60^\circ - 90^\circ}{60^\circ} \times 100\% \\ &= \frac{307 - 207}{307} \times 100\% \\ &= \frac{100}{307} \times 100\% \\ &\approx 33\% \quad \text{(rounded)}\end{aligned}$$

The percentage difference in heat flux values for 90 double-sided cooling from simulation and mathematically is:

$$\begin{aligned}\text{Percentage difference} &= \frac{\text{Simulated} - \text{Calculated}}{\text{Simulated}} \times 100\% \\ &= \frac{207 - 204.6}{207} \times 100\% \\ &= \frac{2.4}{207} \times 100\% \\ &\approx 1.2\% \quad \text{(rounded to 2 decimal places)}\end{aligned}$$

5

Conclusion

The calorimeter calibration showed both what the system could measure and where it failed. Initial tests had large variability at low power inputs, with coefficient of variation over 84% at 0.1 W. This was expected - low-power signals get close to the detection limits of heat flux sensors, where background thermal noise is almost as large as the signal itself. At higher power levels above 0.4 W, the system worked much better, getting variations below 20%.

As expected, the results improved with offset correction. Errors dropped from 67% to below 4% for moderate to high power inputs.This reveals the main problem was systematic errors, not random noise. If noise was the main issue, a low pass filter could have removed it.

Measurements of heat generation demonstrated a considerable difference between heat generation during charging and discharging of battery. The significant transport limitation and resistance offered by the almost-filled cathode lattice to the incoming lithium ions is the reason behind spike in heat generated. When designing cooling systems, these patterns are important. Initially, at the same C-rate, discharging produces roughly 36% greater peak heat than charging. A cooling system that is simply intended for charging will be insufficient. Second, there is a scaling issue: peak heat increases by more than ten times while current grows by six times when the temperature is raised from 0.05C to 0.3C.

These patterns matter for cooling system design. First, discharging makes about 36% more peak heat than charging at the same C-rate. A cooling system designed only for charging will be too small. Second, there is a scaling problem - going from 0.05C to 0.3C increases the current by six times, but peak heat goes up by more than ten times.

Both calorimetric and potentiometric methods measured how entropic coefficients change with SOC, showing both positive and negative regions. The potentiometric gave good linearity ($R^2 > 0.9$) at most SOC points, with similar results across different cells and temperatures. However, linearity dropped below 0.9 at the edges - the 0-10% and 90-100% SOC regions.The thermal behavior of a cell was studied using an electrothermal model to estimate internal heat generation and observe the temperature distribution of the cell in 3D thermal model to identify how heat propagates through the cell under different conditions. The models are lumped rather than detailed due to the limited amount of data available.

The findings clearly show that cell temperature rises dramatically with increasing C-rate, advancing from near-ambient conditions at 0.1C-rate to critical levels surpassing 60°C at 2C-rate. Across all working circumstances, the temperature distribution within the cell is relatively consistent, with differences between the jelly roll, terminal, bottom, and can wall of less than 2°C. However, the absolute temperature values at higher C-rates demonstrate a substantial relationship between cell thermal behavior and load intensity.

For a 2C-rate operation, double-sided cooling (150 W/m^2K) reaches a competitive maximum temperature of 38.8°C, but results in a large thermal gradient of 9.3°C. This gradient is 82% larger than the superior 5.1°C gradient accomplished by top cooling (650 W/m^2K) at the same rate. It is also closer to the bad performance of single-sided cooling (12.6°C). As a result, while successful at managing peak temperature, double-sided cooling at greater loads fails to provide ideal cell uniformity when compared with top cooling, which is crucial for longevity. However, removing the required heat through the limited surface area available on the top of the cell is challenging, as it demands a very high heat flux. To overcome this limitation, double-sided cooling was selected as the most effective strategy for this cell. Thus, the obtained results confirm known trends rather than presenting a surprising deviation.

To assess performance under extreme conditions, a worst-case scenario was simulated in COMSOL at a 1C rate. The results showed that 90° double-sided cooling performed better than 60° double-sided cooling configuration. Specifically, the heat flux required for 60° cooling was 33% higher than for 90° double-sided cooling. The heat flux obtained from the simulation is ideal because the deviation from mathematical value is just 1.2%. But the choice of 60° double-sided cooling represents a balance between thermal performance and practical design considerations. The geometry of the cooling tubes significantly affects both the efficiency of heat removal and the feasibility of installation, and in this case, the 60° cooling configuration offered the best compromise between effective cooling and manageable tube design.

6

Future Work

6.1 1D Model

The ECM computes irreversible heat generation and evaluates reversible heat generation using the corresponding equation in less than 30 seconds, yielding the total heat produced for a given load cycle. But the calculation time for the 3D thermal model to reflect the temperature distribution of the heat created is more significant. If we examine smaller mesh areas for precise results, the total computation time can be up to 4-5 hours. The lumped RC thermal model depicted in figure 6.1, could be built to shorten the total computing time required to obtain an understanding of the temperature distribution of the 4695 cell.

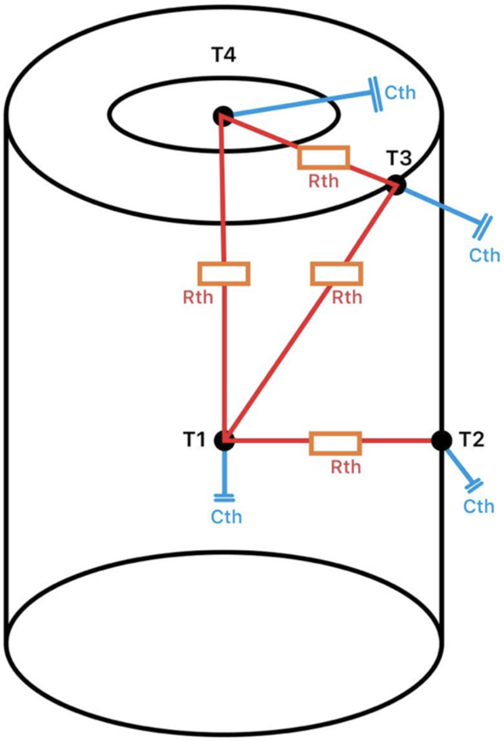

Figure 6.1: Lumped RC Thermal Model representation

Table 6.1: 1D model description

Parameter	Description
Rth	Thermal resistance between 2 materials
Cth	Thermal mass capacity
T1	Temperature at Jelly roll
T2	Temperature at Can
T3	Temperature at Top
T4	Temperature at Terminal

This model is a one-dimensional description of the temperature distribution within the cell. The thermal properties of the cell described in table 6.1 and the materials utilized in the cell were used to calculate the temperature at different locations. Thermal conductivity and specific heat capacity were the key thermal parameters investigated. The ECM generates the maximum overall heat value, which is then implemented in the center of the jelly roll. Thermal factors determine the temperature distribution across the cell. To validate this model with the experimental data or the 3D thermal model, make sure that the model is subjected to natural convection.

6.2 Cell Modeling

A detailed electrothermal model can provide more accurate predictions of cell behavior under high C-rates and extreme operating conditions. In the future, incorporating additional material properties could further enhance the model, allowing for better validation against experimental data. Such as more precise thermal properties of individual cell components would improve the accuracy of heat transfer simulations within the cell, leading to a more reliable representation of its thermal behavior.

In addition to that, performing adaptive time steps during simulation and mesh dependant study for different C-rates can also improve the accuracy of the results.

Bibliography

[1] Ossila Ltd. *Lithium-Ion Battery Components and Working Principle.* 2023. URL: `https://www.ossila.com/pages/lithium-ion-batteries`.

[2] U.S. Department of Energy. *How Lithium-ion Batteries Work.* 2023. URL: `https://www.energy.gov/energysaver/articles/how-lithium-ion-batteries-work`.

[3] Barnett Technical Services. “Hot Disk Battery Anisotropy”. In: (). Technical Report. URL: `https://www.stevesolutions.com`.

[4] et al. Xu. “Precise Determination of the Continuous Entropic Coefficient of Lithium-Ion Batteries”. In: *Journal of Electrochemical Science* (2024).

[5] et al. Geng. “Experimental and Numerical Study of Entropic Coefficients in Lithium-ion Batteries”. In: *Electrochimica Acta* (2021).

[6] et al. Choi. “Inverse Heat Transfer Analysis Method to Determine the Entropic Coefficient of a Lithium-ion Cell”. In: *Thermal Science and Engineering Progress* (2023).

[7] U. et al. Han. *Estimation of Reversible Entropic Heat of Lithium Battery Using Inverse Heat Transfer and Least Squares Optimization.* Tech. rep. National Renewable Energy Laboratory, 2022.

[8] Wadsö. “Electrical Calibration of Heat Conduction Calorimeters”. In: *Journal of Thermal Instrumentation* (2024).

[9] PowerTech Systems. *Lithium-Ion State of Charge (SoC) Measurement.* 2024. URL: `https://www.powertechsystems.eu/home/tech-corner/lithium-ion-state-of-charge-soc-measurement/`.

[10] Analog Devices Inc. “A Closer Look at State of Charge (SOC) and State of Health (SOH) Estimation Techniques for Batteries”. In: *Analog Dialogue* (2025).

[11] BatteryDesign.net. *SoC Estimation Techniques.* 2025. URL: `https://www.batterydesign.net/soc-estimation-techniques/`.

[12] et al. Singh. “State of Charge Estimation Techniques of Li-ion Battery: A Review”. In: *Journal of Energy Storage* (2023).

[13] Jiaping Zhou, Bo Xing, and Chunyang Wang. *A review of lithium ion batteries electrochemical models for electric vehicles: E3s Web of Conferences.* Sept. 2020. URL: `https://www.e3s-conferences.org/articles/e3sconf/ref/2020/45/e3sconf_iceeb2020_04001/e3sconf_iceeb2020_04001.html`.

[14] Haider Adel Ali Ali and Ziad Namir Abdeljawad. *Thermal Management Technologies of Lithium-Ion Batteries Applied for Stationary Energy Storage Systems: Investigation on the Thermal Behavior of Lithium-Ion Batteries.* 2020.

[15] Mikäel Cugnet, Matthieu Dubarry, and Bor Yann Liaw. Apr. 2010. URL: `https://www.researchgate.net/publication/230823728_Peukert%E2%80%99s_Law_of_a_Lead-Acid_Battery_Simulated_by_a_Mathematical_Model`.

[16] Duo Yang et al. *A neural network based state-of-health estimation of lithium-ion battery in electric vehicles.* June 2017. URL: `https://www.sciencedirect.com/science/article/pii/S1876610217306355?via%3Dihub`.

[17] Saumitra Jagdale. *Li-ion batteries and equivalent circuits.* June 2023. URL: `https://www.powerelectronicsnews.com/modeling-li-ion-batteries-with-equivalent-circuit-technology/`.

[18] Jianwen Meng et al. *A new cascaded framework for lithium-ion battery state and parameter estimation.* Feb. 2020. URL: `https://www.mdpi.com/2076-3417/10/3/1009`.

[19] E. Karden et al. *Modeling of lithium ion cells-a simple equivalent-circuit model approach.* Oct. 2004. URL: `https://www.sciencedirect.com/science/article/pii/S0167273804006678?via%3Dihub`.

[20] Ahmad A. Pesaran. *Battery thermal models for hybrid vehicle simulations.* May 2002. URL: `https://www.sciencedirect.com/science/article/pii/S0378775302002008?via%3Dihub`.

[21] Shuaishuai Lv et al. *The influence of temperature on the capacity of lithium ion batteries with different anodes.* Dec. 2021. URL: `https://www.mdpi.com/1996-1073/15/1/60`.

[22] Shuai Ma. *Temperature effect and thermal impact in lithium-ion batteries: A Review.* Nov. 2018. URL: `https://www.sciencedirect.com/science/article/pii/S1002007118307536?ref=pdf_download&fr=RR-2&rr=95f7ef45783870d3`.

[23] G.X. Wang et al. *Kinetic behavior of LiFePO4/C cathode material for lithium-ion batteries.* Nov. 2007. URL: `https://www.sciencedirect.com/science/article/pii/S0013468607013576`.

[24] S.S. Zhang. *The low temperature performance of Li-Ion Batteries.* Dec. 2002. URL: `https://www.sciencedirect.com/science/article/pii/S0378775302006183`.

[25] Ashish Rajkumar Devshette. *Air-cooled and PCM-cooled battery thermal management systems of an electric vehicle: a technical review.* Apr. 2025. URL: `https://iopscience.iop.org/article/10.1088/2631-8695/adc876`.

[26] Charlotte Roe. *Immersion cooling for lithium-ion batteries – a review - sciencedirect.* 2025. URL: `https://www.sciencedirect.com/science/article/pii/S0378775322001185`.

[27] Ping Fu et al. *A review of cooling technologies in lithium-ion power battery thermal management systems for new energy vehicles.* Dec. 2023. URL: `https://www.mdpi.com/2227-9717/11/12/3450`.

[28] Maan Al-Zareer, Ibrahim Dincer, and Marc A. Rosen. Mar. 2018. URL: `https://www.tandfonline.com/doi/full/10.1080/10407782.2018.1439237`.

[29] Jiahao Liu et al. *Recent progress and prospects in liquid cooling thermal management system for lithium-ion batteries.* Aug. 2023. URL: `https://www.mdpi.com/2313-0105/9/8/400`.

[30] URL: `http://miba.com/en/emobility/battery-cooling`.

[31] A. Greco et al. *Thermal performance of lithium-ion battery thermal management system by using mini-channel cooling.* Aug. 2016. URL: `https://www.sciencedirect.com/science/article/pii/S0196890416307373`.

[32] et al. Zhang. "Voltage Characteristics of Lithium-ion Cells Under Quasi-Equilibrium Conditions". In: *Journal of Battery Science* (2018).

[33] Xiaoping Wang et al. "Advanced OCV-SOC modeling for lithium-ion batteries considering hysteresis and temperature effects". In: *Energy Storage Materials* 58 (2024), pp. 445–458. DOI: `10.1016/j.ensm.2023.12.041`.

[34] Ukmin Han and Hoseong Lee. "Estimation Of Reversible Entropic Heat Of Lithium Battery Based On Inverse Heat Transfer Analysis and Least-squares Optimization". In: *Proceedings of the 19th International Refrigeration and Air Conditioning Conference at Purdue.* Purdue University. West Lafayette, IN, USA, 2022. URL: `https://docs.lib.purdue.edu/iracc/2329`.

[35] P. K. Singh et al. "Title of the Singh et al. 2023 Paper". In: *Journal Name* xx.xx (2023), pp. xx–xx. DOI: `put-doi-here`.

[36] H. Zhao et al. "Advancing lithium-ion battery anodes towards a sustainable future: prospects, challenges, and perspectives". In: *Materials Today Energy* 37 (2025), p. 101190. DOI: `10.1016/j.mtener.2024.101190`.

[37] Shen Li. *How to enable large format 4680 cylindrical lithium-ion batteries.* 2023. URL: `https://doi.org/10.1016/j.apenergy.2023.121548`.

[38] Christian Allgäuer. *Thermal management of 4680 battery cells: Cell design and cooling concept.* Sept. 2025. URL: `https://doi.org/10.1016/j.est.2025.117318`.

DEPARTMENT OF SOME SUBJECT OR TECHNOLOGY
CHALMERS UNIVERSITY OF TECHNOLOGY
Gothenburg, Sweden
www.chalmers.se

CHALMERS
UNIVERSITY OF TECHNOLOGY